

UC San Diego

UC San Diego Electronic Theses and Dissertations

Title

Cloudiness over the Mountains of the Western United States: Variability and Influences on Snowmelt and Streamflow

Permalink

<https://escholarship.org/uc/item/1bz9q9cm>

Author

Sumargo, Edwin

Publication Date

2018

Supplemental Material

<https://escholarship.org/uc/item/1bz9q9cm#supplemental>

Peer reviewed|Thesis/dissertation

UNIVERSITY OF CALIFORNIA SAN DIEGO

Cloudiness over the Mountains of the Western United States: Variability and Influences on
Snowmelt and Streamflow

A dissertation submitted in partial satisfaction of the
requirements for the degree

Doctor of Philosophy

in

Earth Sciences

by

Edwin Sumargo

Committee in charge:

Daniel R. Cayan, Chair
Michael D. Dettinger
Ian Eisenman
Jan Kleissl
Joel R. Norris
Shang-Ping Xie

2018

© Copyright

Edwin Sumargo, 2018

All rights reserved

The Dissertation of Edwin Sumargo as it is listed on UCSD Academic Records is approved, and it is acceptable in quality and form for publication on microfilm and electronically:

Chair

University of California San Diego

2018

DEDICATION

To my parents, for their love and support since the beginning.

And to God, unto whom I owe my existence and salvation.

TABLE OF CONTENTS

Signature Page.....	iii
Dedication	iv
Table of Contents	v
List of Abbreviations.....	ix
List of Figures	xiii
List of Tables.....	xvii
Acknowledgments.....	xix
Vita.....	xxi
Abstract of the Dissertation.....	xxii
Chapter 1 Introduction	1
1.1 Background and Motivations	1
1.2 Spatial and Temporal Scopes of the Research	4
Chapter 2 Variability of Cloudiness over Mountain Terrain in the Western United States	12
2.1 Introduction	12
2.2 Datasets	15
2.2.1 GOES-West Visible Cloud Albedo.....	15
2.2.2 Gridded Elevation Data.....	16
2.2.3 Reanalyzed Meteorological Data and Low Frequency Weather Anomalies Indices	17
2.3 Methods.....	17
2.3.1 Determining the Clear-sky Albedo and the Cloud Albedo	17
2.3.2 Quantifying Solar Insolation Sensitivity to Cloudiness Variation	19
2.3.3 Low Elevation Mask	20
2.3.4 Removing the Seasonal Cycle of Cloud Albedo and Meteorological Variables.....	20

2.3.5	Rotated Empirical Orthogonal Function (REOF) of Daily Cloud Anomalies.....	21
2.3.6	Composites Based upon Extreme RPC Values	22
2.3.7	Contingencies Based upon Extreme RPC Values	22
2.4	Results and Discussion.....	23
2.4.1	Cloud Variability on Daily to Inter-annual Time Scales.....	23
2.4.2	Sensitivity of Solar Insolation to Cloudiness Variability.....	28
2.4.3	Coherent Patterns of Daily Cloud Variability	29
2.4.4	Relations to Larger Scale Circulation Patterns	33
2.4.5	Relations to Lower Frequency Climate Variability Patterns	34
2.5	Summary and Conclusions.....	40
Appendix 2A	GOES Data Availability.....	42
Appendix 2B	Clear-sky Albedo Time Window	44
Appendix 2C	Determining the Seasonal Cycle	45
Chapter 3	The Influence of Cloudiness on Hydrologic Fluctuations in the Mountains of the Western United States	53
3.1	Introduction	54
3.2	Data, Methods and Tools	58
3.2.1	Observational Datasets and Processing.....	58
3.2.1.1	Cloud Cover Index	58
3.2.1.2	Snow Water Equivalent.....	59
3.2.1.3	Streamflow	60
3.2.1.4	Precipitation and Surface Air Temperature.....	61
3.2.2	Contingency Analysis of Cloudiness and Snowmelt	61
3.2.3	Multivariate Linear Regression Analysis of Cloudiness and Snowmelt/Streamflow	62
3.2.4	REOF Analysis of Cloudiness.....	63
3.3	Results	64

3.3.1	Local Cloudiness and Snowmelt Variations	64
3.3.2	Antecedent Cloudiness and Snowmelt/Streamflow Fluctuations	66
3.3.3	Snowmelt/Streamflow Variations Accounted by Local Cloudiness Variability.....	69
3.3.3.1	Cloudiness and Snowmelt Variability.....	71
3.3.3.2	Cloudiness and Streamflow Variability	76
3.3.3.3	Elevational Dependence of Snowmelt and Streamflow Responses to Cloudiness Variability.....	79
3.3.4	Regional Cloudiness vs. Snowmelt/Streamflow Variability.....	82
3.4	Summary and Conclusions.....	84
Appendix 3A	Cloudiness Relationships with Precipitation and Diurnal Air Temperature	88
Appendix 3B	Training and Validation of Δ SWE and Δ Q Models.....	89
Appendix 3C	Asymmetry of Cloudiness Associations between Dry Years and Wet Years.....	91
Chapter 4	Effects of Cloud Variability on Snow-fed Runoffs in California’s Sierra Nevada.....	103
4.1	Introduction.....	104
4.2	Precipitation-Runoff Modeling System (PRMS)	107
4.2.1	Model Description.....	107
4.2.2	GOES-derived Solar Radiation Input.....	112
4.3	PRMS Experiments to Explore Response to Cloudiness	114
4.3.1	Snow-fed Streamflow Response to Daily Cloudiness Variability	114
4.3.2	Snow-fed Streamflow Response to High/Mid/Low Elevation Cloudiness	115
4.3.3	Snow-fed Streamflow Response to Intensified Daily Cloudiness Fluctuations	117
4.4	Results and Discussion.....	119
4.4.1	Snow-fed Streamflow Response to Daily Cloud Variability	119
4.4.2	Snow-fed Streamflow Response to Cloudiness at Different Elevations Bands.....	123

4.4.3	Snow-fed Streamflow Response to Intensified Daily Cloudiness Fluctuations	127
4.5	Summary and Conclusions.....	131
Appendix 4A	Determining the Time Windows of UB and LB	134
Appendix 4B	Determining Dry vs. Wet Years.....	136
Appendix 4C	PRMS Model Calibration.....	137
Appendix 4D	Different Effects of Dry vs. Wet Years.....	141
Chapter 5	Conclusions	152

LIST OF ABBREVIATIONS

AO	Arctic Oscillation
CC	cloud cover
CDEC	California Data Exchange Center
CDWR	California Department of Water Resources
CRM	Crater Meadows snow pillow site in Idaho
CSS	Cooperative Snow Survey
CV	coefficient of variation
DAN	Dana Meadows snow pillow site in California
DJF	December-January-February (boreal winter)
dT	diurnal temperature range
DTR	Diurnal Temperature Range-based solar radiation parameterization
ENSO	El Niño Southern Oscillation
ET	evapotranspiration
f	cloud albedo multiplication factor
$f Bias $	fractional mean absolute bias
FIL	Fish Lake snow pillow site in Oregon
GIN	Gin Flat snow pillow site in California
GOES	Geostationary Operational Environmental Satellite
HCDN	Hydro-Climatic Data Network
HRU	Hydrologic Response Unit
HTH	Hetch Hetchy Reservoir
JJA	June-July-August (boreal summer)

LB	lower bound of cloud dynamical range
LST	local standard time
LWF	longwave flux/radiation
MAM	March-April-May (boreal spring)
MELT	snowmelt
MRMF	Merced River at Merced Forks
NARR	North American Regional Reanalysis
NASA	National Aeronautics and Space Administration
NGDC	National Geophysical Data Center
NOAA	National Oceanic and Atmospheric Administration
NRCS	Natural Resources Conservation Service
NW	northwestern United States
P	precipitation
PET	potential evapotranspiration
PNA	Pacific-North America pattern
POH	Merced River at Pohono Bridge in Yosemite National Park
PRISM	Precipitation-elevation Regressions on Independent Slopes Model
PRMS	Precipitation-Runoff Modeling System
PST	Pacific standard time
Q	streamflow
R	correlation
R_{auto}	autocorrelation
REOF	rotated empirical orthogonal function

RH	relative humidity
RMSE	root-mean-squared error
RPC	rotated principal component
SNOTEL	Snow Telemetry
SoDa	Solar radiation Data
SON	September-October-November (boreal autumn)
STP	Stampede Pass snow pillow site in Washington
SW	southwestern United States
SWE	snow water equivalent
SWF	shortwave flux (also solar radiation/insolation)
SWF _{clear}	clear-sky shortwave flux
T _a	surface air temperature
T _{avg}	daily average surface air temperature
T _{max}	daily maximum surface air temperature
T _{min}	daily minimum surface air temperature
TRLG	Tuolumne River below La Grange Dam
U	wind speed
U.S.	United States
UB	upper bound of cloud dynamical range
UEB	Utah Energy Balance snow model
USDA	United States Department of Agriculture
USGS	United States Geological Survey
WUS	western United States

WY	water year
Z_{500}	500-hPa geopotential height
z_{t1}	the first tercile of elevation
z_{t2}	the second tercile of elevation
α	albedo
α_{clear}	clear-sky albedo
α_{cloud}	cloud albedo
α_{cm}	median cloud albedo
α_{ovc}	overcast albedo
ΔQ	daily-centered streamflow change
ΔSWE	daily-centered snow water equivalent change
μ	mean/average
σ	standard deviation
ϕ	phi correlation coefficient of the χ^2 statistics
χ^2	Chi-squared statistical significance
ω_{500}	500-hPa pressure vertical velocity

LIST OF FIGURES

Figure 2.1.	(Top) Daily mean α_{clear} over California and Nevada before and after 1-3 December 2005 snowstorm. (Bottom) November and December 2005 time-series of local noontime α and the estimated α_{clear} and α_{cloud} at GOES pixel overhead Dana Meadows in Yosemite National Park.....	19
Figure 2.2.	Maps of mean (μ), standard deviation (σ) and coefficient of variation (CV) of daily α_{cloud} for winter (DJF), spring (MAM) and summer (JJA).....	24
Figure 2.3.	DJF, MAM and JJA standard deviation and coefficient of variation calculated from seasonal (three-month) α_{cloud} averages. Means for the seasonal averages are same as those in Figure 2, so are not shown. Note change in color scales from those in Figure 2.	25
Figure 2.4.	Correlation (R) fields (all months of 1996-2014) between de-seasonalized daily α_{cloud} and (a) RPC1, (b) RPC2, (c) RPC3, (d) RPC4, and (e) RPC5 over the entire domain. Only pixels with p -value < 0.05 are colored.	30
Figure 2.5.	Standard deviations of (a) RPC1, (b) RPC2, (c) RPC3, (d) RPC4, and (e) RPC5 for each month in α_{cloud} percent units, exemplifying the seasonal structures of each RPC mode.	32
Figure 2.6.	500-hPa geopotential height (Z_{500}) anomaly (isolines) and pressure vertical velocity (ω_{500}) anomaly (shades) composited for days with the most positive (a and b) and most negative (c and d) anomalies for RPC1 (left) and RPC2 (right).....	34
Figure 2.7.	Correlation maps between the seasonal averages of the five leading α_{cloud} RPCs and those of Z_{500} anomaly for 1996-2014. The gray contours denote the areas where p -value < 0.05	39
Figure 2.A1.	<u>Left</u> : Number distribution of missing data for each month and half-hour of the day of 1996-2014. <u>Right</u> : The percentages of hours between 0800 and 1600 PST exist per day during the same period and averaged over the same pixels.	43
Figure 2.B1.	Daily time-series of water year 2006 SWE (gray shading) and of clear-sky albedo derived using four different time windows (color plots) at Dana Meadows in the Yosemite National Park, California, (left) and Crater Meadows in Idaho (right).....	45
Figure 2.C1.	Daily climatology (1996-2014) of α_{cloud} (gray) and its low-pass filtered versions using Chebyshev Type I filter (blue) and original 29-day (± 14 days) centered moving average (red) at four different locations.	46
Figure 3.1.	USGS HCDN stream gauges, CDWR CSS (CDEC) snow sensors and USDA/NRCS SNOTEL snow pillows employed in this study. The	

	background colors signify the Northwest and the Southwest climate regions.	57
Figure 3.2.	<u>Upper</u> : Correlation between de-seasonalized overhead CC and subsequent and concurrent MELT at (a) Gin Flat and (b) Crater Meadows. <u>Lower</u> : Correlations between de-seasonalized overhead CC and subsequent or coherent ΔQ at (c) Merced River and (d) South Fork Clearwater River.	68
Figure 3.3.	Variance of MELT (left) and ΔQ (right) anomalies explained (%) by anomalous CC predictors in lagged multiple regressions for February, April and June of 1996-2015. Circle size is proportional to R^2 (%).	71
Figure 3.4.	Scatter plots of R^2 between modeled and measured MELT (left) and ΔQ (right) as a function of station altitude for February, April and June, showing the variations of CC-MELT association with elevation and month. The red lines are least-square fits denoting the data trends.	81
Figure 3.5.	<u>Left</u> : The NW REOF of February to July de-seasonalized daily CC anomalies from 1996-2015. <u>Center</u> : Correlations between the NW RPC daily time series and MELT anomalies for February, April and July. <u>Right</u> : Same as center panel, except between the NW RPC time series and ΔQ	83
Figure 3.6.	Same as Figure 3.5, except for the SW daily CC REOF.	84
Figure 3.A1.	Monthly correlations (1996-2015) between de-seasonalized CC, P and dT at (a) Gin Flat in California (37.767 °N, 119.773 °W, 2,149 m) and (b) Crater Meadows in Idaho (46.56 °N, 115.29 °W, 1,817 m), ordered according to water-year months (October-September).	89
Figure 3.C1.	Daily MELT variance explained by anomalous CC (%) for February, April and June during dry years (left) and wet years (right) of 1996-2015. Circle size is proportional to R^2 (%).	92
Figure 3.C2.	Same as Figure 3.C1, except for ΔQ	94
Figure 4.1.	Observed vs. estimated daily SWF at Dana Meadows for snowmelt season (February-July) of 1996-2014. The SWF estimates are derived using PRMS version of diurnal temperature range (DTR) algorithm and using Ineichen-Perez algorithm with using GOES α (GOES).	109
Figure 4.2.	<u>Top left</u> : PRMS Tuolumne River basin. The upper Tuolumne basin is hatched. <u>Top right</u> : PRMS Merced River basin. The upper Merced basin is hatched. <u>Bottom</u> : Wavelet coherence between the observed daily inflow to HTH and observed daily streamflow at POH, for WYs 1996-2013.	112
Figure 4.3.	Daily climatology (1996-2014) of SWF at Dana Meadows (DAN) from observation, Ineichen-Perez algorithm with original α_{cloud} (Baseline), and Ineichen-Perez algorithm with annual harmonic α_{cloud} (Annual harmonic clouds).	115

Figure 4.4.	Snowmelt season (February-July) daily climatological mean (1996-2014 for Tuolumne and 1996-2013 for Merced) CC at each HRU in the Upper Tuolumne (left) and Merced (right) watersheds..	117
Figure 4.5.	<u>Top</u> : WYs 2010-2013 time series of Tuolumne River inflow to HTH (left), and of Merced River inflow to POH (right), from Baseline (blue) and “Annual harmonic clouds” (orange) simulations. <u>Bottom</u> : Differences, Baseline minus “Annual harmonic clouds” simulations.....	120
Figure 4.6.	Differences in HRU spring onsets between Baseline and “Annual harmonic clouds” simulations, mapped (top) and plotted against HRU elevations (bottom), for the upper Tuolumne (left) and Merced (right) River basins. The plots are the daily climatological averages.	122
Figure 4.7.	Daily climatology of basin area-weighted evapotranspiration (ET) of the Upper Tuolumne River (left) and the Upper Merced River (right) basins, for the Baseline and “Annual harmonic clouds” simulations (top) and those of the differences between the two simulations (bottom).	123
Figure 4.8.	The differences in daily climatological averages between Baseline simulation and “No clouds at high elevation HRUs” (top), or “No clouds at mid elevation HRUs” (middle), or “No clouds at low elevation HRUs” (bottom) simulation.	125
Figure 4.9.	Differences in Upper Tuolumne River basin’s HRU spring onsets between Baseline simulation and No clouds at (a) high, (b) mid, and (c) low elevations HRUs simulations, mapped (left) and plotted against HRU elevations (right). The plots are the daily climatological averages.	127
Figure 4.10.	The differences in daily climatological averages between Baseline simulation and “Clear gets clearer” simulation (left), and between Baseline simulation and “Cloudy gets cloudier” simulation (right).	129
Figure 4.11.	The daily climatological averages of the observed and simulated inflows to HTH for the dry-year (top) and wet-year (bottom) subsets, illustrating the different flow timings and discrepancies between the Baseline and “Cloudy gets cloudier” simulations between the two subsets.	131
Figure 4.A1.	The <i>R</i> (left) and RMSE (right) between the observed and Ineichen-Perez estimated SWF at Dana Meadows in California (37.897 °N, 119.257 °W, 2,987 m) for all months (blue) and February-July period (red) of 1996-2014, for the UB (top) and LB (bottom) cases.....	135
Figure 4.B1.	<u>Top</u> : January-September total inflow to HTH for every water year of 1996-2014, showing 9 wettest and 9 driest years in the period. <u>Bottom</u> : January-September upper Tuolumne River basin composite mean α cloud for every water year of 1996-2014.	136

Figure 4.C1. The observed (shade) and simulated (plots) daily climatology of inflow to HTH using the original diurnal temperature range (DTR) method and using calibrated Ineichen-Perez algorithm based on GOES α (GOES), for all-year (left), dry-year (upper right) and wet-year (lower right) subsets. 140

Figure 4.C2. Same as Figure 4.C1, except for the PRMS Merced model..... 141

Figure 4.D1. Top sub-panels: Daily climatology of inflow to HTH for all-year, dry-year and wet-year subsets from PRMS upper Tuolumne River basin model Baseline and “Annual harmonic clouds” simulations. Bottom sub-panels: The resulting difference between the Baseline and “Annual harmonic clouds” simulations. 143

Figure 4.D2. Same as Figure 4.D1, except for streamflow at POH from PRMS upper Merced River basin model. 144

LIST OF TABLES

Table 2.1.	Daily and seasonal means (μ) and standard deviations (σ) of α_{cloud} in percent and the coefficients of variations (CV) for winter (DJF), spring (MAM), summer (JJA), and autumn (SON).....	25
Table 2.2.	Change in daily solar irradiance (SWF) at the surface corresponding to a 10% increase in daily α_{cloud} estimated for two Region 1 locations (Dana Meadows, CA, and Fish Lake, OR) and two Region 2 locations (Crater Meadows, ID, and Quartz Peak, WA).	28
Table 2.3.	The eigenvalues of α_{cloud} REOFs/RPCs 1-5 and the specific geographical areas where each mode is pronounced. The eigenvalue represents the amount of variance explained by each mode.....	29
Table 2.4.	χ^2 values of the contingency tables relating the five RPC modes to selected teleconnection indices during winter (DJF), spring (MAM), and summer (JJA) of 1996-2014. The statistic is significant at 95% confidence level when $\chi^2 > 3.84$ (bold numbers).	35
Table 2.5.	ϕ coefficients associated with the χ^2 statistics, indicating the magnitude and the sign of the correlations between the RPCs and teleconnection indices during winter (DJF), spring (MAM), and summer (JJA) of 1996-2014.	36
Table 2.6.	Contingency table showing the relationship between RPC1 and PNA in JJA.	37
Table 2.7.	Contingency table showing the relationship between RPC2 and Niño3.4 in JJA.....	37
Table 2.A1.	The R , RMSE and $f Bias $ between daily average cloud albedo when no half-hour between 0800 and 1600 LST is missing and that when one or more (n) half-hours are missing, for $1 \leq n \leq 10$ only. The RMSEs are in percent cloud albedo unit.	44
Table 3.1.	Numbers of Days associated with Snow Accumulation/Melt coincident with Clear/Moderate/Cloudy Sky for February-July of 1996-2015 at Gin Flat in California (37.767 °N, 119.773 °W, 2,149 m).	64
Table 3.2.	Area-averaged R^2 (%) of Multiple Regression-modeled ΔSWE , February-July 1996-2015.....	72
Table 3.3.	The R^2 (%) of Multiple Regression-Modeled ΔSWE , Trained (1996-2005) and Validated (2006-2015) using Observed (left) and UEB-modeled (right) SWE for Selected Stations.....	73
Table 3.4.	R^2 (%) of Multiple Regression-modeled ΔQ for February-July of 1996-2015.	76

Table 3.B1.	Same as Table 3.2, except for when the training and validation periods are treated separately.....	90
Table 3.B2.	Same as Table 3.4, except for when the training and validation periods are treated separately.....	90
Table 3.C1.	Same as Table 3.2, except for the Dry-year and Wet-year Subsets.	93
Table 3.C2.	Same as Table 3.4, except for the Dry-year and Wet-year Subsets.	95
Table 4.C1.	The R , RMSE and NSE between the daily climatological averages of the observed and PRMS simulated inflow to HTH and streamflow at POH, using the original diurnal temperature range-based SWF (DTR) and the calibrated Ineichen-Perez SWF based on GOES α (GOES).....	139

ACKNOWLEDGEMENTS

First and foremost, I am profoundly thankful for my advisor Dan Cayan, for his constant support, patience and unending insights. It has been blissful to have Dan as an advisor and friend, from whom I have learned not only to be a dedicated and detail-oriented scientist, but also to remain humble and how to be a great advisor/mentor. He genuinely cares for his students and staffs and is always hard working, positive and friendly to those around him. I cannot thank Dan enough for his guidance and substantial role in paving my path to the future.

I am deeply grateful to Mike Dettinger, Sam Iacobellis and Mary Tyree. Their helps and supports have significantly contributed to my start and growth as a graduate student and researcher. Mike has been a close colleague and mentor. His insights and dedications have been an inspiration. Along with Dan, Mike is a tremendous role model in both office and field works. I am indebted to Sam for the GOES database, and to Sam and Mary for the Fortran codes and various other assistances that they have provided. Without which, I would have taken many more months (or years) to produce the same amount of research output.

I am also thankful to Ian Eisenman, Jan Kleissl, Joel Norris, and Shang-Ping Xie for serving as my thesis committee members and for their thoughtful advices and discussions. I am particularly indebted to Joel Norris. His insights and feedbacks have been instrumental in every chapter of my thesis. I would also like to thank Alexander Gershunov, Bruce Cornuelle, and many more for their helps, insights and discussions throughout the years.

Beyond the SIO community, I would like to acknowledge Bruce McGurk for his mentorship and guidance in hydrology and for providing training in the PRMS hydrologic

model. Finally, I would like to thank Mike Anderson and the California Department of Water Resources for providing funds and resources that make this dissertation possible.

Chapter 2, in full, is a reprint of the material as it appears in *Journal of Hydrometeorology* in 2017, with slight modifications. Sumargo, E., and D. R. Cayan, 2017: Variability of cloudiness over mountain terrain in the Western United States. *J. Hydrometeorol.*, **18**, 1227–1245. <https://doi.org/10.1175/JHM-D-16-0194.1>. ©American Meteorological Society. Used with permission. The dissertation author was the primary investigator and author of this paper.

Chapter 3, in full, has been submitted for publication to *Water Resources Research*, with slight modifications. Sumargo, E., and D. R. Cayan, 2018: The Influence of Cloudiness on Hydrologic Fluctuations in the Mountains of the Western United States. *Submitted for publication in Water Resour. Res.* The dissertation author was the primary investigator and author of this paper.

Chapter 4, in part, is currently being prepared for submission for publication. Sumargo, E., Effects of Cloud Variability on Snow-fed Runoffs in California's Sierra Nevada. The dissertation author was the sole investigator and author.

VITA

- 2011 B.S. in Atmospheric Sciences, University of Illinois Urbana-Champaign
- 2014 M.S. in Earth Sciences, University of California San Diego
- 2018 Ph.D. in Earth Sciences, University of California San Diego

PUBLICATIONS

Sumargo, E., and D. R. Cayan, Effects of Cloud Variability on Snow-fed Runoffs in California's Sierra Nevada, *in preparation*.

Sumargo, E., and D. R. Cayan, 2018: The Influence of Cloudiness on Hydrologic Fluctuations in the Mountains of the Western United States. *Submitted for publication in Water Resour. Res.*

Sumargo, E., and D. R. Cayan, 2017: The Influence of cloudiness, temperature and precipitation variabilities on snowmelt and streamflow variations in the western U.S. *Proc. Western Snow Conf.*, **85**, pp. 85-96 [Available at <https://westernsnowconference.org/files/PDFs/2017Sumargo.pdf>]

Sumargo, E., and D. R. Cayan, 2017: Variability of cloudiness over mountain terrain in the Western United States. *J. Hydrometeorol.*, **18**, 1227–1245. <https://doi.org/10.1175/JHM-D-16-0194.1>.

Lapo, K. E., L. M. Hinkelman, **E. Sumargo**, M. Hughes, and J. D. Lundquist, 2017: A critical evaluation of modeled solar irradiance over California for hydrologic and land surface modeling. *J. Geophys. Res. Atmos.*, **122**, 299-317. doi:10.1002/2016JD025527.

Cayan, D. R., M. D. Dettinger, D. Pierce, T. Das, N. Knowles, F. M. Ralph, and **E. Sumargo**, 2016: Natural Variability, Anthropogenic Climate Change, and Impacts on Water Availability and Flood Extremes in the Western United States. In *Water Policy and Planning in a Variable and Changing Climate* (pp. 17-42). CRC Press.

Sumargo, E., and D. R. Cayan, 2015: Variability of cloud cover and its relation to springtime snowmelt and runoff. *Proc. Western Snow Conf.*, **83**, pp. 77-87. [Available at <https://westernsnowconference.org/files/PDFs/2015Sumargo.pdf>]

ABSTRACT OF THE DISSERTATION

Cloudiness over the Mountains of the Western United States: Variability and Influences on
Springtime Snowmelt and Streamflow Fluctuations

by

Edwin Sumargo

Doctor of Philosophy in Earth Sciences

University of California San Diego, 2018

Daniel R. Cayan, Chair

This dissertation demonstrates the uses of satellite and surface observations, in tandem with hydrologic modeling, to characterize daily-to-interannual cloudiness variability and its influence on spring-summer snowmelt and streamflow fluctuations over the mountains of the western United States from 1996 to 2015.

Daily cloudiness variations can exceed 50% of long-term averages during the springtime. When aggregated over three-month periods, cloudiness varies by $\pm 10\%$ of long-term averages in many locations. Rotated empirical orthogonal functions (REOFs) analysis indicates the first five REOFs account for $\sim 67\%$ of the total variance, each of which has distinct regional and seasonal emphases. Each of the REOF modes associates with anomalous large scale atmospheric circulation patterns and one or more large-scale

teleconnection indices, which helps to explain why anomalous cloudiness patterns take on regional spatial scales and contain substantial variability over seasonal time scales.

Cloud cover indices (CC) are, to some extent, related linearly to snowmelt (Δ SWE) and snow-fed streamflow (Δ Q) fluctuations. Local CC- Δ SWE and CC- Δ Q associations vary with time and location, with the dominance of negative correlations between CC and Δ SWE, exemplifying the cloud-shading (or clear-sky) effect on snowmelt. The magnitude of CC- Δ SWE association (R^2) amounts to 5%-56%, typically peaking in May. These associations fade earlier in summer during dry years than wet years, indicating the differing responses of higher vs. lower snowpack. The CC- Δ Q association displays less consistent arrangement, with R^2 amounting to 2%-47%. The Δ SWE and Δ Q fluctuations exhibit spatially extensive patterns of correlations with daily CC anomalies, indicating the effects of cloudiness often operate over regional scales.

On a watershed scale, cloudiness variability redistributes the seasonal runoff and hastens the spring onset by 1-3 days. Higher elevation cloudiness exerts a greater influence on the basin runoff than lower elevation cloudiness does. Overall, cloudiness delays spring onset by 2-15 days regardless of the elevation. Lastly, the experiment on the intensification of cloudiness fluctuations suggests greater streamflow sensitivity to the “relatively cloudy periods get cloudier” scheme than to the “relatively clear periods get clearer” scheme, with the former producing 3-5 days later spring onsets.

Chapter 1

Introduction

1.1 Background and Motivations

Cloudiness is pivotal for earth's surface radiative budget (Harrison et al., 1990). In snow hydrology, the importance of cloudiness is exemplified by its role in regulating the amount of solar radiation/shortwave flux (SWF) at the snow surface (Simpson et al., 2004). In turn, SWF is the primary input component in snowmelt energy balance in mountain environment (U.S. Army Corps of Engineer, 1956; Marks and Dozier, 1992; Cline, 1997; Bales et al., 2006; Comola et al., 2015; Painter et al., 2017). Furthermore, cloudiness also modulates the longwave radiative exchange between the atmosphere and the surface (Aguado, 1985, Zhang et al., 1996; Stone, 1997; Stone et al., 2002; Harpold and Brooks, 2018). Despite these facts, cloudiness variability over mountainous terrains, along with its influence on snowmelt and runoff processes, has not been thoroughly investigated.

The underlying factor that hinders such a study is the difficulty in observing cloud cover and the associated incoming SWF at the surface, particularly over complex mountainous terrains. Fundamentally, cloud cover and, consequently, SWF have great spatial and temporal variations (Rauber, 1992), which necessitates spatially and temporally dense observation networks. However, the difficult physical access and snowy seasons severely limit our capability to setup and maintain comprehensive surface measurement networks in montane environment (Dettinger, 2014; Henn et al., 2015; Lapo et al., 2015a; Le Moine et al., 2015; Raleigh et al., 2016). For this reason, studies relating cloudiness variability and surface radiation to hydrologic variations in snow-laden mountainous settings are relatively few (e.g., Simpson et al., 2004; Pellicciotti et al, 2011; Lapo et al., 2015b).

For the same reason, hydrologic models, such as the Precipitation-Runoff Modeling System (Leavesley et al., 1983; Markstrom et al., 2015) and the Variable Infiltration Capacity (Liang et al., 1994), parameterize SWF input using algorithms based on diurnal temperature range—a proxy for cloud cover. However, the relationship between the diurnal temperature range and cloud cover is not robust (Pellicciotti et al., 2011). As a result, such algorithms can produce highly biased SWF estimates and, therefore, inaccurate snowmelt and runoff estimates (Rittger et al., 2011; Mizukami et al., 2014; Hinkelman et al., 2015; Lapo et al., 2015b; Lapo et al., 2017).

The use of satellite imageries is increasingly common and reliable for meteorological and climatological applications. In particular, the fine spatial and temporal resolutions that geostationary satellites offer allow real-time cloud cover monitoring and forecasting. This advancement has also enabled solar energy communities to assess SWF resources and yield real-time SWF estimates for solar power grids (Kleissl, 2013), reflected by the abundance of SWF algorithms that utilize satellite remote-sensed cloud products (e.g., Ineichen and Perez, 1999; Pinker et al., 2003; Perez et al., 2002, 2010; Hinkelman et al., 2012). Therefore, geostationary satellite cloud products and the associated SWF estimates offer a promising solution for hydrologic applications in mountainous catchments, where surface SWF observations are scarce.

Thus, the goals of my graduate research are:

1. To characterize spatial and temporal cloudiness variabilities over the mountain terrain of the western U.S., which will be addressed in Chapter 2 and was published in *Journal of Hydrometeorology* (Sumargo and Cayan, 2017),

2. To evaluate how this variability influences daily-seasonal snowmelt and runoff processes, which will be addressed in Chapter 3 and is currently in revision to be re-submitted to *Water Resources Research* journal (Sumargo and Cayan, 2018),
3. To examine the applicability of satellite-derived SWF estimate in hydrologic modeling, which will allow spatially and temporally comprehensive investigation of the effects of cloudiness variability and the associated SWF variations on snowmelt-runoff processes at watershed scales. This part will be addressed in Chapter 4 and is currently in preparation for submission.

The importance of addressing these goals is accentuated with climate change, since many hydrologic applications still rely on historical statistics that become less reliable as climate continues to change (Lundquist et al., 2009; Rice et al., 2011). For example, storm tracks, cloud cover patterns (Yin, 2005; Held and Soden, 2006; O’Gorman and Schneider, 2008; Dettinger, 2011) and radiative properties (Zelinka et al., 2017) are expected to evolve as a consequence of climate change. What is more, greater rain-to-snow ratio (Knowles et al., 2006), changes in winter precipitation, seasonal snowpack and annual flow (Hantel and Hirtl-Wielke, 2007; Schöner et al., 2009; Beniston, 2010; Das et al., 2011; Luce et al., 2013), and earlier streamflow timing (Stewart et al., 2005; Horton et al., 2006; Morán-Tejeda et al., 2014) are observed throughout. Climate change is also expected to decrease the snowmelt rate (Musselman et al., 2017) and summer soil moisture (Gergel et al., 2017). These factors will likely complicate the association between cloudiness variability and surface hydrologic variations, especially in mountain environment where surface energy balance and hydroclimatic processes are inherently complex (Brauchli et al., 2017).

1.2 Spatial and Temporal Scopes of the Research

The sensitivity of mountain snowpack to climate fluctuations makes mountainous regions, such as the western U.S., particularly vulnerable to climate change (Barnett et al., 2008; IPCC, 2013). Climate change can adversely impact the ecology (Diaz and Eischeid, 2007; Null et al., 2013) and hydrologic systems (Hoerling et al., 2013; Mann and Gleick, 2015; Musselman et al., 2017). It has led to earlier snow-fed streamflow (Dettinger and Cayan, 1995; Cayan et al., 2001; Stewart et al., 2005; Regonda et al., 2005) and extensively altered spring snowpack (Mote, 2003, 2006; Mote et al., 2005, 2008; Pierce et al., 2008; Kapnick and Hall, 2012; Sproles et al., 2017) and snow cover extent (Groisman and Easterling, 1994).

This sensitivity was exemplified in the recent multiyear severe drought in California [water years (WYs) 2012-2015], marked by disproportionately low spring-early summer snowpack associated with anomalous low precipitation (Mao et al., 2015; Seager et al., 2015; Williams et al., 2015). This episode was followed by the exceptionally wet WY 2017, which featured numerous Atmospheric River events (Ralph et al., 2017) and high snowpack (California Department of Water Resources, 2017; Lettenmaier, 2017). This sensitivity was similarly shown in the “snow drought” in WY 2015 in Oregon and Washington, where anomalous high temperature accompanied near-normal precipitation, resulting in lower snow-precipitation ratio (Fosu et al., 2016; Mote et al., 2016; Sproles et al., 2017).

Thus, the western U.S. makes a suitable natural laboratory for my research, which focuses on the spring-early summer period when snowmelt and runoff processes are most active.

References

- Aguado, E., 1985: Radiation balances of melting snow covers at an open site in the central Sierra Nevada, California. *Water Resour. Res.*, **21**(11), 1649-1654.
- Bales, R. C., N. P. Molotch, T. H. Painter, M. D. Dettinger, R. Rice, and J. Dozier, 2006: Mountain hydrology of the western United States. *Water Resour. Res.*, **42**(8).
- Barnett, T. P., D. W. Pierce, H. Hidalgo, C. Bonfils, B. Santer, T. Das, G. Bala, A. Wood, T. Nozawa, A. Mirin, D. Cayan, and M. Dettinger, 2008: Human-induced changes in the hydrology of the western United States. *Science*, **316**, 1080-1083.
- Beniston, M., 2010: Impacts of climatic change on water and associated economic activities in the Swiss Alps. *J. Hydrol.*, **412-413**, 291-296. doi:10.1016/j.jhydrol.2010.06.046.
- Brauchli, T., E. Trujillo, H. Huwald, and M. Lehning, 2017: Influence of slope-scale snowmelt on catchment response simulated with the Alpine3D model. *Water Resour. Res.*, **53**. <https://doi.org/10.1002/2017WR021278>
- California Department of Water Resources (2017, September). What a Difference a Year Makes. *Water Year 2017: What a Difference a Year Makes*.
- Cayan, D. R., S. Kammerdiener, M. D. Dettinger, J. M. Caprio, and D. H. Peterson, 2001: Changes in the onset of spring in the western United States. *Bull. Am. Met Soc.*, **82**(3), 399-415.
- Cline, D. W., 1997: Snow surface energy exchanges and snowmelt at a continental, midlatitude Alpine site. *Water Resour. Res.*, **33**(4), 689-701.
- Comola, F., B. Schaepli, P. Da Ronco, G. Botter, M. Bavay, A. Rinaldo, A., and M. Lehning, 2015: Scale-dependent effects of solar radiation patterns on the snow-dominated hydrologic response. *Geophys. Res. Lett.*, **42**. doi:10.1002/2015GL064075.
- Das, T., D. W. Pierce, D. R. Cayan, J. A. Vano and D. P. Lettenmaier, 2011: The importance of warm season warming to western U.S. streamflow changes. *Geophys. Res. Lett.*, **38**, L2403, doi:10.1029/2011GL049660.
- Dettinger, M., 2011: Climate change, atmospheric rivers, and floods in California—A multimodel analysis of storm frequency and magnitude changes. *J. Am. Water Resour. Assoc.*, **47**(3), 514–523, doi:10.1111/j.1752-1688.2011.00546.x.
- Dettinger, M., 2014: Climate change: Impacts in the third dimension. *Nature Geoscience*, **7**, 166–167, <https://doi.org/10.1038/ngeo2096>.
- Dettinger, M. D., and D. R. Cayan, 1995: Large-scale atmospheric forcing of recent trends toward early snowmelt runoff in California. *J. Climate*, **8**, 606-623.
- Diaz, H. F., and J. K. Eischeid, 2007: Disappearing “alpine tundra” Köppen climatic type in the western United States. *Geophys. Res. Lett.*, **34**(18).

Fosu, B. O., S. Simon Wang, and J. Yoon, 2016: The 2014/15 Snowpack Drought in Washington State and its Climate Forcing. *Bull. Amer. Meteor. Soc.*, **97**, S19–S24. <https://doi.org/10.1175/BAMS-D-16-0154.1>

Gergel, D. R., B. Nijssen, J. T. Abatzoglou, D. P. Lettenmaier, and M. R. Stumbaugh, 2017: Effects of climate change on snowpack and fire potential in the western USA. *Climatic Change*, **141**(2), 287–289.

Groisman, P.Y. and D. R. Easterling, 1994: Variability and Trends of Total Precipitation and Snowfall over the United States and Canada. *J. Climate*, **7**, 184–205. [https://doi.org/10.1175/1520-0442\(1994\)007<0184:VATOTP>2.0.CO;2](https://doi.org/10.1175/1520-0442(1994)007<0184:VATOTP>2.0.CO;2)

Hantel, M., and L. M. Hirtl-Wielke, 2007: Sensitivity of Alpine snow cover to European temperature. *Int. J. Clim.*, **27**, 1265–1275.

Harpold, A. A., and P. D. Brooks, 2018: Humidity determines snowpack ablation under a warming climate. *Proc. Natl. Acad. Sci. U.S.A.*, **201716789**. <https://doi.org/10.1073/pnas.1716789115>

Harrison, E. F., P. Minnis, B. R. Barkstrom, V. Ramanathan, R. D. Cess, and G. G. Gibson, 1990: Seasonal variation of cloud radiative forcing derived from the Earth Radiation Budget Experiment. *J. Geophys. Res. Atmos.*, **95**(D11), 18687–18703.

Held, I. M., and B. J. Soden, 2006: Robust Responses of the Hydrological Cycle to Global Warming. *J. Climate*, **19**, 5686–5699. doi: <http://dx.doi.org/10.1175/JCLI3990.1>

Henn, B., M. P. Clark, D. Kavetski, and J. D. Lundquist, 2015: Estimating mountain basin-mean precipitation from streamflow using Bayesian inference. *Water Resour. Res.*, **51**, 8012–8033. doi:10.1002/2014WR016736.

Hinkelman, L., T. Zhang, and P. Stackhouse, 2012: Comparisons of satellite-estimated radiative fluxes reaching the surface to ground observations, in *GEWEX Radiative Flux Assessment (RFA) Volume 1: Assessment*, edited by E. Raschke, S. Kinne, and P. W. Stackhouse, pp. 159–187, World Clim. Res., Programme.

Hinkelman, L. M., K. E. Lapo, N. C. Cristea, and J. D. Lundquist, 2015: Using CERES SYN Surface Irradiance Data as Forcing for Snowmelt Simulation in Complex Terrain. *J. Hydrometeorol.*, **16**, 2133–2152. doi:10.1175/JHM-D-14-0179.1.

Hoerling, M. P., M. Dettinger, K. Wolter, J. Lukas, J. Eischeid, R. Nemani, B. Liebmann, and K. E. Kunkel, 2013: Present weather and climate: Evolving conditions, in *Assessment of Climate Change in the Southwest United States: A Report Prepared for the National Climate Assessment*, edited by G. Garfin et al., pp. 74–100, A report by the Southwest Climate Alliance, Isl. Press, Washington, D. C.

Horton, P., Schaepli, B., Mezghani, A., Hingray, B., and Musy, A., 2006: Assessment of climate-change impacts on alpine discharge regimes with climate model uncertainty. *Hydrological Processes*, **20**(10), 2091–2109. <https://doi.org/10.1002/hyp.6197>

Ineichen, P., and R. Perez, 1999: Derivation of cloud index from geostationary satellites and

application to the production of solar irradiance and daylight illuminance data. *Theor. Appl. Climatol.*, **64**, 119–130.

IPCC, 2013: *Climate Change 2013: The Physical Science Basis*, Contribution of Working Group I to the Fifth Assessment Report of the Intergovernmental Panel on Climate Change (Stocker, T.F., D. Qin, G.-K. Plattner, M. Tignor, S.K. Allen, J. Boschung, A. Nauels, Y. Xia, V. Bex and P.M. Midgley (eds.)), 1535 pp., Cambridge Univ. Press, Cambridge, United Kingdom and New York, NY, USA.

Kapnick, S., and A. Hall, 2012: Causes of recent changes in western North American snowpack. *Clim. Dyn.*, **38**, 1885-99.

Kleissl, J., 2013: *Solar energy forecasting and resource assessment*, Oxford: Academic Press.

Knowles, N., M. D. Dettinger, and D. R. Cayan, 2006: Trends in snowfall versus rainfall for the western United States. *J. Clim.*, **19**(18), 4545-4559.

Lapo, K. E., L. M. Hinkelman, C. C. Landry, A. K. Massmann, and J. D. Lundquist, 2015a: A simple algorithm for identifying periods of snow accumulation on a radiometer. *Water Resour. Res.*, **51**, 7820–7828. doi:10.1002/2015WR017590.

Lapo, K. E., L. M. Hinkelman, E. Sumargo, M. Hughes, and J. D. Lundquist, 2017: A critical evaluation of modeled solar irradiance over California for hydrologic and land surface modeling. *J. Geophys. Res. Atmos.*, **122**, 299-317. doi:10.1002/2016JD025527.

Lapo, K. E., L. M. Hinkelman, M. S. Raleigh, and J. D. Lundquist, 2015b: Impact of errors in the downwelling irradiances on simulations of snow water equivalent, snow surface temperature, and the snow energy balance. *Water Resour. Res.*, **51**, 1649–1670. doi:10.1002/2014WR016259.

Le Moine, N., F. Hendrickx, J. Gailhard, R. Garçon, and F. Gottardi, 2015: Hydrologically Aided Interpolation of Daily Precipitation and Temperature Fields in a Mesoscale Alpine Catchment. *J. Hydrometeorology*, **16**, 2595–2618. <https://doi.org/10.1175/JHM-D-14-0162.1>.

Leavesley, G. H., R. W. Lichty, B. M. Troutman, and L. G. Saindon, 1983: Precipitation-runoff modeling system: User's manual. *Water-Resources Investigation Report*, 83-4238 pp., U.S. Geol. Surv.

Lettenmaier, D. P., 2017: Observational breakthroughs lead the way to improved hydrological predictions. *Water Resour. Res.*, **53**, 2591–2597. doi:10.1002/2017WR020896.

Liang, X., D. P. Lettenmaier, E. F. Wood, and S. J. Burges, 1994: A Simple hydrologically Based Model of Land Surface Water and Energy Fluxes for GSMs. *J. Geophys. Res.*, **99**(D7), 14,415-14,428.

Luce, C. H., J. T. Abatzoglou, and Z. A. Holden, 2013: The missing mountain water: Slower westerlies decrease orographic enhancement in the Pacific Northwest USA. *Science*, **342**(6164), 1360-1364. doi:10.1126/science.1242335.

- Lundquist, J. D., M. D. Dettinger, I. T. Stewart, and D. R. Cayan, 2009: Variability and trends in spring runoff in the western United States. *Climate warming in western North America: evidence and environmental effects*. University of Utah Press, Salt Lake City, Utah, USA, 63-76.
- Mann, M. E., and P. H. Gleick, 2015: Climate change and California drought in the 21st century. *Proc. Natl. Acad. Sci. U.S.A.*, **112**(13), 3858–3859. doi:10.1073/pnas.1503667112.
- Mao, Y., B. Nijssen, and D. P. Lettenmaier, 2015: Is climate change implicated in the 2013–2014 California drought? A hydrologic perspective. *Geophys. Res. Lett.*, **42**, 2805–2813. doi: 10.1002/2015GL063456.
- Marks, D., and J. Dozier, 1992: Climate and energy exchange at the snow surface in the alpine region of the Sierra Nevada: 2. Snow cover energy balance. *Water Resour. Res.*, **28**(11), 3043-3054.
- Markstrom, S. L., R. S. Regan, L. E. Hay, R. J. Viger, R. M. T. Webb, R. A. Payn, and J. H. LaFontaine, 2015: PRMS-IV, the precipitation-runoff modeling system, version 4. *U.S. Geological Survey Techniques and Methods*, book 6, chap. B7, 158 p., <http://dx.doi.org/10.3133/tm6B7>.
- Mizukami, N., M. P. Clark, A. G. Slater, L. D. Brekke, M. M. Elsner, J. R. Arnold, and S. Gangopadhyay, 2014: Hydrologic Implications of Different Large-Scale Meteorological Model Forcing Datasets in Mountainous Regions. *J. Hydrometeorol.*, **15**(1), 474–488. doi:10.1175/JHM-D-13-036.1.
- Morán-Tejeda, E., J. Lorenzo-Lacruz, J. I. López-Moreno, K. Rahman, and M. Beniston, 2014: Streamflow timing in mountain rivers in Spain: Recent changes and future projections. *J. Hydrology*, **517**, 1114-1127. doi: 10.1016/j.jhydrol.2014.06.053.
- Mote, P. W., 2003: Trends in snow water equivalent in the Pacific Northwest and their climatic causes. *Geophys. Res. Lett.*, **30**, 1601. doi:10.1029/2003GL017258
- Mote, P. W., 2006: Climate-driven variability and trends in mountain snowpack in western North America. *J. Climate*, **19**, 6209–6220.
- Mote, P. W., A. F. Hamlet, and E. Salathe, 2008: Has spring snowpack declined in the Washington Cascades?. *Hydrol. Earth Syst. Sci.*, **12**, 193–206.
- Mote, P. W., A. F. Hamlet, M. P. Clark, and D. P. Lettenmaier, 2005: Declining mountain snowpack in western North America. *Bull. Am. Met. Soc.*, **86**, 39-49.
- Mote, P. W., D. E. Rupp, S. Li, D. J. Sharp, F. Otto, P. F. Uhe, M. Xiao, D. P. Lettenmaier, H. Cullen, and R. M. Allen, M. R., 2016: Perspectives on the causes of exceptionally low 2015 snowpack in the western United States. *Geophys. Res. Lett.*, **43**, 10980-10988. doi: 10.1002/2016GL069965.
- Musselman, K. N., M. P. Clark, C. Liu, K. Ikeda, K., and R. Rasmussen, 2017: Slower snowmelt in a warmer world. *Nature Climate Change*. doi: 10.1038/NCLIMATE3225

Null, S. E., J. H. Viers, M. L. Deas, S. K. Tanaka, and J. F. Mount, 2013: Stream temperature sensitivity to climate warming in California's Sierra Nevada: impacts to coldwater habitat. *Climatic Change*, **116**(1), 149-170.

O'Gorman, P. A., and T. Schneider, 2008: The Hydrological Cycle over a Wide Range of Climates Simulated with an Idealized GCM. *J. Climate*, **21**, 3815–3832. doi: <http://dx.doi.org/10.1175/2007JCLI2065.1>

Painter, T. H., S. McKenzie Skiles, J. S. Deems, W. Tyler Brandt and J. Dozier, 2017: Variation in rising limb of Colorado River snowmelt runoff hydrograph controlled by dust radiative forcing in snow. *Geophys. Res. Lett.*, **44**. <https://doi.org/10.1002/2017GL075826>

Pellicciotti, F., T. Raschle, T. Huerlimann, M. Carezzo, and P. Burlando, 2011: Transmission of solar radiation through clouds on melting glaciers: A comparison of parameterizations and their impact on melt modeling. *J. Glaciol.*, **57**(202), 367–381. doi:10.3189/002214311796406013.

Perez, R., P. Ineichen, K. Moore, M. Kmiecik, C. Chain, R. George, and F. Vignola, 2002: A new operational model for satellite-derived irradiances: description and validation. *Solar Energy*, **73**, 307-317.

Perez, R., S. Kivalov, A. Zelenka, J. Schlemmer, and K. Hemker Jr., 2010: Improving the performance of satellite-to-irradiance models using the satellite's infrared sensors. In: *Proc. of American Solar Energy Society's Annual Conference*, Phoenix, AZ.

Pierce, D. W., T. P. Barnett, H. G. Hidalgo, T. Das, C. Bonfils, B. D. Santer, G. Bala, M. D. Dettinger, D. R. Cayan, A. Mirin, A. W. Wood, and T. Nozawa, 2008: Attribution of Declining Western U.S. Snowpack to Human Effects. *J. Climate*, **21**, 6425-6444. doi:10.1175/2008JCLI2405.1

Pinker, R. T., D. Tarpley, I. Laszlo, K. Mitchell, and P. Houser, 2003: Surface radiation budgets in support of the GEWEX Continental-Scale International Project (GCIP) and the GEWEX Americas Prediction Project (GAPP), including the North American Land Data Assimilation System (NLDAS) project. *J. Geophys. Res.*, **108**(D22), 8844. doi:10.1029/2002JD003301.

Raleigh, M. S., B. Livneh, K. Lapo, and J. D. Lundquist, 2016: How Does Availability of Meteorological Forcing Data Impact Physically Based Snowpack Simulations?. *J. Hydrometeorology*, **17**, 99–120. <https://doi.org/10.1175/JHM-D-14-0235.1>.

Ralph, F. M., C. Hecht, and B. Kawzenuk, 2017: How Many Atmospheric Rivers Have Hit the U.S. West Coast During the Remarkably Wet Water Year 2017?. Accessed 15 January 2018, <http://cw3e.ucsd.edu/how-many-atmospheric-rivers-have-hit-the-u-s-west-coast-during-the-remarkably-wet-water-year-2017/>

Rauber, R. M., 1992: Microphysical Structure and Evolution of a Central Sierra Nevada Orographic Cloud System. *J. Appl. Meteor.*, **31**, 3–24. doi: [http://dx.doi.org/10.1175/1520-0450\(1992\)031<0003:MSAEOA>2.0.CO;2](http://dx.doi.org/10.1175/1520-0450(1992)031<0003:MSAEOA>2.0.CO;2).

- Regonda, S. K., B. Rajagopalan, M. Clark, and J. Pitlick, 2005: Seasonal cycle shifts in hydroclimatology over the western United States. *J. Climate*, **18**, 372–384.
- Rice, R., R. C. Bales, T. H. Painter, and J. Dozier, 2011: Snow water equivalent along elevation gradients in the Merced and Tuolumne River basins of the Sierra Nevada. *Water Resour. Res.*, **47**, W08515, doi:10.1029/2010WR009278.
- Rittger, K., A. Kahl, and J. Dozier, 2011: Topographic distribution of snow water equivalent in the Sierra Nevada, *Proc. Western Snow Conf.*, **79**, 37–46.
- Schöner, W., I. Auer, and R. Böhm, 2009: Long term trend of snow depth at Sonnblick (Austrian Alps) and its relation to climate change. *Hyrdol. Process*, **23**, 1052–1063.
- Seager, R., M. Hoerling, S. Schubert, H. Wang, B. Lyon, A. Kumar, J. Nakamura, and N. Henderson, 2015: Causes of the 2011–14 California Drought. *J. Climate*, **28**, 6997–7024. <https://doi.org/10.1175/JCLI-D-14-00860.1>
- Simpson, J. J., M. D. Dettinger, F. Gehrke, T. J. McIntire, and G. L. Hufford, 2004: Hydrologic scales, cloud variability, remote sensing, and models: Implications for forecasting snowmelt and streamflow. *Weather and forecasting*, **19**(2), 251–276.
- Sproles, E. A., T. R. Roth, and A. W. Nolin, 2017: Future snow? A spatial-probabilistic assessment of the extraordinarily low snowpacks of 2014 and 2015 in the Oregon Cascades. *The Cryosphere*, **11**, 331–341. doi:10.5194/tc-11-331-2017.
- Stewart, I. T., D. R. Cayan, and M. D. Dettinger, 2005: Changes towards earlier streamflow timing across western North America. *J. Climate*, **18**, 1136–1155.
- Stone, R. S., 1997: Variations in western Arctic temperatures in response to cloud- radiative and synoptic-scale influences. *J. Geophys. Res.*, **102**(D18), 21,769 – 21,776.
- Stone, R. S., E. G. Dutton, J. M. Harris, and D. Longenecker, 2002: Earlier spring snowmelt in northern Alaska as an indicator of climate change. *J. Geophys. Res.*, **107**(D10), 4089. doi:10.1029/2000JD000286.
- Sumargo, E., and D. R. Cayan, 2017: Variability of cloudiness over mountain terrain in the Western United States. *J. Hydrometeorol.*, **18**, 1227–1245. <https://doi.org/10.1175/JHM-D-16-0194.1>.
- Sumargo, E., and D. R. Cayan, 2018: The influence of cloudiness on hydrologic fluctuations in the mountains of the western United States. *Submitted for publication in Water Resour. Res.*
- U.S. Army Corps of Engineers, 1956: *Snow hydrology: Summary report of the snow investigations*. North Pacific Division, U.S. Army Corps of Engineers, 437 pp.
- Williams, A. P., R. Seager, J. T. Abatzoglou, B. I. Cook, J. E. Smerdon, and E. R. Cook, 2015: Contribution of anthropogenic warming to California drought during 2012–2014. *Geophys. Res. Lett.*, **42**, 6819–6828. doi:10.1002/2015GL064924.

Yin, J. H., 2005: A consistent poleward shift of the storm tracks in simulations of 21st century climate. *Geophys. Res. Lett.*, **32**, L18701, doi:10.1029/2005GL023684.

Zelinka, M. D., D. A. Randall, M. J. Webb, and S. A. Klein, 2017: Clearing clouds of uncertainty. *Nat. Climate Change*, **7**, 674-678. doi:10.1038/nclimate3402.

Zhang, T., K. Stamnes, and S. A. Bowling, 1996: Impact of clouds on surface radiative fluxes and snowmelt in the Arctic and Subarctic. *J. Climate*, **9**, 2110–2123.

Chapter 2

Variability of Cloudiness over Mountain Terrain in the Western United States

This study investigates the spatial and temporal variability of cloudiness across mountain zones in the western United States. Daily average cloud albedo is derived from a 19-year series (1996-2014) of half-hourly Geostationary Operational Environmental Satellite (GOES) images. During springtime when incident radiation is active in driving snowmelt-runoff processes, the magnitude of daily cloud variations can exceed 50% of long-term averages. Even when aggregated over three-month periods, cloud albedo varies by $\pm 10\%$ of long-term averages in many locations. Rotated empirical orthogonal functions (REOFs) of daily cloud albedo anomalies over high elevation regions of western conterminous U.S. identify distinct regional patterns, wherein the first five REOFs account for $\sim 67\%$ of the total variance. REOF1 is centered over northern California and Oregon and is pronounced between November and March. REOF2 is centered over the interior northwest and is accentuated between March and July. Each of the REOF/PC modes associates with anomalous large scale atmospheric circulation patterns and one or more large-scale teleconnection indices (AO, Niño 3.4 and PNA), which helps to explain why anomalous cloudiness patterns take on regional spatial scales and contain substantial variability over seasonal time scales.

2.1 Introduction

Understanding spatial and temporal variability of cloudiness is a long-standing problem (e.g., Welch et al., 1988; Seze and Rossow, 1991; Rossow, 2002; Simpson et al.,

2004). A better determination of recent historical variability is yet more important in the light of climate change, which may affect storm tracks and cloud patterns (Yin, 2005; Held and Soden, 2006; O’Gorman and Schneider, 2008; Dettinger, 2011). Cloud variability in mountain settings is enigmatic because clouds and radiation are not well-monitored by surface observers, because cloudiness depends on several factors at multiple scales including storm tracks and cloud life cycles, and because topographic features can change the cloud systems on relatively short spatial and temporal scales (Rauber, 1992). The present work addresses this complexity by identifying the extent to which the cloudiness in mountain zones is organized over large regional scales and how it varies temporally.

In the mountains of the western United States (U.S.), precipitation is largely delivered as snow from cool season storms (Serreze et al., 1999). Snowpack provides water storage (Mote, 2006) and is an integral part of the hydrologic cycle in the region (Pierce et al., 2008; Pierce and Cayan, 2013). In snow-fed watersheds, net solar radiation is the primary energy input for spring snowmelt (U.S. Army Corps of Engineers, 1956), providing 66–90% of energy needed for snowmelt (Marks and Dozier, 1992; Cline, 1997). Varying cloudiness comes into play in modulating this solar heating and the associated snowmelt, a process that continues into the summer. In their study of hydrologic responses in the upper Colorado River basin, Mizukami et al. (2014) reported a difference of 85 W m^{-2} in shortwave radiation in May, which translated to a difference of 273 mm snowmelt at elevations above 3 km, contributing to the differences of ~20% in annual runoff and ~20 days in the timing of snowmelt and runoff.

Diurnal and annual cycles of solar energy reaching the surface are controlled by solar geometry, but the anomalous solar variations depend on the structure and evolution of clouds

(Kleissl, 2013). Consequently, cloud cover variations are the principal regulator of solar insolation at synoptic to inter-annual time scales (Smith et al., 1992; Ringer and Shine, 1997). Cloudiness also affects longwave radiation exchange with the surface (Aguado, 1985). Therefore, understanding cloud variability is needed to comprehensively explain the spatial and temporal variations of surface processes, particularly the fluctuating patterns of hydrologic measures over the mountainous western U.S.

Although clouds are a major regulator of the energy budget, their optical properties vary over a range of spatial scales, so describing the incoming radiation using radiative transfer modeling is not feasible (Gimeno García et al., 2012). Additionally, *in situ* radiation measurements are difficult in mountainous settings because complex topography and snow-laden seasons hinder necessary ground-based observations. Moreover, surface point radiation measurements generally lack the scope required to portray spatial and temporal structure over the broader region. As a result, clouds and surface radiation in mountainous terrains have been inadequately described (Gautier et al., 1980; Bales et al., 2006).

A direct impact of this inadequacy is reflected in hydrologic modeling and related applications, e.g., in Precipitation-Runoff Modeling System (PRMS) (Leavesley et al., 1983; Markstrom et al., 2015), wherein daily surface air temperature range is used as a proxy for cloud cover to estimate surface radiation. This can introduce errors in water supply forecasts (Rittger et al., 2011) by producing biases in estimating snowmelt rate (Lapo et al., 2015) and runoff timing (Hinkelman et al., 2015).

Studies using space-borne measurements have demonstrated the merit of remotely sensed snow albedo as input to a snowmelt model (Molotch et al., 2004), to investigate snow cover area under forest canopies (Raleigh et al., 2011) and to map snow cover (Rittger et al.,

2013). Geostationary satellite estimates of surface irradiance are increasingly common (e.g., Cano et al., 1986; Ineichen and Perez, 1999; Perez et al., 2002, 2010), since they provide the most accurate option for locations >25 km away from a ground station (Zelenka et al., 1999; Paulescu et al., 2012).

The availability of two decades of remote-sensed cloud measures, along with an increasing reliance on remote-sensed radiation measures (e.g., Bales et al., 2006; Khan et al., 2011), motivates us to investigate the variability of cloudiness over western U.S. mountain settings. Cloud variability during the hydrologically important winter-to-summer period is emphasized here. While the occurrence of long period, globally patterned changes in cloudiness is becoming clearer (Dai et al., 2006; Warren et al., 2007; Eastman and Warren, 2013; Norris et al., 2016), the 19-year GOES dataset used in this study is too short to resolve such changes. Accordingly, our focus here is to understand cloudiness variability from daily to seasonal time scales.

2.2 Datasets

2.2.1 GOES-West visible cloud albedo

The cloud measures explored here are derived from NASA/NOAA Geostationary Operational Environmental Satellite (GOES) images collected at half-hourly intervals from 1996 to 2014. GOES captures a large swath simultaneously throughout the day (<http://noaasis.noaa.gov/NOAASIS/ml/genlsatl.html>). The GOES radiometer provides an albedo measure defined as the ratio of reflected to incident radiation from the surface, i.e., the reflectivity. As cloud cover increases, the albedo increases and the downwelling surface radiation decreases (Ramanathan et al., 1989; Iacobellis and Cayan, 2013).

This study utilizes GOES-West (9, 10, 11 and 15) visible albedo measurements with 1-km horizontal and 30-minute temporal resolutions retrieved from NOAA Comprehensive Large Array-data Stewardship System (<http://www.nsof.class.noaa.gov>). The 1-km pixels are spatially aggregated to 4-km pixels to alleviate the computational burden. The GOES data in this study encompasses the westernmost U.S. and adjacent eastern North Pacific domain (25-50 °N, 130-113 °W), and spans the period 1996-2014. The albedo observations are adjusted by removing the estimated clear-sky albedo to derive cloud albedo values (section 2.3.1).

Mountain clouds can vary considerably within the period of a day in response to synoptic events and topographically forced diurnal circulations. To minimize the impact of these shorter period variations, cloud albedo is averaged over daytime scenes [0800-1600 Local Standard Time (LST)]. The vast majority of days (>80%) have at least 15 half-hour observations. A sampling exercise that constructed the daily average from successively smaller numbers of observations per day determined that 10 out of 17 possible half-hourly data yielded a reasonable estimate of the daytime average albedo (appendix 2A). The daytime average albedo is the fundamental measure of cloudiness used throughout the paper.

2.2.2 Gridded elevation data

Gridded elevation data with 2-minute cell size are downloaded from the NOAA National Geophysical Data Center (NGDC) GEODAS Grid Translator Design-a-Grid website (http://www.ngdc.noaa.gov/mgg/gdas/gd_designagrid.html). The output latitude-longitude boxes are then interpolated to the 4-km GOES pixels using shortest distance interpolation method to discriminate the high-elevation GOES pixels from the low-elevation GOES pixels (section 2.3.3).

2.2.3 Reanalyzed meteorological data and low frequency weather anomalies indices

This study utilizes the (0.3°x0.3°) North American Regional Reanalysis (NARR, Mesinger et al., 2006) provided by NOAA Physical Sciences Division/PSD to investigate the associations with larger-scale meteorological patterns. Connections between cloud variability and climate patterns are also examined using a set of low frequency weather anomalies metrics commonly known as teleconnection indices (Wallace and Gutzler, 1981; Franzke et al., 2001). These metrics include the monthly versions of Pacific North American (PNA), of the Arctic Oscillation (AO), and of Niño 3.4 indices from the NOAA Climate Prediction Center database (<http://www.cpc.ncep.noaa.gov/>).

2.3 Methods

2.3.1 Determining the clear-sky albedo and the cloud albedo

GOES albedo (α) is controlled by both clouds and other non-cloud factors. The non-cloud component of albedo, i.e., clear-sky albedo (α_{clear}), is dominated by changing surface characteristics (e.g., snow covered vs. not snow covered) as well as changes in clear atmospheric components (e.g., aerosol). The cloud component of albedo, hereby called cloud albedo (α_{cloud}), is determined as the difference between α and α_{clear} :

$$\alpha_{cloud} = \alpha - \alpha_{clear} \quad (2.1)$$

α_{clear} evolves over time in response to local albedo variations at and near the surface, chiefly consisting of snow, moisture and vegetation (Perez et al., 2002). α_{clear} is calculated and subtracted from α separately for each individual half-hour of the day since surface reflectance can be dependent on the angle of incoming solar radiation (Iacobellis and Cayan, 2013). The

units of the albedos are percent, ranging from 0% (transparent) to 100% (opaque).

α_{clear} is derived using a sliding time window algorithm (Cano et al., 1986; Perez et al., 2002), such that α_{clear} is the minimum α observed at a particular pixel within a prescribed time window. A time window centered on a given target day (after Paech et al., 2009) is used to determine the minimum albedo value (α_{clear}), under the likely assumption that there is at least one clear-weather day within this time window for each particular half-hour. This algorithm is based on the premise that clouds are non-stationary and thus the minimum value of daily mean α observed at each pixel can provide a reference albedo map (Cano et al., 1986), which in this case is α_{clear} . A set of time windows was investigated to determine their ability to capture fluctuations from changing surface properties. This experimentation indicated that a sliding 15-day window of ± 7 days was able to balance the need to sample a long enough period to include a clear-sky day within the window and the need to make the window narrow enough to capture relatively short time scale changes in surface characteristics (appendix 2B). Figure 2.1 illustrates the resulting α_{clear} and α_{cloud} estimates over a period that includes an abrupt deposit of snow cover during a winter storm from 30 November 2005 to 4 December 2005.

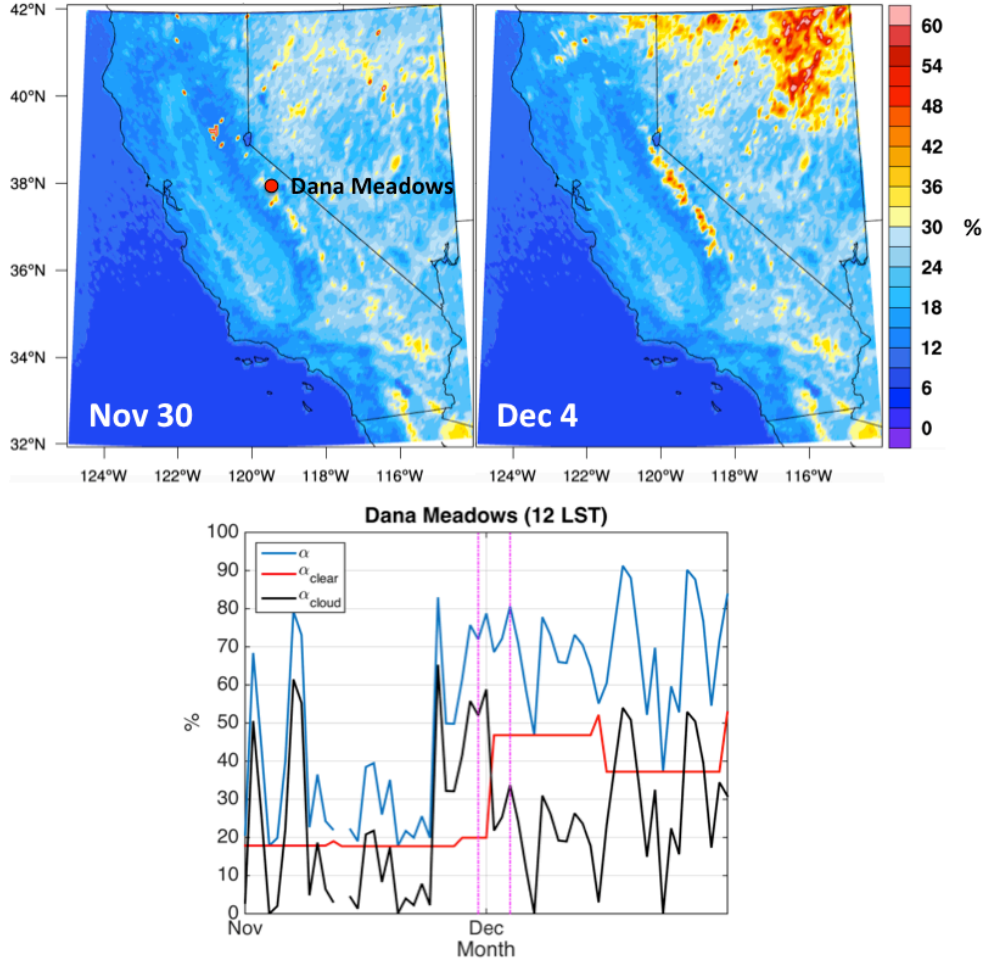


Figure 2.1. (Top) Estimated daily mean (0800-1600 LST) α_{clear} over California and Nevada before and after 1-3 December 2005 snowstorm. (Bottom) November and December 2005 time-series of local noontime α (blue) and the estimated α_{clear} (red) and α_{cloud} (black) at GOES pixel overhead Dana Meadows in Yosemite National Park (37.9 °N, 119.26 °W, 2,987 m elevation). The vertical magenta lines denote 30 November 2005 and 4 December 2005.

2.3.2 Quantifying solar insolation sensitivity to cloudiness variation

The influence of cloudiness on incoming solar radiation at the surface [hereby called Shortwave Flux (SWF)] is quantified from a simple sensitivity measure where SWF is a linear function of α_{cloud} :

$$SWF = (100\% - \alpha_{cloud}) * SWF_{clear} \quad (2.2)$$

such that the response or sensitivity of SWF is determined as:

$$\Delta SWF = \Delta \alpha_{cloud} * SWF_{clear} \quad (2.3)$$

SWF_{clear} is theoretical clear-sky SWF calculated as a function of geo-location and time of the year (see <http://maeresearch.ucsd.edu/kleissl/files/R.m> for documentation). To investigate the effect of cloud variations, we evaluate the response of SWF to a 10% increase in α_{cloud} ($\Delta \alpha_{cloud} = 10\%$). The resultant linear response is presented for every season and at four representative locations spread across the western U.S. to examine ΔSWF at different areas and different times of the year. Additionally, the linear response derived from observed solar irradiance records from radiometers at selected Sierra Nevada sites are employed.

2.3.3 Low elevation mask

Our GOES albedo dataset includes all pixels, regardless of altitude, within the western U.S.-eastern North Pacific domain. In several of our analyses, we wish to focus upon cloud variability that occurs over the higher terrain, without including stratus cloud influences and other possible valley and low elevation effects. For these high terrain analyses, GOES pixels with elevations of less than 800 meters are masked using the gridded elevation data to focus on cloudiness over higher elevation terrain.

2.3.4 Removing the seasonal cycle of α_{cloud} and meteorological variables

The estimated seasonal cycle of α_{cloud} is removed using the daily climatology (average) of α_{cloud} at each individual pixel. After considering different estimators of the seasonal cycle, we adopt a long-term (19-year) average of the daily α_{cloud} wherein the daily average values are smoothed using a 29-day (± 14 days) centered moving average to reduce high frequency sampling noise (appendix 2C). The “de-seasonalized” α_{cloud} is defined as the

difference between α_{cloud} and the smoothed daily climatology. The resulting de-seasonalized residuals provide a description of higher frequency (intra-seasonal) weather and climatic phenomena.

2.3.5 Rotated Empirical Orthogonal Function (REOF) of daily cloud anomalies

Empirical Orthogonal Function (EOF) analysis (Lorenz, 1956; Davis, 1976; Hannachi, 2004) is employed to decompose space-time variations in daily α_{cloud} into orthogonal spatial eigenvector patterns (or simply EOFs) and their corresponding temporal amplitude time-series, called Principal Components (PCs) (Hannachi, 2004). To ensure physically meaningful spatial structures, rotated EOFs (REOFs; Richman, 1986; Hannachi, 2004; Monahan et al., 2009) are constructed using Kaiser row normalization and a varimax criterion (Kaiser, 1958), which are constrained to be orthogonal in time only.

The varimax rotation is applied to the five leading EOF modes of the de-seasonalized α_{cloud} , all days of the year (January-December) over the 19-year period (1996-2014), from pixels with elevations of at least 800 meters above sea level. A set of time varying coefficients, or rotated principal components (RPCs) was also derived. When the REOF analysis is repeated for four-month blocks, e.g., February-May, June-September, and April-July, instead of the entire year, the results yield nearly identical patterns for the five leading REOF modes, only ordered differently according to the variance explained. In each of the four-month and all-year analyses, the five leading modes account for 60% or more of the total variance. Moreover, the 6th mode in the all-year analysis accounts for 3.1% of the total variance, a significant drop from the 5th mode (9.5%). Therefore, only the five leading modes are presented in this paper.

2.3.6 Composites based upon extreme RPC values

December-August days within the 1996-2014 period with the most positive and negative RPC values are identified to represent the cloudiest and clearest days during winter-to-summer period when snow accumulation and melt are most active. The cloudiest days in the REOF core regions are determined as days with RPC values $> 90^{\text{th}}$ percentile, while the clearest days are determined as days with RPC values $< 10^{\text{th}}$ percentile. Given these subsets of cloudiest and clearest days, composites of anomaly fields of pertinent variables were formed to investigate the association of the cloudiness patterns with surface weather variables and atmospheric circulation patterns. For the latter, the NOAA PSD website (<http://www.esrl.noaa.gov/psd/cgi-bin/data/narr/plotday.pl>) was used to generate NARR composite datasets corresponding to the REOF/RPC modes.

2.3.7 Contingencies based upon extreme RPC values

2-by-2 contingency tables (Pearson, 1904; Wilks, 1995, Done et al., 2004) are constructed to examine how positive and negative anomalies of each RPC mode associate with positive and negative anomalies of the selected teleconnection indices. The days corresponding to the most positive ($>75^{\text{th}}$ percentile) and negative ($<25^{\text{th}}$ percentile) indices are identified. The cloudiest ($>75^{\text{th}}$ percentile) and clearest ($<25^{\text{th}}$ percentile) days corresponding to each RPC mode are also identified. This criterion is applied to the high positive and negative states of the AO, Niño 3.4 and PNA indices, so the cells of the 2-by-2 tables represent the number of days associated with high positive and

negative phases of each teleconnection index and the number of days of high positive or negative phase of each RPC.

The ϕ coefficients and χ^2 statistics (Pearson, 1904; Howell, 2011) are subsequently computed to determine the correlation and statistical significance of the associations between the RPC modes and the teleconnection indices. The ϕ coefficient is analogous to Pearson's correlation coefficient, although it must be noted that the maximum value of ϕ is not necessarily ± 1 (Davenport and El-Sanhurry, 1991).

2.4 Results and discussion

2.4.1 α_{cloud} variability on daily to inter-annual time scales

The magnitude of α_{cloud} variations at daily and inter-annual time scales is investigated by computing the mean (μ), standard deviation (σ) and the coefficient of variation ($CV = \sigma/\mu$) of α_{cloud} for winter (DJF), spring (MAM), summer (JJA) and autumn (SON), separately, at each GOES pixel (all elevations) across the western U.S from the 1996-2014 data. The maps showing the three-month aggregates of σ and CV are displayed in Figure 2.2 for intra-seasonal daily anomalies and in Figure 2.3 for inter-annual seasonal anomalies. The mean values (μ) are identical in both intra-seasonal and inter-annual cases, so they are displayed in Figure 2.2 only. Figures 2.2 and 2.3 illustrate DJF, MAM and JJA to focus on periods when cloudiness variability has the most important influence on snowpack dynamics. The figures include offshore regions to compare coastal and lowland cloud variability to that of the higher elevation terrestrial regions of the western U.S. The albedo mean and variability statistics of representative regions for all four seasons are presented in Table 2.1.

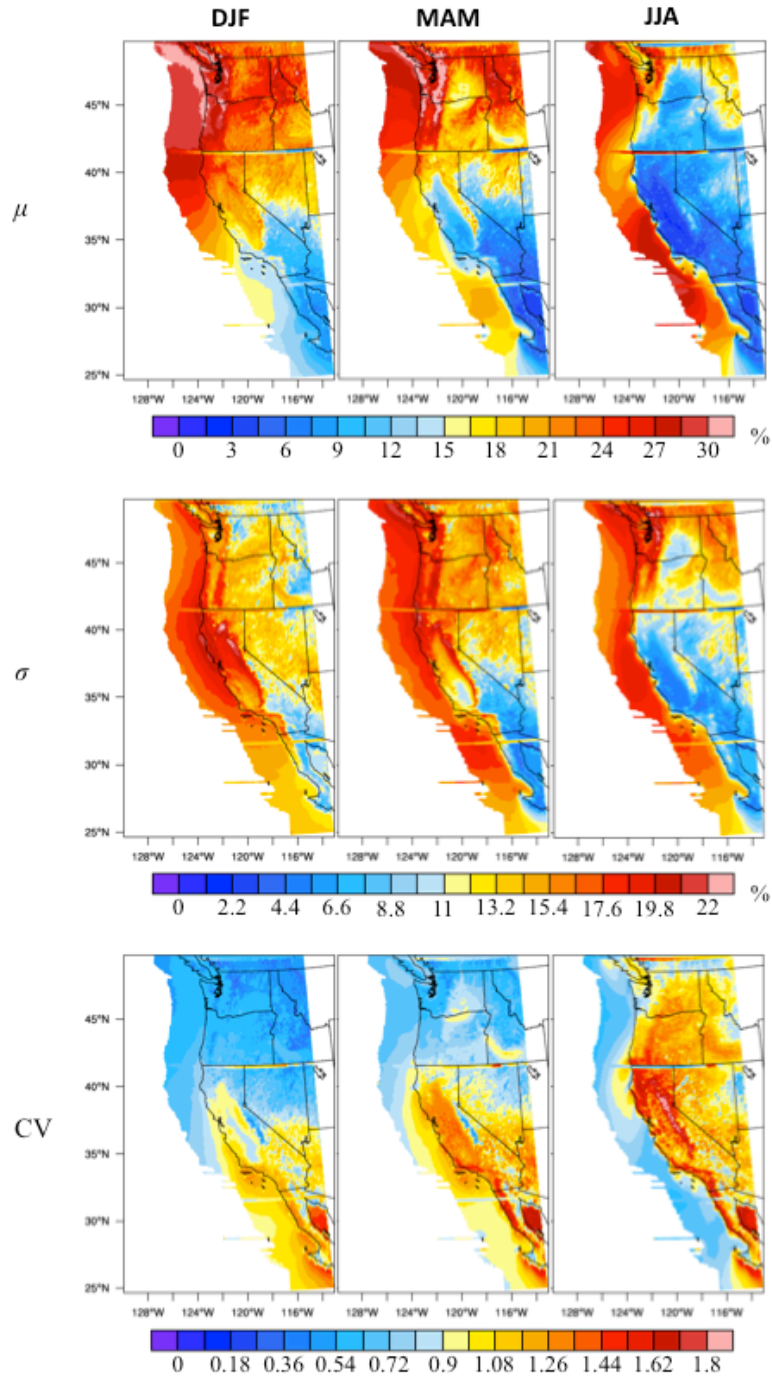


Figure 2.2. Maps of mean (μ), standard deviation (σ) and coefficient of variation (CV) of daily α_{cloud} for winter (DJF), spring (MAM) and summer (JJA).

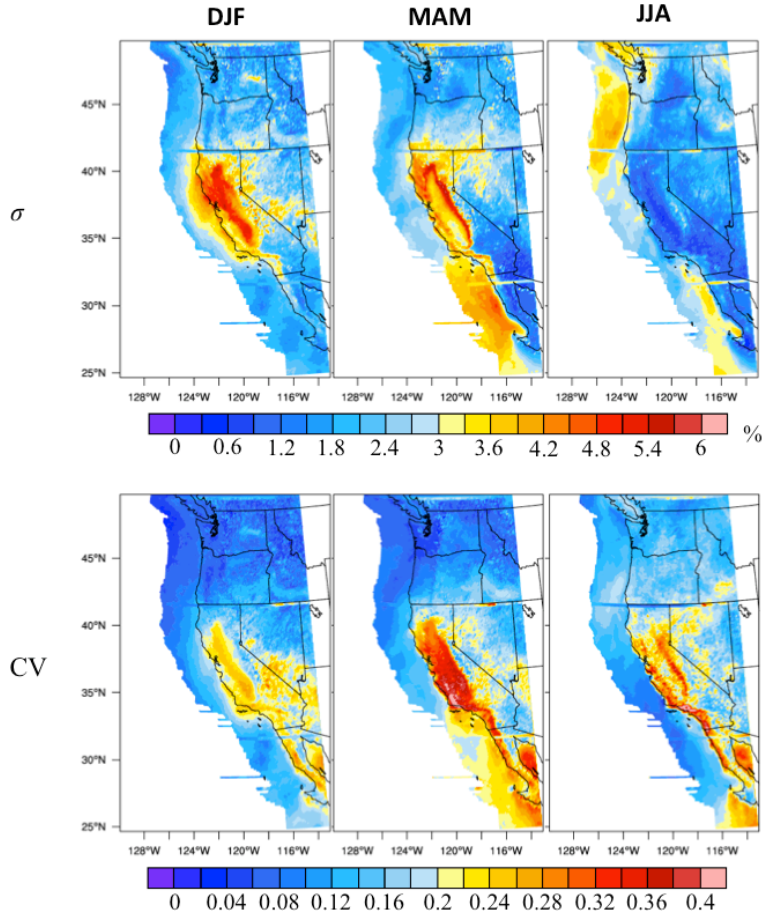


Figure 2.3. DJF, MAM and JJA standard deviation and coefficient of variation calculated from seasonal (three-month) α_{cloud} averages. Means for the seasonal averages are same as those in Figure 2.2, so are not shown. Note change in color scales from those in Figure 2.2.

Table 2.1. Daily and seasonal means (μ) and standard deviations (σ) of α_{cloud} in percent and the coefficients of variations (CV) for winter (DJF), spring (MAM), summer (JJA), and autumn (SON). The two tabulations are aggregates over the mountains in California and Oregon, and over the mountains in Idaho, Montana and eastern Washington.

Time scale	Season	Region 1 (CA-OR)			Region 2 (ID-MT-WA)		
		μ	σ	CV	μ	σ	CV
Daily	DJF	22.4	11.3	0.50	24.7	8.1	0.33
	MAM	19.8	13.0	0.66	24.8	12.1	0.49
	JJA	9.1	8.6	0.94	16.5	12.2	0.74
	SON	14.9	11.5	0.77	22.3	13.8	0.62
Seasonal	DJF	22.4	2.6	0.12	24.7	1.2	0.05
	MAM	19.8	2.8	0.14	24.8	1.4	0.06
	JJA	9.2	1.2	0.13	16.6	2.1	0.12
	SON	14.8	2.3	0.15	22.1	1.9	0.09

Seasonal means of α_{cloud} range from as low as 6% to as high as 30%. Cloudiness is greatest in the offshore and near-shore coastal lowlands, and over mountainous terrains of the coast range, the Cascades, the northern Rockies and the Sierra Nevada (Figure 2.2, top panel). Over land, cloudiness tends to be greater north of San Francisco than to its south. A well-defined seasonality is observed over much of the western U.S. land mass, with greatest cloudiness in winter and least in summer. This contrasts with offshore and coastal lowland marine cloudiness in California, which peaks in summer (Clemesha et al., 2016), and illustrates the distinct physical mechanisms driving cloud formations. While subsiding air masses and low-level inversions are involved in marine layer clouds, synoptic-scale weather systems, e.g., Pacific cold fronts, are the primary generator of cool season mountain clouds. These synoptic systems produce spatially coherent cloudiness from offshore Pacific Northwest to the Cascades and Sierra Nevada.

The variability of daily α_{cloud} , represented by σ (Figure 2.2, middle panel), ranges from ~2% to >20%. On daily time scales, σ is highest over the coastal ocean and coastal lowlands and over the western slopes of mountain ranges. Regions with greater μ usually exhibit greater daily σ , including inland areas in California where both daily μ and σ are high in winter and spring. In California, this pattern demonstrates the strong influence of synoptic weather patterns in determining the enhanced average and time varying cloudiness in winter and spring months. However, over the interior Pacific Northwest in winter and spring, μ is high but σ is reduced, suggesting more persistent cloudiness. In the interior Pacific Northwest, the variability is heightened in summer and rather isolated from that over the coasts, indicative of regional processes including local convective activities.

Daily α_{cloud} CV (Figure 2.2, bottom panel) provides a different perspective of the variability since they are scaled by their mean values, so a higher CV denotes increased variability relative to average conditions. The CV is generally higher in the south than in the north, an indication of the important role played by time varying cloudiness in a region with lower overall mean cloudiness such as the southwestern U.S., or particularly California. In DJF and MAM, the daily CV is pronounced along the eastern side of the Sierra Nevada rather than along the Sierra range itself, probably related to the irregular occurrence of mountain cloud formations including wave cloud that Grubišić and Billings (2008) found in spring and, even more variably, in winter. The high CV in California continues through JJA, which reflects the intermittent orographic thunderstorms that are common over the plateaus and mountains of the western U.S. during summertime (Kelly et al., 1985; Whiteman, 2000).

Turning to seasonal time scales (Figure 2.3), it is important to know how much variability remains when α_{cloud} is time-averaged, since persistent fluctuations of incoming radiation could affect seasonal anomalies of precipitation, snowmelt and other surface processes. Although their magnitudes are reduced, σ and CV patterns derived from ~ 90 -day average α_{cloud} are qualitatively similar those from daily α_{cloud} , but they are accentuated in different regions. Importantly, the seasonal σ tends to be greatest in California, in contrast to daily σ , which is generally greatest in the Pacific Northwest. This daily-seasonal contrast indicates the regional significance of seasonal α_{cloud} variability in California, especially during snowmelt season when the variability is emphasized over the west of Sierra Nevada.

From year to year, seasonal α_{cloud} deviations range from about 4% to 40% of mean α_{cloud} , as shown by the seasonal CV (Figure 2.3, lower panel). Traversing central California, seasonal CVs exceed 0.18 from the California coast across the Central Valley and up the

Sierra Nevada slope, and also over neighboring high elevations of western Nevada, southern Oregon, and southern Idaho. In contrast, over the Pacific Northwest, seasonal CVs are low in DJF and MAM, reflecting high mean cloudiness and relatively low inter-annual variation.

2.4.2 Sensitivity of solar insolation to cloudiness variability

Using Eq. (2.3), the change in SWF associated with a given change in α_{cloud} can be determined. Considering a set of selected locations (Table 2.2), the magnitude of daytime (0800-1600 LST) average Δ SWF, expressed as the response of SWF to a 10% increase in α_{cloud} , ranges from ~ 66 to ~ 84 $W\ m^{-2}$ over spring and summer when snowmelt activity is prominent; this range of Δ SWF is representative of Δ SWF determined for a larger set of 239 high-altitude (≥ 800 meters) locations ($64-84$ $W\ m^{-2}$). Furthermore, these calculated responses are comparable to those directly observed at the surface, via a least-squares regression analysis, between α_{cloud} and surface pyranometer SWF at high-elevation stations in California. For example, a 10% increase in α_{cloud} at Dana Meadows and at nearby Tuolumne Meadows ($37.873^\circ N$, $119.35^\circ W$, 2,621 m) results in a 77-91 $W\ m^{-2}$ SWF reduction over spring and summer.

Table 2.2. Change in daily solar irradiance (SWF) at the surface corresponding to a 10% increase in daily α_{cloud} estimated for two Region 1 locations [Dana Meadows, CA ($37.9^\circ N$, $119.26^\circ W$, 2,987 m), and Fish Lake, OR ($42.38^\circ N$, $122.35^\circ W$, 1,420 m)] and two Region 2 locations [Crater Meadows, ID ($46.56^\circ N$, $115.29^\circ W$, 1,817 m), and Quartz Peak, WA ($47.88^\circ N$, $117.09^\circ W$, 1,433 m)]. A negative Δ SWF denotes reduced SWF associated with increased α_{cloud} .

Season	$\Delta\alpha_{cloud}$ (%)	Δ SWF ($W\ m^{-2}$)			
		Dana Meadows	Fish Lake	Crater Meadows	Quartz Peak
DJF	10	-43.3	-35.3	-29.8	-27.6
MAM	10	-76.4	-70.2	-67.5	-65.8
JJA	10	-84.1	-78.9	-77.5	-76.1
SON	10	-56.2	-49.0	-43.9	-42.1

Table 2.2. Continued

*The sensitivity values are based on daily time-series of α_{cloud} and SWF_{clear} . The daily SWF_{clear} is an average of hourly SWF_{clear} during daytime only (0800-1600 LST).

2.4.3 Coherent patterns of daily α_{cloud} variability

To extract the dominant patterns of cloud variability over the mountains of the western U.S., REOF analysis is performed on the de-seasonalized daily α_{cloud} over high-elevation (≥ 800 meters) terrain, encompassing all months (January-December) of 1996-2014. By design, the leading REOF patterns are the ones whose α_{cloud} anomaly patterns occupy a relatively large spatial scale and thus avoid the complexity introduced by smaller scale higher order patterns. Collectively, these five REOFs account for a considerable amount of the variability of mountain cloudiness, amounting to 66.7% of the total daily variance (Table 2.3).

Table 2.3. The eigenvalues of α_{cloud} REOFs/RPCs 1-5 and the specific geographical areas where each mode is pronounced. The eigenvalue represents the amount of variance explained by each mode.

REOF/RPC	Eigenvalue (%)	Geographical Emphasis
1	20.4	Northern California and Oregon
2	15.1	Interior Pacific Northwest
3	11.2	Coastal Pacific Northwest
4	10.5	Southwestern U.S.
5	9.5	Great Basin

Correlations between the five leading RPCs and de-seasonalized α_{cloud} are strongest over high-elevation areas where the REOFs are accentuated, and rapidly degrade over adjacent lower-elevation areas (Figure 2.4). REOF1 represents daily α_{cloud} anomalies that are pronounced in the mountainous region of northern California and Oregon, including the Sierra Nevada and the Oregon Cascades. REOF2 represents daily α_{cloud} anomalies centered

over the interior northwest covering Idaho, western Montana, eastern Oregon and eastern Washington. REOF3 is concentrated over the Cascade mountain range in western Oregon and Washington. REOF4 has greatest weightings in southern California, Nevada, and parts of Utah and Arizona. REOF5 represents daily α_{cloud} anomalies focused on the eastern two thirds of Nevada and Idaho. Each of the five leading REOFs has core areas that partially overlap with those of other REOFs because, unlike in EOF analysis, the spatial orthogonality has been relaxed in REOF analysis. For instance, both REOF1 and REOF2 contain a footprint over northeastern Oregon.

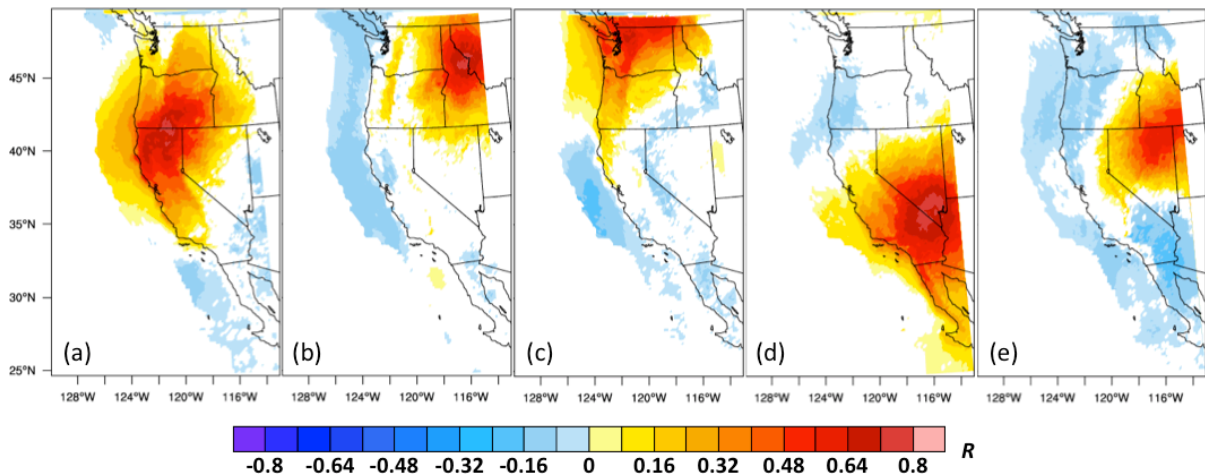


Figure 2.4. Correlation (R) fields (all months of 1996-2014) between de-seasonalized daily α_{cloud} and (a) RPC1, (b) RPC2, (c) RPC3, (d) RPC4, and (e) RPC5 over the entire domain. Only pixels with p -value < 0.05 are colored.

When a separate REOF analysis was applied to daily α_{cloud} anomalies over all elevations (not shown), the same five higher elevation-oriented modes appeared, but not in the same order and in the midst of other REOFs that represent lower-elevation cloudiness, primarily over the eastern Pacific Ocean and coastal lowlands. This confirms the authenticity

of the original α_{cloud} REOFs and the distinction between these higher elevation modes from those that are organized over lower elevations.

While there is some degree of spatial overlap between the five REOFs, by construction their temporal variability is statistically independent—the RPCs are temporally orthogonal. Although each RPC has a time mean of zero for each day of the year, the magnitude of month-to-month RPC fluctuations still contains substantial seasonal variability, as shown by their monthly standard deviations (Figure 2.5).

The variability of RPCs 1, 3 and 4 exhibits a well-defined annual cycle, while that of RPCs 2 and 5 displays a biannual cycle peaking in spring and early autumn. The Oregon-California and Nevada modes (RPC1 and RPC4) have greatest variability between autumn and late spring and least variability in summer. This seasonality reflects the winter-dominated storminess climate pattern in California and Nevada, having more abundant clouds (and higher variations thereof) during the cool season (October-May) than during the warm season (June-September). In contrast, the two Pacific Northwest modes (RPC2 and RPC3) contain highest variability from summer to early autumn and lowest variability in winter and spring. The cloud cover over the Pacific Northwest during the cool season is high (Figure 2.2, upper panel), but prone to persisting for long periods—both RPC2 and RPC3 have minimum variability in December and January. The seasonality of the variance of the Great Basin mode (RPC5) has peaks in spring and autumn, resembling that of the northern Idaho-eastern Washington-eastern Oregon mode (RPC2) in which twice yearly cycle is presented.

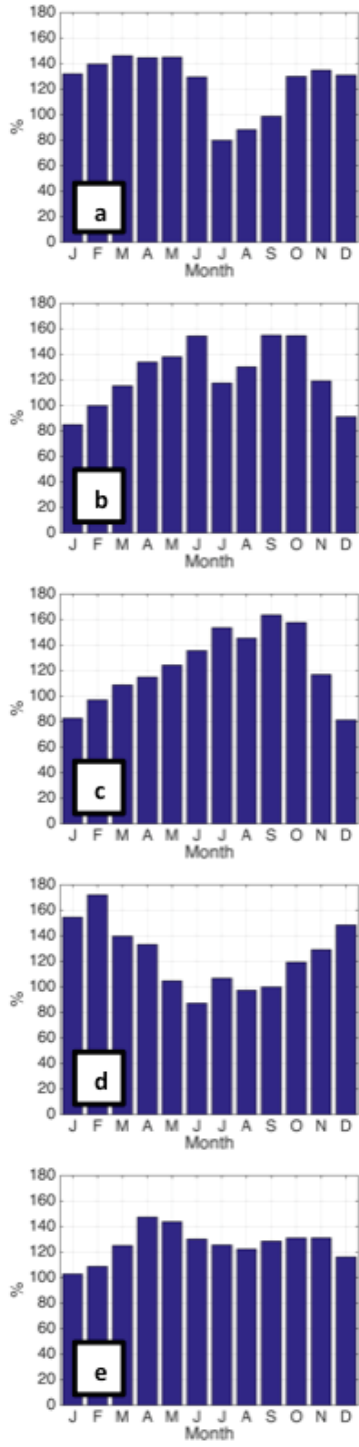


Figure 2.5. Standard deviations of (a) RPC1, (b) RPC2, (c) RPC3, (d) RPC4, and (e) RPC5 for each month in α_{cloud} percent unit, exemplifying the seasonal structures of each RPC mode.

2.4.4 Relations to larger scale circulation patterns

The contours in Figures 2.6a and 2.6b present the 500-hPa geopotential height (Z_{500}) composite anomaly fields from NARR historical reanalysis associated with the two REOF/RPC modes during the most positive α_{cloud} RPC amplitudes (cloudiest days) during December through August. The cloudy-day composites are characterized by negative Z_{500} anomalies with centers positioned west and/or north of the strongest REOF loadings, conducive to anomalous cyclonic flow and rising motion, as described below. Similarly, the contours in Figures 2.6c and 2.6d show the Z_{500} anomaly fields during the most negative RPC amplitude (clearest days). The clear-day composites are nearly the mirror image patterns of their positive RPC cloudy-day counterparts, with positive Z_{500} anomalies in the upstream or overlying regions, conducive to anomalous anti-cyclonic motion and descending motion.

The color shades in Figure 2.6 represent the 500-hPa pressure vertical velocity (ω_{500}) composite anomalies in association with the positive and negative α_{cloud} RPC subsets. A negative ω_{500} anomaly denotes greater than average upward motion, often associated with lowered surface pressure and often with precipitation; a positive ω_{500} anomaly denotes more downward motion, often associated with surface high pressure and often with fewer clouds. A consistent feature of the composites is the association of core positive REOF (greatest cloudiness) areas with strong negative ω_{500} anomaly over areas with strong negative Z_{500} anomaly and vice versa, in agreement with canonical quasi-geostrophic theory [e.g., Holton (2012)].

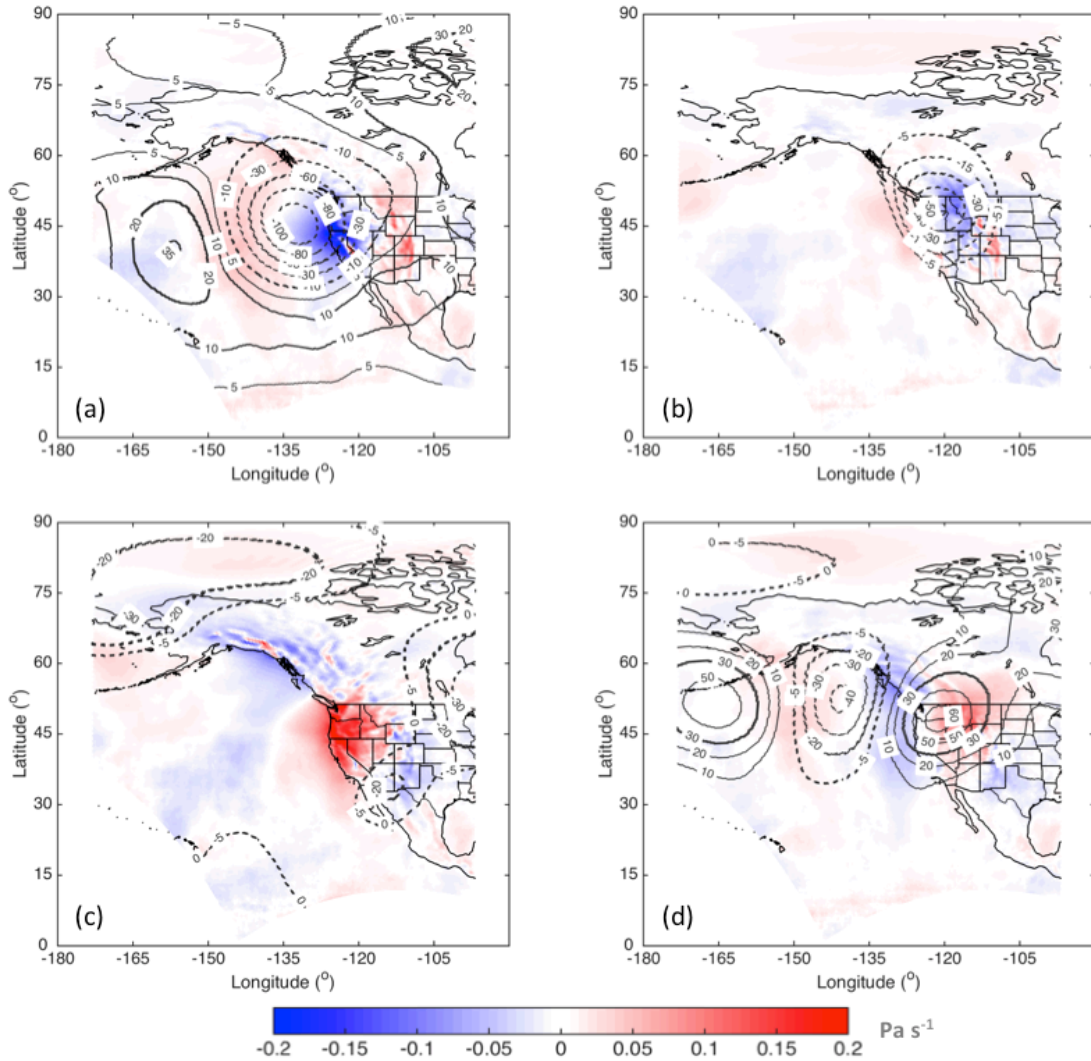


Figure 2.6. 500-hPa geopotential height (Z_{500}) anomaly (isolines) and pressure vertical velocity (ω_{500}) anomaly (shades) composited for days with the most positive (a and b) and most negative (c and d) anomalies for RPC1 (left) and RPC2 (right), representing cloudiest and clearest days during December-August of 1996-2014. The positive (negative) Z_{500} anomaly is contoured as solid (dashed) line.

2.4.5 Relations to lower frequency climate variability patterns

The associations of the REOF/RPCs with seasonal atmospheric circulation patterns are explored using conventional teleconnection indices and correlation patterns averaged over winter (DJF), spring (MAM) and summer (JJA).

Contingency tables are developed to understand how the high and low seasonal anomalies of the α_{cloud} RPCs associate with positive and negative expressions of the teleconnection patterns. Positive (negative) cloudiness RPC anomalies represent greater (lesser) cloudiness in the respective REOF core regions and are denoted +RPCs (–RPCs). Likewise, the positive/negative phase of the teleconnection indices are marked with +/- sign. From the contingency tables (not shown), the χ^2 statistics and the associated ϕ coefficients are summarized in Tables 2.4 and 2.5 to denote the statistical significance and the correlation of the associations between the teleconnection indices and the RPC modes.

Table 2.4. χ^2 values of the contingency tables relating the five RPC modes to selected teleconnection indices during winter (DJF), spring (MAM), and summer (JJA) of 1996-2014. The statistic is significant at 95% confidence level when $\chi^2 > 3.84$ (bold numbers).

Indices	Season	RPC1	RPC2	RPC3	RPC4	RPC5
AO	DJF	23.65	6.72	6.40	19.46	0.61
	MAM	0.49	1.98	0.03	0.67	0.22
	JJA	5.13	4.52	0.50	1.21	2.31
Niño 3.4	DJF	0.69	1.15	0.48	19.51	5.72
	MAM	0.00	0.79	0.15	5.07	0.03
	JJA	0.79	4.38	5.76	1.63	0.35
PNA	DJF	0.19	0.31	3.08	1.70	4.13
	MAM	1.51	0.41	0.05	2.87	0.29
	JJA	17.49	3.24	0.44	2.14	17.01

Table 2.5. ϕ coefficients associated with the χ^2 statistics, indicating the magnitude and the sign of the correlations between the RPCs and teleconnection indices during winter (DJF), spring (MAM), and summer (JJA) of 1996-2014.

Indices	Season	RPC1	RPC2	RPC3	RPC4	RPC5
AO	DJF	-0.24	0.12	0.12	-0.22	0.04
	MAM	-0.03	0.07	-0.01	-0.04	0.02
	JJA	-0.10	-0.10	-0.03	0.05	-0.07
Niño 3.4	DJF	0.04	-0.05	-0.03	0.21	-0.11
	MAM	0.00	0.04	-0.02	0.10	-0.01
	JJA	0.04	0.10	-0.11	0.06	0.03
PNA	DJF	-0.02	-0.03	0.08	0.06	-0.10
	MAM	0.06	-0.03	-0.01	0.08	0.02
	JJA	0.20	0.09	-0.03	0.07	0.19

RPC1, the interior California and Oregon pattern, has statistically significant relationships ($\chi^2 > 3.84$) with AO and PNA. RPC1 is negatively correlated with AO in DJF and JJA as indicated by the ϕ coefficient. Thus, +RPC1 cases tend to coincide with -AO, the equatorward and more distorted version of the high latitude westerlies that presumably increases storminess across the mid-latitudes of western North America (Thompson and Wallace, 2000, 2001). The opposite pattern, -RPC1 cases, is associated with +AO, the mode having confined high latitude westerly winds. The significant RPC1 relationship with PNA in JJA is rather unexpected because the PNA pattern is usually weak in summer, and because a high pressure ridge (indicative of fair weather) along the western North America often characterizes +PNA condition (Wallace and Gutzler, 1981). The RPC1-PNA contingency table shows a particularly high number of days when both RPC1 and PNA index are negative (Table 2.6). This unexpected RPC1-PNA relationship in JJA may also be a “false positive” attributed to the 95% confidence level test applied here.

Table 2.6. Contingency table showing the relationship between RPC1 and PNA in JJA

	+RPC1	-RPC1	Total
+PNA	123	78	201
-PNA	103	146	249
Total	226	224	450

RPC2, the interior northwestern U.S. pattern, associates with AO in DJF and JJA, where +RPC2 tends to concur with +AO in DJF and with -AO in JJA as indicated by the ϕ coefficient. Although mid-latitude storm activities in North Pacific are often associated with -AO when the westerlies are usually weaker (Thompson and Wallace, 2001), the relatively northern REOF2 region is in a location where the storm track may trail into the region even with +AO. Interestingly, RPC2 is positively correlated with Niño 3.4 in JJA, although El Niño Southern Oscillation (ENSO) signal in the western U.S. tends to be weak in boreal summer. The RPC2-Niño 3.4 contingency table shows a particularly high number of days when both RPC2 and Niño 3.4 index are positive (Table 2.7), demonstrating that contingency table analysis can report a statistically significant relationship even with only one distinctly high number of days.

Table 2.7. Contingency table showing the relationship between RPC2 and Niño3.4 in JJA

	+RPC2	-RPC2	Total
+Niño 3.4	138	98	236
-Niño 3.4	102	108	210
Total	240	206	446

Similar to RPC2, RPC3, the Cascade mountain range pattern, is positively correlated with AO in DJF, in keeping with the positive AO correlations with RPC2. However, the RPC3 relationship with AO is not statistically significant in JJA. +RPC3 is negatively correlated with Niño 3.4 in JJA. In view of the fact that its neighboring interior Northwest

pattern (REOF2/RPC2) is positively correlated with Niño 3.4 in JJA, this indicates a rather strong gradient of cloudiness may set in during summer ENSO events.

RPC4, the southwestern U.S. pattern, is significantly correlated with AO in DJF, where, similar to +RPC1, +RPC4 tends to coincide with –AO. Furthermore, +RPC4 events are associated with +Niño 3.4 in DJF and MAM, a signature of El Niño conditions and increased storminess in the southwestern U.S. (Cayan et al., 1999).

RPC5, the northern Nevada and Idaho pattern, associates with Niño 3.4 and PNA. RPC5 is negatively correlated with Niño 3.4 in DJF, evidently because El Niño forces storm tracks farther south resulting in variable influences on Great Basin precipitation (Smith et al., 2015). RPC5 is negatively correlated with PNA in DJF, indicating that strengthened high pressure ridging in winter reduces cloud cover over the northern Great Basin. However, RPC5 is positively correlated with PNA in JJA, reflecting Leathers et al. (1991) finding that PNA is negatively correlated with precipitation over much of the western U.S. during the cool season and a positively correlated during the warm season.

The correlation maps between the seasonal averages of the five leading α_{cloud} RPCs and those of Z_{500} anomaly are shown in Figure 2.7. Although they vary somewhat with season, the spatial structure of the correlation maps of RPCs 1 and 2 (upper two rows of Figure 2.7) is in good agreement with the daily composite maps in Figure 2.6. The rather detailed regional structure of the correlation maps explains why the association of western U.S. cloudiness with the AO, Niño 3.4, and PNA teleconnection patterns is perhaps more modest than might be expected. These correlations clearly represent regional circulations that may, at times, conflict with the larger scale circulations of the major teleconnection patterns, making for relatively weak associations.

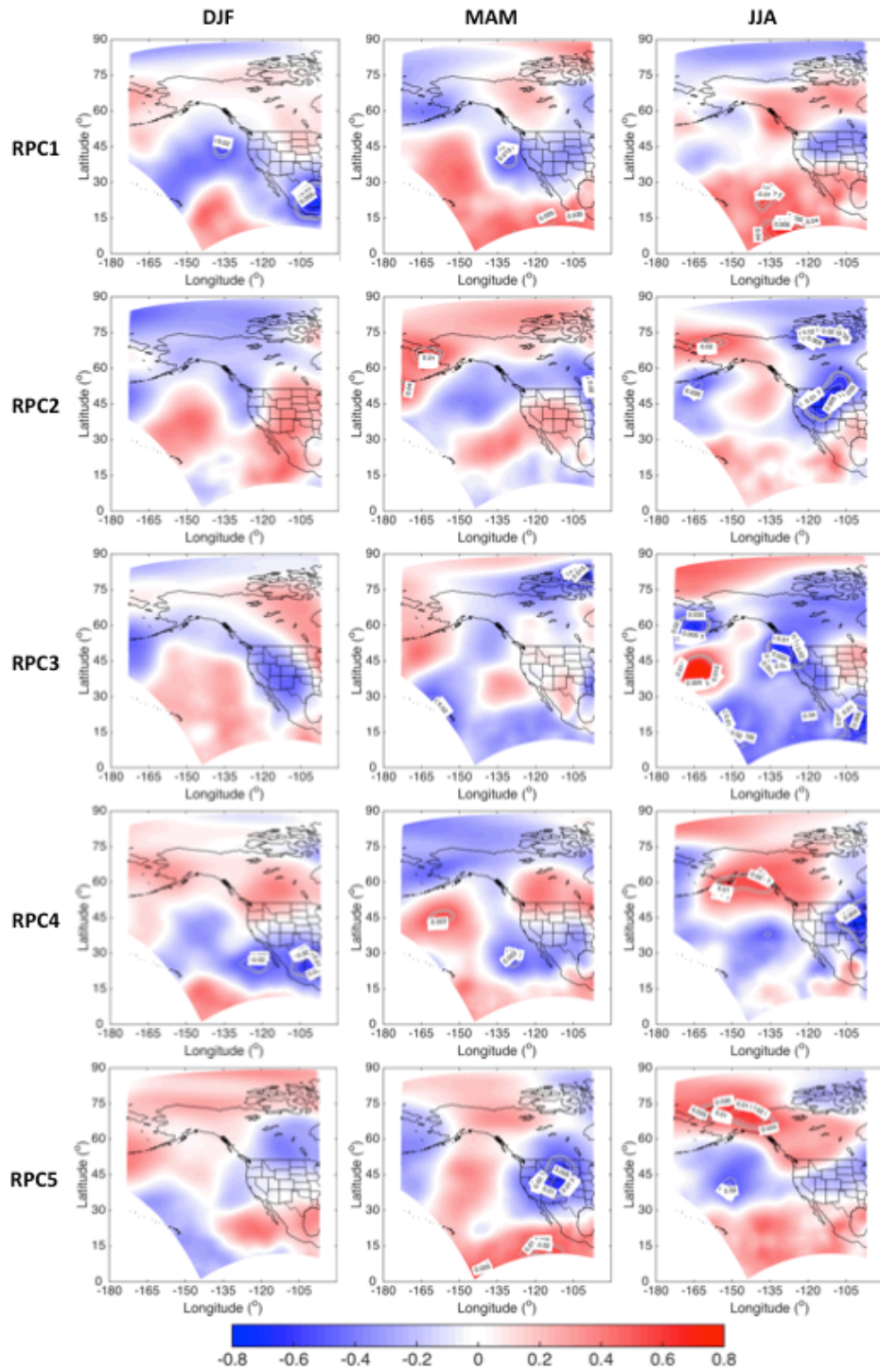


Figure 2.7. Correlation maps between the seasonal averages of the five leading α_{cloud} RPCs and those of Z_{500} anomaly for 1996-2014. The gray contours denote the areas where p -value < 0.05 .

2.5 Summary and conclusions

Aside from having substantial spatial and seasonal variation, cloudiness over the mountains of the western U.S. has significant anomalous variation over a broad range of scales. A 19-year (1996-2014) GOES cloud albedo (α_{cloud}) dataset, sampled to cover elevations ≥ 800 meters, exhibits anomalous fluctuations whose dominant patterns are organized over 100's of km regions. The high degree of spatial coherence is evidenced by the α_{cloud} REOF decomposition of the daily cloudiness variability in which the first five modes account for $\sim 67\%$ of the total variance. These α_{cloud} modes operate throughout the whole year, but they are modulated seasonally. For example, the leading mode represents the variability over northern California and Oregon and is accentuated between November and March, while the second mode represents that over the interior Pacific Northwest and is pronounced between March and July.

Anomalous cloudiness over high elevation regions has differing levels and primary seasons of activity. For example, in the southwest, mountain cloudiness variability is highest in spring, probably because of year-to-year climate variability and intermittent synoptic weather systems from the Pacific. This springtime variability amounts to $\sim 13\%$ (cloud albedo unit) on daily scale, equivalent to $\sim 95 \text{ W m}^{-2}$ difference in solar radiation (based on Tables 2.1 and 2.2). Even when seasonally averaged, the α_{cloud} standard deviation amounts to $\sim 3\%$, equivalent to $\sim 20 \text{ W m}^{-2}$ departure in incoming solar radiation. In contrast, in the northwest, the variability is lowest in winter and highest in summer, probably because it is persistently cloudy in winter while summertime cloudiness is more often interrupted by interludes of clear skies. In a relative sense, the amount of cloudiness variation compared to the mean cloudiness is uniformly higher in the southwest than in the northwest. Importantly, this

relative variation is quite large, with a magnitude of up to ~ 1.8 on daily scale and ~ 0.4 on seasonal scale, and is typically greatest during spring and summer when snowmelt is most active.

The seasonal variability of cloudiness over mountain regions in the western U.S. contrasts with that of eastern North Pacific and low lying coastal cloudiness, reflecting the different dynamics operating in these environments. This contrast is most evident in California, where the mean cloudiness and variability over higher elevation terrain is greatest in winter, while offshore and along the coastline they are greatest in summer.

As expected, daily variations in cloudiness are dictated by anomalous patterns of atmospheric circulation. Positive regional cloudiness anomalies are usually accompanied by anomalously low surface pressure systems, e.g., negative geopotential height anomalies and upward vertical velocity anomalies.

These circulation patterns are affected by regional and to some extent by Pacific basin-scale climate variability as represented by regional atmospheric circulation composites and by associations with AO, PNA and Niño 3.4 teleconnection patterns. These associations vary with regions and seasons. For instance, during the winter and spring the southwestern U.S. is greatly influenced by AO and Niño 3.4, while the interior Pacific Northwest is almost singularly influenced by AO. Somewhat surprisingly, northern California and Oregon are not strongly influenced by ENSO, probably because this region resides near the hinge point of the West Coast precipitation dipole (Dettinger et al., 1998).

Previous studies (e.g., Eastman and Warren, 2013; Norris et al., 2016) suggest there may be a slight decline in cloud cover globally and a poleward movement of mid-latitude storm tracks, but the 19-year GOES dataset is too short to form realistic estimates of trends.

Determination of long term changes over high elevations of the western U.S. must contend with considerable shorter period variability of cloudiness that is described here. Because of strong influences by large-scale weather and short period climate patterns, cloudiness varies over regional spatial scales, with characteristic patterns that cover large portions of the high elevation zones of the region.

Acknowledgment. ES was funded by the California Department of Water Resources Award 4600010378. DRC was funded by the California Energy Commission and the Southwest Climate Science Center sponsored by the U.S. Department of Interior and the U.S. Geological Survey. Many thanks to Sam Iacobellis for providing access to GOES imagery and for useful discussions and to Joel R. Norris and three anonymous reviewers for the thoughtful comments. This chapter, in full, is a reprint of the material as it appears in *Journal of Hydrometeorology* in 2017, with slight modifications. Sumargo, E., and D. R. Cayan, 2017: Variability of cloudiness over mountain terrain in the Western United States. *J. Hydrometeorol.*, **18**, 1227–1245, <https://doi.org/10.1175/JHM-D-16-0194.1>. ©American Meteorological Society. Used with permission. The dissertation author was the primary investigator and author.

APPENDIX 2A

GOES data availability

The structure of the missing data is illustrated in Figure 2.A1. Most of the missing data occur in early morning and late afternoon during times of low sun angle. There are more

missing data in winter months due to shorter day lengths. The right panel on Figure 2.A1 shows that >80% of the days have >15 half-hour daytime observations.

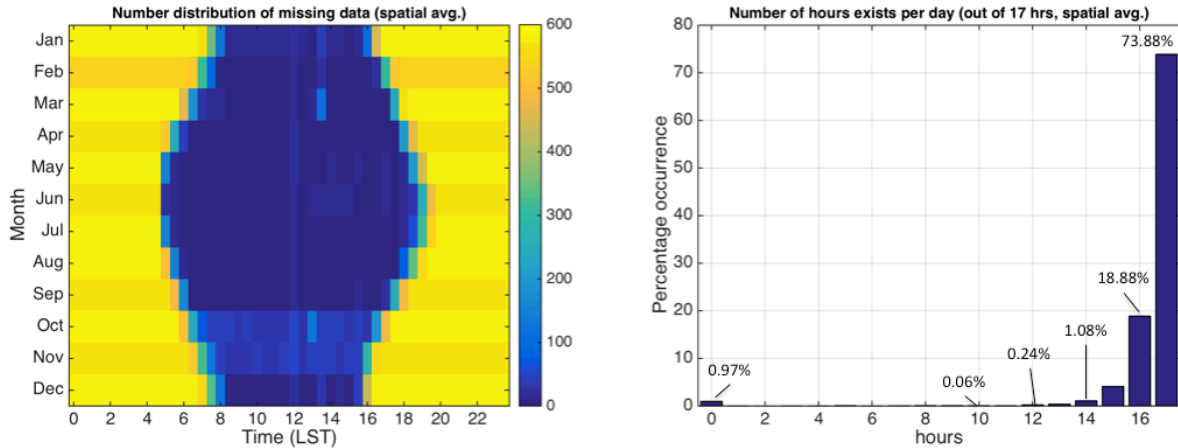


Figure 2.A1. Left: Number distribution of missing data for each month and half-hour of the day of 1996-2014, averaged over >300 high-elevation pixels across the westernmost U.S., illustrating which hours of the day have the least/most missing data in each month. Right: The percentages of hours between 0800 and 1600 PST exist per day during the same period and averaged over the same pixels, illustrating how many daytime hours exist on average.

Whether 10 out of 17 half-hours made a reasonable daily mean estimate was determined from an analysis summarized in Table 2.A1. We identified the days when there was no missing data between 0800 and 1600 LST and derived the daily averages. We then randomly removed [1, 2, 3...16] half-hours of the same days and re-derived the daily averages. In each instance, the correlation (R), root-mean-squared error (RMSE) and fractional mean absolute bias ($f|Bias| = |\alpha_{17-n} - \alpha_{17}|/\alpha_{17}$, for $1 \leq n \leq 16$) between the two sets (with vs. without missing data) were computed to determine the validity of the daily averages.

There is no set standard of how many half-hours or of how much error/bias can be tolerated. Together with the facts that >90% of the days had >15 half-hours available and that

the days with 7 missing data accounted for <0.1%, having an error (fractional bias) of ~1.91% (0.1) was a reasonable limit.

Table 2.A1. The correlation (R), root-mean-squared error (RMSE) and fractional mean absolute bias (f|Bias|) between daily average cloud albedo when no half-hour between 0800 and 1600 LST is missing and that when one or more (n) half-hours are missing, for $1 \leq n \leq 10$ only. The RMSEs are in percent cloud albedo unit. The statistics are averages over all days and sites as in Figure A1.

	n									
	1	2	3	4	5	6	7	8	9	10
R	0.999	0.998	0.997	0.996	0.994	0.993	0.991	0.990	0.988	0.986
RMSE	0.66	0.94	1.17	1.38	1.56	1.74	1.91	2.08	2.24	2.41
f Bias	0.03	0.05	0.06	0.07	0.08	0.09	0.10	0.11	0.12	0.13

APPENDIX 2B

Clear-sky albedo time window

Figure 2.B1 shows how different time windows used to determine the clear-sky albedo evolve throughout the water year 2006, in comparison to snow water equivalent (SWE) at nearby snow sensors in California and Idaho mountain settings. Each of the clear-sky albedos generally captures the snow and non-snow season, but the one with the shortest time window (7 days) is hypersensitive to short-term fluctuations. In contrast, the one with the longest time window (28 days) is hyposensitive to such fluctuations. The 15-day (± 7 days) time window has intermediate properties that capture major changes while being immune to short period changes.

There were a few isolated cases when the 15-day time window did not capture the evolving snow surface cover during the early snow season. For example, the period when snowfall and accumulation occurred rapidly between 29 November 2005 and 1 December 2005 was misclassified as no snow accumulation (Figure 2.1). Shortening the time window

(e.g., to 7-day period) resolved this problem, but resulted in other days misclassified as cloud-free, e.g., 2 December 2005, 7 December 2005 and 15 December 2005. On the other hand, expanding the time window would result in more days misclassified as no snow accumulation, e.g., in 1-4 December 2005 and 31 December 2005. Thus, we determined that 15-day window was optimal.

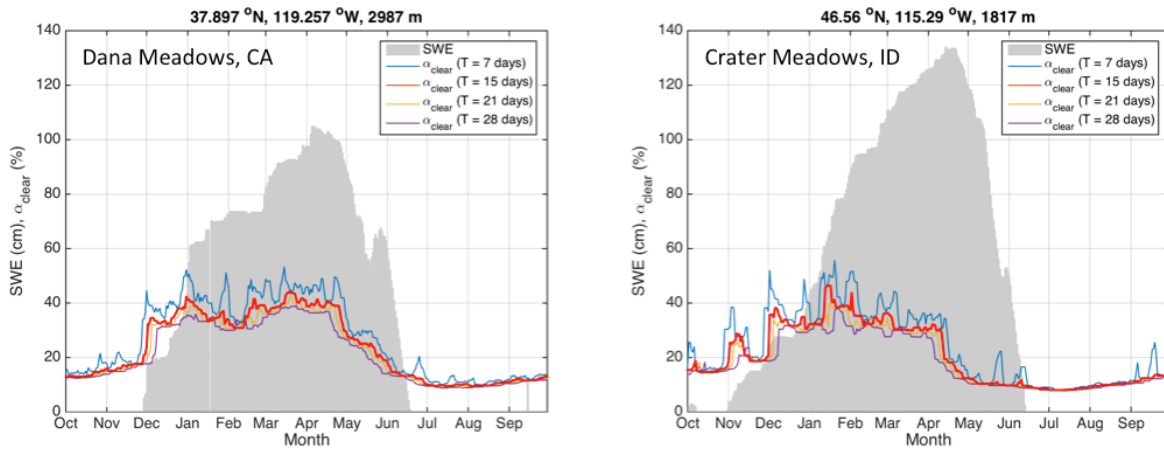


Figure 2.B1. Daily time-series of water year 2006 SWE (gray shading) and of α_{clear} derived using four different time windows (color plots) at Dana Meadows in the Yosemite National Park, California, (left) and Crater Meadows in Idaho (right). The thick red line denotes the time window used in the study.

APPENDIX 2C

Determining the seasonal cycle

Harmonic fitting, Butterworth filter and Chebyshev Type I filter were evaluated alongside the original 29-day (± 14 days) centered moving average used in this study. Figure 2.C1 shows the de-seasonalized daily cloud albedo time-series at four different pixels and two selected filters (1st order Chebyshev Type I filter, 29-day centered moving average), averaged over all years. The more sophisticated and computationally more intensive method yielded a somewhat different representation of the annual cycle, but without appreciable

improvement. The power spectra of the de-seasonalized time-series displayed similar power dissipations at different spectral periods, most notably at ~ 365 -day period (not shown).

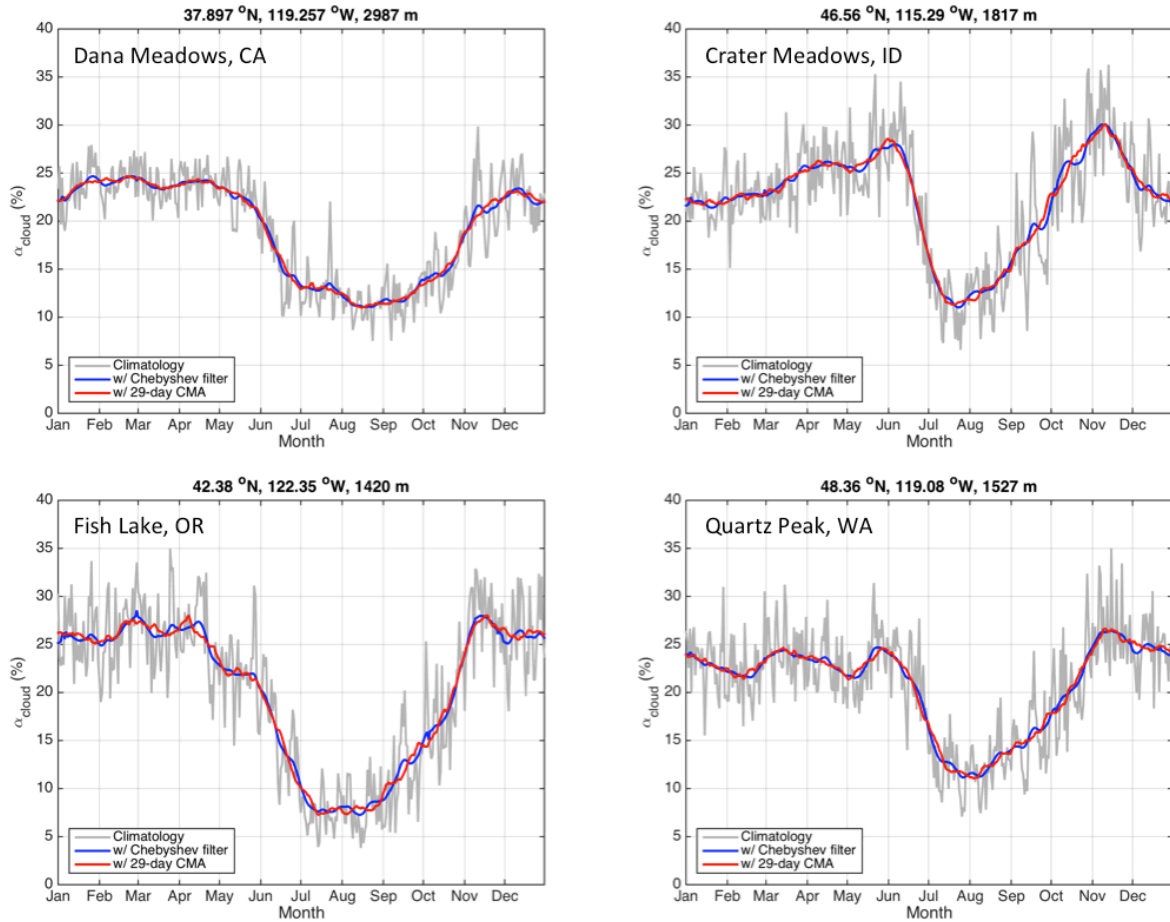


Figure 2.C1. Daily climatology (1996-2014) of α_{cloud} (gray) and its low-pass filtered versions using Chebyshev Type I filter (blue) and original 29-day (± 14 days) centered moving average (CMA) (red) at four different locations.

The same conclusion was derived when different filters (i.e., harmonic fitting and Butterworth filter) and different orders (i.e., 2nd, 3rd, ... order Chebyshev, 1, 2, 3, ... -point Butterworth) were used. Furthermore, the two other filters and the higher order Chebyshev filters tended to underestimate the annual cycle as they produce dampened amplitudes, which resulted in large positive biases in winter and large negative biases in summer.

References

- Aguado, E., 1985: Radiation balances of melting snow covers at an open site in the central Sierra Nevada, California. *Water Resour. Res.*, **21**(11), 1649-1654.
- Bales, R. C., N. P. Molotch, T. H. Painter, M. D. Dettinger, R. Rice, and J. Dozier, 2006: Mountain hydrology of the western United States. *Water Resour. Res.*, **42**(8).
- Cano, D., J. M. Monget, M. Albuissou, H. Guillard, N. Regas, and L. Wald, 1986: A method for the determination of the global solar radiation from meteorological satellite data. *Solar Energy*, **37**, 31-39.
- Cayan, D. R., K. T. Redmond, and L. G. Riddle, 1999: ENSO and Hydrologic Extremes in the Western United States*. *J. Climate*, **12**, 2881–2893. doi: [http://dx.doi.org/10.1175/1520-0442\(1999\)012<2881:EAHEIT>2.0.CO;2](http://dx.doi.org/10.1175/1520-0442(1999)012<2881:EAHEIT>2.0.CO;2)
- Clemesha, R. E. S., A. Gershunov, S. F. Iacobellis, A. P. Williams, and D. R. Cayan, 2016: The northward march of summer low cloudiness along the California coast. *Geophys. Res. Lett.*, **43**, 1287-1295. doi:10.1002/2015gl067081.
- Cline, D. W., 1997: Snow surface energy exchanges and snowmelt at a continental, midlatitude Alpine site. *Water Resour. Res.*, **33**(4), 689-701.
- Dai, A., T. R. Karl, B. Sun, and K. E. Trenberth, 2006: Recent trends in cloudiness over the United States: A tale of monitoring inadequacies. *Bull. Amer. Meteor. Soc.*, **87**, 597–606.
- Davis, R. E., 1976: Predictability of Sea Surface Temperature and Sea Level Pressure Anomalies over the North Pacific Ocean. *J. Phys. Oceanogr.*, **6**, 249–266. doi: [http://dx.doi.org/10.1175/1520-0485\(1976\)006<0249:POSSTA>2.0.CO;2](http://dx.doi.org/10.1175/1520-0485(1976)006<0249:POSSTA>2.0.CO;2)
- Davenport, E. C., and N. A. El-Sanhurry, 1991: Phi/phimax: review and synthesis. *Educational and Psychological Meas.*, **51**(4), 821-828.
- Dettinger, M., 2011: Climate change, atmospheric rivers, and floods in California—A multimodel analysis of storm frequency and magnitude changes. *J. Am. Water Resour. Assoc.*, **47**(3), 514–523, doi:10.1111/j.1752-1688.2011.00546.x.
- Dettinger, M. D., D. R. Cayan, H. F. Diaz, and D. M. Meko, 1998: North-south precipitation patterns in western North America on interannual-to-decadal time scales. *J. Climate*, **11**(12), 3095-3111.
- Done, J., C. A. Davis, and M. Weisman, 2004: The next generation of NWP: Explicit forecasts of convection using the Weather Research and Forecasting (WRF) model. *Atmos. Sci. Lett.*, **5**(6), 110-117.
- Eastman, R., and S. G. Warren, 2013: A 39-Yr Survey of Cloud Changes from Land Stations Worldwide 1971–2009: Long-Term Trends, Relation to Aerosols, and Expansion of the Tropical Belt. *J. Climate*, **26**, 1286-1303.

- Franzke, C., K. Fraedrich, and F. Lunkeit, 2001: Teleconnections and low-frequency variability in idealized experiments with two storm tracks. *Quart. J. Roy. Meteor. Soc.*, **127**, 1321–1339.
- Gautier, C., G. Diak, and S. Masse, 1980: A Simple Physical Model to Estimate Incident Solar Radiation at the Surface from GOES Satellite Data. *J. Appl. Meteor.*, **19**, 1005–1012. doi: [http://dx.doi.org/10.1175/1520-0450\(1980\)019<1005:ASPMTE>2.0.CO;2](http://dx.doi.org/10.1175/1520-0450(1980)019<1005:ASPMTE>2.0.CO;2).
- Gimeno García, S., T. Trautmann, and V. Venema, 2012: Reduction of radiation biases by incorporating the missing cloud variability via downscaling techniques: a study using the 3-D MoCaRT model. *Atmos. Meas. Tech. Disc.*, **5**(1), 1543-1573.
- Grubišić, V., and B. J. Billings, 2008: Climatology of the Sierra Nevada Mountain-Wave Events. *Mon. Weather Rev.*, **136**(2), 757–768. doi:10.1175/2007MWR1902.1.
- Hannachi, A., 2004: A primer for EOF analysis of climate data. University of Reading, 33 pp.
- Held, I. M., and B. J. Soden, 2006: Robust Responses of the Hydrological Cycle to Global Warming. *J. Climate*, **19**, 5686–5699. doi: <http://dx.doi.org/10.1175/JCLI3990.1>
- Hinkelman, L. M., K. E. Lapo, N. C. Cristea, and J. D. Lundquist, 2015: Using CERES SYN Surface Irradiance Data as Forcing for Snowmelt Simulation in Complex Terrain. *J. Hydrometeorol.*, **16**, 2133-2152. doi:10.1175/JHM-D-14-0179.1.
- Holton, J., 2012: *An introduction to dynamic meteorology*. 5th edition, Academic press, 552 pp.
- Howell, D. C., 2011: Chi-square test: analysis of contingency tables. *International Encyclopedia of Statistical Science*. Springer Berlin Heidelberg, 250-252 pp.
- Iacobellis, S. F., and D. R. Cayan, 2013: The variability of California summertime marine stratus: Impacts on surface air temperatures. *J. Geophys. Res.: Atmospheres*, **118**(16), 9105-9122.
- Ineichen, P., and R. Perez, 1999: Derivation of cloud index from geostationary satellites and application to the production of solar irradiance and daylight illuminance data. *Theor. Appl. Climatol.*, **64**, 119–130.
- Kaiser, H. F., 1958: The varimax criterion for analytic rotation in factor analysis. *Psychometrika*, **23**, 187–200.
- Kelly, D. L., J. T. Schaefer, and C. A. Doswell III, 1985: Climatology of nontornadic severe thunderstorm events in the United States. *Mon. Wea. Rev.*, **113**(11), 1997-2014.
- Khan, S. I., and Coauthors, 2011: Satellite remote sensing and hydrologic modeling for flood inundation mapping in Lake Victoria Basin: Implications for hydrologic prediction in ungauged basins. *IEEE Trans. Geosci. Remote Sens.*, **49**(1), 85–95, doi:10.1109/TGRS.2010.2057513.

- Kleissl, J., 2013: *Solar energy forecasting and resource assessment*, Oxford: Academic Press.
- Lapo, K. E., L. M. Hinkelman, M. S. Raleigh, and J. D. Lundquist, 2015: Impact of errors in the downwelling irradiances on simulations of snow water equivalent, snow surface temperature, and the snow energy balance. *Water Resour. Res.*, **51**, 1649–1670. doi:10.1002/2014WR016259.
- Leathers, D. J., B. Yarnal, and M. A. Palecki, 1991: The Pacific/North American teleconnection pattern and United States climate. Part I: Regional temperature and precipitation associations. *J. Climate*, **4**(5), 517-528.
- Leavesley, G. H., R. W. Lichty, B. M. Troutman, and L. G. Saindon, 1983: Precipitation-runoff modeling system: User's manual, *Water-Resources Investigation Report*, 83-4238 pp., U.S. Geol. Surv.
- Lorenz, E. N., 1956: Empirical orthogonal functions and statistical weather prediction. Statistical Forecasting Project Rep. 1, MIT Department of Meteorology, 49 pp.
- Marks, D., and J. Dozier, 1992: Climate and energy exchange at the snow surface in the alpine region of the Sierra Nevada: 2. Snow cover energy balance. *Water Resour. Res.*, **28**(11), 3043-3054.
- Markstrom, S. L., R. S. Regan, L. E. Hay, R. J. Viger, R. M. T. Webb, R. A. Payn, and J. H. LaFontaine, 2015: PRMS-IV, the precipitation-runoff modeling system, version 4. *U.S. Geological Survey Techniques and Methods*, book 6, chap. B7, 158 p., <http://dx.doi.org/10.3133/tm6B7>.
- Mesinger, F., G. DiMego, E. Kalnay, K. Mitchell, P. C. Shafran, W. Ebisuzaki, D. Jović, J. Woollen, E. Rogers, E. H. Berbery, M. B. Ek, Y. Fan, R. Grumbine, W. Higgins, H. Li, Y. Lin, G. Manikin, D. Parrish, and W. Shi, 2006: North American regional reanalysis. *Bull. Am. Meteorol. Soc.*, **87**, 343–360.
- Mizukami, N., M. P. Clark, A. G. Slater, L. D. Brekke, M. M. Elsner, J. R. Arnold, and S. Gangopadhyay, 2014: Hydrologic Implications of Different Large-Scale Meteorological Model Forcing Datasets in Mountainous Regions. *J. Hydrometeorol.*, **15**(1), 474–488, doi:10.1175/JHM-D-13-036.1.
- Molotch, N. P., T. H. Painter, R. C. Bales, and J. Dozier, 2004: Incorporating remotely sensed snow albedo into spatially distributed snowmelt modeling. *Geophys. Res. Lett.*, **31**, L03501, doi: 10.1029/2003GL019063.
- Monahan, A. H., J. C. Fyfe, M. H. Ambaum, D. B. Stephenson, and G. R. North, 2009: Empirical orthogonal functions: The medium is the message. *J. Climate*, **22**(24), 6501-6514.
- Mote, P. W., 2006: Climate-Driven Variability and Trends in Mountain Snowpack in Western North America*. *J. Climate*, **19**(23), 6209-6220.

- Norris, J. R., R. J. Allen, A. T. Evan, M. D. Zelinka, C. W. O'Dell, and S. A. Klein, 2016: Evidence for Climate Change in the Satellite Cloud Record. *Nature*. doi: 10.1038/nature18273.
- O’Gorman, P. A., and T. Schneider, 2008: The Hydrological Cycle over a Wide Range of Climates Simulated with an Idealized GCM. *J. Climate*, **21**, 3815–3832. doi: <http://dx.doi.org/10.1175/2007JCLI2065.1>
- Paech, S. J., J. R. Mecikalski, D. M. Sumner, C. S. Pathak, Q. Wu, S. Islam, and T. Sangoyomi, 2009: A calibrated, highresolution GOES satellite solar insolation product for a climatology of Florida evapotranspiration. *J. Amer. Water Resour. Assoc.*, **45**(6), 1328–1342.
- Paulescu, M., E. Paulescu, P. Gravila, V. Badescu, 2012: *Weather Modeling and Forecasting of PV Systems Operation*, 2013th edn. London: Springer-Verlag.
- Pearson, K., 1895: Notes on regression and inheritance in the case of two parents. *Proc. R. Soc. Lond.*, **58**, 240-242.
- Pearson, K., 1904: On the theory of contingency and its relation to association and normal correlation. *Foreword to Drapers Company research memoirs: Biometric series I*.
- Perez, R., P. Ineichen, K. Moore, M. Kmiecik, C. Chain, R. George, and F. Vignola, 2002: A new operational model for satellite-derived irradiances: description and validation. *Solar Energy*, **73**, 307-317.
- Perez, R., S. Kivalov, A. Zelenka, J. Schlemmer, and K. Hemker Jr., 2010: Improving the performance of satellite-to-irradiance models using the satellite’s infrared sensors. In: *Proc. of American Solar Energy Society’s Annual Conference*, Phoenix, AZ.
- Pierce, D. W., and D. R. Cayan, 2013: The Uneven Response of Different Snow Measures to Human-Induced Climate Warming. *J. Climate*, **26**, 4148–4167. doi: <http://dx.doi.org/10.1175/JCLI-D-12-00534.1>
- Pierce, D. W., and Coauthors, 2008: Attribution of declining western US snowpack to human effects. *J. Climate*, **21**(23), 6425-6444.
- Raleigh, M. S., K. Rittger, and J. D. Lundquist, 2011: What lies beneath? Comparing MODIS fractional snow covered area against ground-based observations under forest canopies and in the meadows of the Sierra Nevada. *Proc. Western Snow Conf.*, **79**, 3-14.
- Ramanathan, V., R. D. Cess, E. F., Harrison, P. Minnis, B. R. Barkstrom, E. Ahmad, E., and D. L. Hartmann, 1989: Cloud-radiative forcing and climate: Results from the Earth Radiation Budget Experiment. *Science*, **243**(4887), 57-63.
- Rauber, R. M., 1992: Microphysical Structure and Evolution of a Central Sierra Nevada Orographic Cloud System. *J. Appl. Meteor.*, **31**, 3–24, doi: [http://dx.doi.org/10.1175/1520-0450\(1992\)031<0003:MSAEOA>2.0.CO;2](http://dx.doi.org/10.1175/1520-0450(1992)031<0003:MSAEOA>2.0.CO;2).
- Richman, M. B., 1986: Rotation of principal components. *J. Climate*, **6**(3), 293-335.

- Ringer, M. A., and K. P. Shine, 1997: Sensitivity of the Earth's radiation budget to interannual variations in cloud amount. *Climate Dyn.*, **13**, 213–222.
- Rittger, K., A. Kahl, and J. Dozier, 2011: Topographic distribution of snow water equivalent in the Sierra Nevada, *Proc. Western Snow Conf.*, **79**, 37-46.
- Rittger, K., T. H. Painter, and J. Dozier, 2013: Assessment of methods for mapping snow cover from MODIS. *Adv. Water Resour.*, **51**, 367-380.
- Rossow, W. B., C. Delo, and B. Cairns, 2002: Implications of the observed mesoscale variations of clouds for the Earth's radiation budget. *J. Climate*, **15**, 557 – 585.
- Serreze, M. C., M. P. Clark, R. L. Armstrong, D. A. McGinnis, and R. S. Pulwarty, 1999: Characteristics of the western United States snowpack from snowpack telemetry (SNOTEL) data. *Water Resour. Res.*, **35**(7), 2145-2160.
- Seze, G., and W. B. Rossow, 1991: Time-cumulated visible and infrared radiance histograms used as descriptors of surface and cloud variations. *Int. J. Remote Sens.*, **12**, 877–920.
- Simpson, J. J., M. D. Dettinger, F. Gehrke, T. J. McIntire, and G. L. Hufford, 2004: Hydrologic scales, cloud variability, remote sensing, and models: Implications for forecasting snowmelt and streamflow. *Wea. Forecasting*, **19**(2), 251-276.
- Smith, G. L., D. Rutan, and T. D. Bess, 1992: Atlas of albedo and absorbed solar radiation derived from Nimbus-7 Earth Radiation Budget data set — November 1978 to October 1985. NASA Ref Publ 1231.
- Smith, K., C. Strong, and S. Y. Wang, 2015: Connectivity between historical Great Basin precipitation and Pacific Ocean variability: A CMIP5 model evaluation. *J. Climate*, **28**(15), 6096-6112.
- Thompson, D. W. J., and J. M. Wallace, 2000: Annular modes in the extratropical circulation. Part I: Month-to-month variability. *J. Climate*, **13**, 1000–1016.
- Thompson, D. W., and J. M. Wallace, 2001: Regional climate impacts of the Northern Hemisphere annular mode. *Science*, **293**(5527), 85-89.
- U.S. Army Corps of Engineers, 1956: *Snow hydrology: Summary report of the snow investigations*. North Pacific Division, U.S. Army Corps of Engineers, 437 pp.
- Wallace, J. M., and D. S. Gutzler, 1981: Teleconnections in the geopotential height during the northern hemisphere winter. *Mon. Wea. Rev.*, **109**(4), 784-812.
- Warren, S. G., R. M. Eastman, and C. J. Hahn, 2007: A Survey of Changes in Cloud Cover and Cloud Types over Land from Surface Observations, 1971 – 1996. *J. Climate*, **20**, 717-738.
- Welch, R. M., K. S. Kuo, B. A. Wielicki, S. K. Sengupta, and L. Parker, 1988: Marine stratocumulus cloud fields off the coast of southern California observed using LANDSAT imagery. Part I: Structural characteristics. *J. Appl. Meteor.*, **27**, 363–378.

Whiteman, C. D., 2000: *Mountain Meteorology: Fundamentals and Applications*. Oxford University Press, 376 pp.

Wilks, D. S., 1995: *Statistical Methods in Atmospheric Sciences: An Introduction*. Academic Press, 467 pp.

Yin, J. H., 2005: A consistent poleward shift of the storm tracks in simulations of 21st century climate. *Geophys. Res. Lett.*, **32**, L18701, doi:10.1029/2005GL023684.

Zelenka, A., R. Perez, R. Seals, and D. Renne, 1999: Effective accuracy of satellite-derived hourly irradiances. *Theor. Appl. Climatol.*, **62**, 199-207.

Chapter 3

The Influence of Cloudiness on Hydrologic Fluctuations in the Mountains of the Western United States

This study investigates snowmelt and streamflow responses to cloudiness variability across the mountainous parts of the western United States. Twenty years (1996-2015) of Geostationary Operational Environmental Satellite-derived cloud cover indices (CC) with 4-km spatial and daily temporal resolutions are used as a proxy for cloudiness. The primary driver of non-seasonal fluctuations in daily mean solar insolation is the fluctuating cloudiness. We find that CC fluctuations are related linearly to snowmelt and snow-fed streamflow fluctuations, to some extent (correlations < 0.5). Multivariate linear regression models of daily snowmelt (MELT) and streamflow (ΔQ) variations are constructed for each month from February to July, when snowmelt is most active. Predictors include CC from five antecedent days up to the concurrent day. The CC-MELT and CC- ΔQ associations vary with time and location. The results show the dominance of negative correlations between CC and MELT, exemplifying the cloud-shading (or clear-sky) effect on snowmelt. The magnitude of CC-MELT association (R^2) amounts to 5%-56%, typically peaking in May. These associations fade earlier in summer during dry years than wet years, indicating the differing responses of higher vs. lower snowpack. The CC- ΔQ association displays less consistent pattern, with R^2 amounting to 2%-47%. Nevertheless, MELT and ΔQ fluctuations exhibit spatially extensive patterns of correlations with daily cloudiness anomalies, indicating the effects of cloudiness often operate over regional spatial scales.

3.1 Introduction

Snowmelt from mountain snowpack is an essential source of water supply in many regions on the globe (Barnett et al., 2005). Notably, in the western United States (U.S.), seasonal streamflow originating from spring-summer mountain snowmelt supplies much of the water needs (Serreze et al., 1999; Stewart et al., 2004; Li et al., 2017). For this reason, seasonal snowmelt is a critical process that draws considerable research attentions.

Numerous studies have investigated the effects of precipitation and temperature on surface hydrologic variability (e.g., Karl & Riebsame, 1989; Mote, 2006; Stoelinga et al., 2009; McCabe & Wolock, 2011; Nowak et al., 2012; Luce et al., 2014; Woodhouse et al., 2016; Sproles et al., 2017). Incoming solar radiation at the surface, hereby called the shortwave flux (SWF), is another significant contributor to hydrologic variability. However, the effect of SWF variations on hydrologic variability remains inadequately studied, although SWF is a dominant snowmelt energy balance component in alpine catchments (Marks & Dozier, 1992; Cline, 1997; Bales et al., 2006; Comola et al., 2015).

The difficulties in characterizing the effect of SWF variations are due mainly to irregular fluctuations of surface radiation, which depend on the highly variable cloud cover (Simpson et al., 2004). Varying spring-summer cloudiness over the mountains in WUS produces SWF fluctuations that amount to $\sim 90\text{-}140 \text{ W m}^{-2}$ on an hourly scale, $\sim 60\text{-}130 \text{ W m}^{-2}$ on a daily scale, and $\sim 10\text{-}20 \text{ W m}^{-2}$ on a seasonal scale [following Sumargo & Cayan (2017)]. Sustaining measurements of these fluctuations over several years is a challenge—difficult access to mountain environments hinders the installation and maintenance of in situ radiation measurements, especially in wintertime (Henn et al., 2015; Lapo et al., 2015a). Consequently, surface radiometer observations are sparse in mountain environments

(Hinkelman et al., 2015; Lapo et al., 2015b), resulting in poor representations of cloudiness and surface irradiance (Gautier et al., 1980; Bales et al. 2006), and tend to have poor data quality requiring careful quality control (Slater, 2015). In addition to complex terrain and vegetation (Lundquist & Flint, 2006; Andreadis et al., 2009; Raleigh et al., 2013; Lundquist et al., 2013; Garvelmann et al., 2014; Dickerson-Lange et al., 2017; Comola et al., 2015; Henn et al., 2015), the lack of accurate cloudiness and radiation data impairs the understanding and modeling efforts of hydrologic variability in mountain settings (Rittger et al., 2016; Lapo et al., 2015a).

Therefore, an accurate representation of cloudiness variability is necessary to characterize surface radiation and hydrologic variabilities. Cloudiness is also correlated with fluctuations of precipitation and surface air temperature (Appendix 3.A), whose effects on surface hydrologic variability are well documented (Lundquist et al., 2013; Garvelmann et al., 2015; Mutzner et al., 2015; Shukla et al., 2015; Woodhouse et al., 2016). In contrast, the relationship between cloudiness and surface hydrology has not been thoroughly explored, particularly in mountain environments. Thus, the relationship between cloudiness variations and surface hydrologic variability deserves further investigation. This topic should motivate future uses of satellite-derived cloud cover to benefit SWE and streamflow predictions.

Past studies have demonstrated the applicability of geostationary satellite observations in characterizing cloudiness and solar energy-related variability (e.g., Gautier et al., 1980; Cano et al., 1986; Ineichen et al., 1999; Perez et al., 2002; Simpson et al., 2004). Because most mountainous watersheds in WUS are sparsely monitored by in situ stations, most of which do not include radiometer instruments (Raleigh et al., 2016), remote sensing is

arguably the most reliable option for locations >20 km away from any ground stations (Zelenka et al., 1999).

In this work, we employ high spatial and temporal resolution observations from a geostationary satellite, along with surface observations and a simple physical snow model, to characterize the variability of cloudiness and investigate its relationships with snowmelt and streamflow. Specifically, we address the following questions:

1. How do springtime snowmelt and streamflow respond to local intraseasonal cloudiness variability, and how strong are these responses?
2. How do the responses vary across different regions and across the years?
3. How do they compare to regional-scale cloudiness variability?

Our geographical focus is the western U.S. (WUS). Unless otherwise noted, the analyses are aggregated into three regions: 1) northwestern U.S. (NW; >42 °N) and 2) southwestern U.S. (SW; <42 °N) as in Figure 3.1, and 3) WUS, the union of NW and SW.

The relevance of this study to WUS is heightened by the vulnerability of WUS to climate change, owing to its strong topographic gradients and the sensitivity of mountain snowpack to climate fluctuations (Barnett et al., 2008; IPCC, 2013). Moreover, hydrologic applications commonly rely on historical statistics, which are increasingly obsolete with climate change (Lundquist et al., 2009; Rice et al., 2011). These attributes can adversely impact the ecology (Diaz & Eischeid, 2007; Null et al., 2013) and hydrologic systems (Hoerling et al., 2013; Mann & Gleick, 2015; Musselman et al., 2017). Earlier snow-fed streamflow (Dettinger & Cayan, 1995; Cayan et al., 2001; Stewart et al., 2005; Regonda et al., 2005) and extensive declines in spring snowpack (Mote, 2003, 2006; Mote et al., 2005,

2008; Pierce et al., 2008; Kapnick & Hall, 2012; Sproles et al., 2017) and snow cover extent (Groisman & Easterling, 1994) are observed throughout.

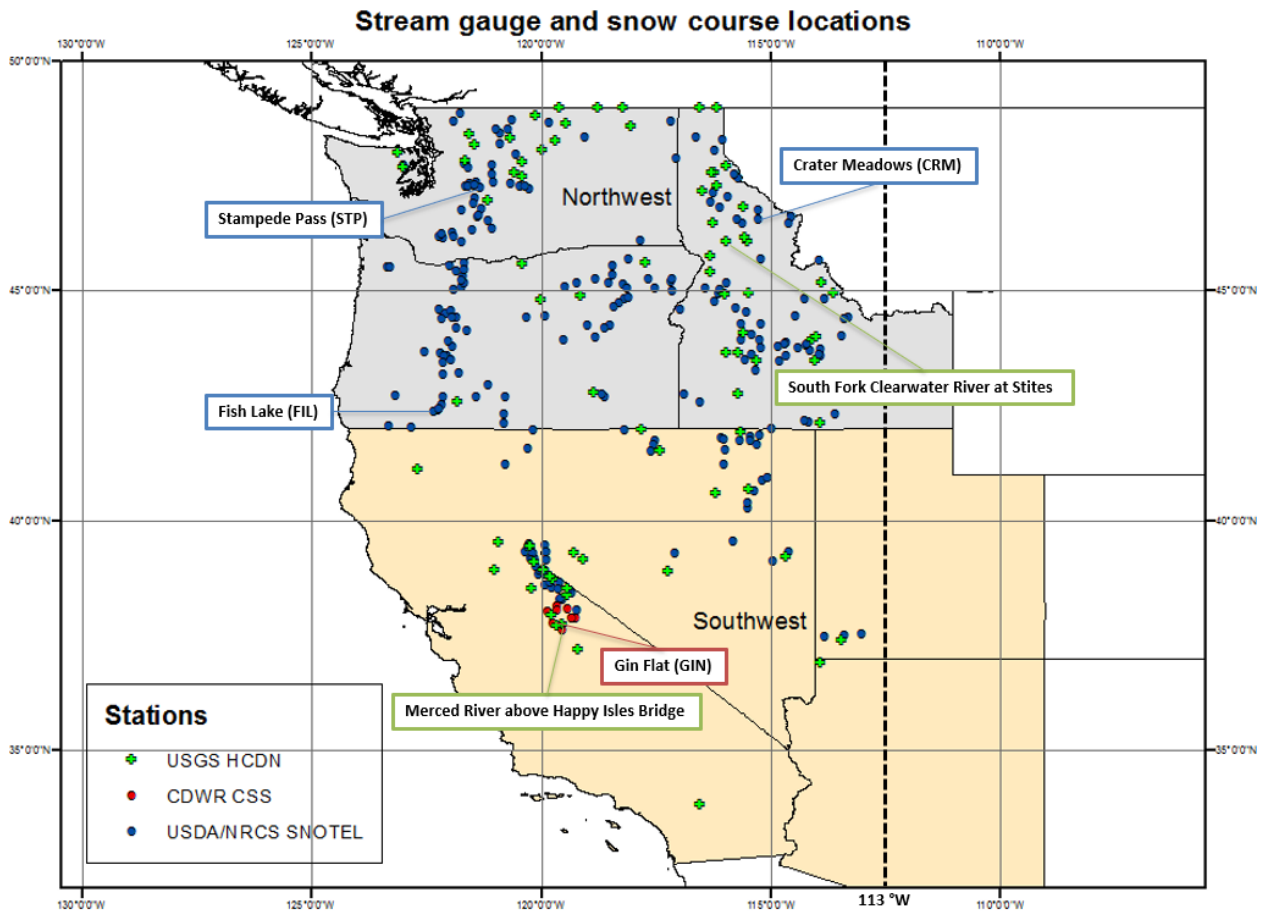


Figure 3.1. USGS HCDN stream gauges (green), CDWR CSS (CDEC) snow sensors (red) and USDA/NRCS SNOTEL (blue) snow pillows employed in this study. The background colors signify the Northwest (gray) and the Southwest (beige) climate regions adapted from Karl and Koss (1984) and verified using principal component analysis (Section 3.3.4). The 113 °W line denotes the eastern limit of our research domain. The text boxes denote some sites examined in this paper.

This sensitivity was exemplified in the recent exceptional drought in California (2012-2015), marked by disproportionately low spring-early summer snowpack associated with anomalous low precipitation (Mao et al., 2015; Williams et al., 2015), and in the “snowpack drought” in 2014/2015 in Oregon and Washington, marked by near-normal

precipitation and anomalous high temperature resulting in lower snow-precipitation ratio (Fosu et al., 2016; Mote et al., 2016; Sproles et al., 2017). In contrast, 2016/2017 featured numerous Atmospheric River events (Ralph et al., 2017) and high snowpack (California Department of Water Resources, 2017; Lettenmaier, 2017), highlighting an exceptionally wet year in California. In view of these issues, WUS is a suitable natural laboratory for our research.

3.2 Data, methods and tools

3.2.1 Observational datasets and processing

3.2.1.1 Cloud cover index

The cloud cover index (CC) used in this study is derived from the Geostationary Operational Environmental Satellite (GOES)-West (9, 10, 11, and 15) visible albedo product over the western U.S. (25-50 °N, 130-113 °W) from the National Oceanic and Atmospheric Administration (NOAA) Comprehensive Large Array-data Stewardship System database (CLASS) (<https://www.class.ncdc.noaa.gov>). The dataset employed here spans twenty years (1996 to 2015) and has 1-km spatial and hourly temporal resolutions. The 1-km pixels are re-sampled to 4-km resolution to be consistent with the PRISM dataset (Section 3.2.1.4).

Physically, CC represents the fraction of the cloud cover in a pixel and is designed to linearly correlate with the atmospheric transmission (Cano et al., 1986). The cloud cover fraction here is defined as the ratio of cloud albedo to the pixel's dynamical range. The cloud albedo is defined as the difference between the raw albedo (α) and clear-sky albedo (α_{clear}), while the dynamical range is defined as the difference between the overcast albedo (α_{ovc}) and

α_{clear} . The dynamical range represents the actual α range occurring in a pixel [see Perez et al. (2002) for more detail].

Mathematically, CC is formulated as:

$$CC_{i,d,h} = \frac{\alpha_{i,d,h} - \alpha_{\text{clear}_{i,d,h}}}{\alpha_{\text{ovc}_{i,d,h}} - \alpha_{\text{clear}_{i,d,h}}} \quad (3.1)$$

where i is the GOES pixel, d is the day, h is the hour of the day. The α_{clear} is determined as the minimum albedo within a prescribed time window (Cano et al., 1986; Perez et al., 2002), assuming there is at least one day with a clear-sky condition within this time window [after Paech et al. (2009)]:

$$\alpha_{\text{clear}_{i,d,h}} = \min(\alpha_{i,d-d_0,h} : \alpha_{i,d+d_0,h}) \quad (3.2)$$

Setting d_0 to 7 days is sufficient to discriminate the more persistent snow cover from the less persistent cloud cover, while still allowing albedo fluctuations due to changing surface and non-cloud atmospheric properties, chiefly those related snow, moisture and vegetation (Perez et al., 2002; Sumargo & Cayan, 2017). Although α_{clear} fluctuates, α_{ovc} is relatively constant (Perez et al., 2002). Our diagnosis suggests that the highest α ever reached in our dataset is ~ 0.96 and that the results (Section 3.3) are virtually insensitive to α_{ovc} variations. Therefore, the α_{ovc} is set as 1 (opaque) for simplicity. The hourly dataset is subsequently averaged over daytime scenes [7-17 Local Standard Time (LST), given there is no missing data between 9 and 15 LST] to form daily composites that are consistent with the temporal resolution of the other datasets used in this study. Most of the days ($>90\%$) contain valid data.

3.2.1.2 Snow water equivalent

Daily snow water equivalent (SWE) records are retrieved from the California Data Exchange Center (CDEC) (<http://cdec.water.ca.gov/>) operated by the California Department

of Water Resources (CDWR) Cooperative Snow Survey (CSS) snow sensor records, and from the U.S. Department of Agriculture (USDA) Natural Resources Conservation Service (NRCS) Snow Telemetry (SNOTEL) records (<http://www.wcc.nrcs.usda.gov/snow>). Considering stations with records from 1996 to 2015, 235 stations are used in our analyses (8 from CDEC and 227 from SNOTEL) (Figure 3.1). Daily SWE change is approximated using a daily-centered SWE difference:

$$\Delta SWE_{i,d} = SWE_{i,d+1} - SWE_{i,d-1} \quad (3.3)$$

where i is the station and d is the day. Under this definition, snowmelt days are defined as having negative ΔSWE and when water leaves the snowpack (as snowmelt water may refreeze within the same snowpack during the cold night, especially in early snowmelt season). Unless otherwise noted, any $\Delta SWE > 0$ (accumulation) is not included our analysis since we focus on the snowmelt events. We hereby formulate snowmelt as:

$$MELT_{i,d} = -\Delta SWE_{i,d} \quad (3.4)$$

The days when both SWE and ΔSWE are zero are excluded from the analyses.

3.2.1.3 Streamflow

Streamflow (Q) is obtained from the U.S. Geological Survey (USGS) database (<http://waterdata.usgs.gov/ca/nwis/>). The Q dataset used here is a set of 79 snow-dominated Hydro-Climatic Data Network (HCDN) gauges (Slack and Landwehr, 1992) having minimal diversions and other human manipulations (Stewart et al., 2005), and having records from 1996 to 2015 (see Figure 3.1). Analogous to the snowmelt variable, daily streamflow change is approximated using a daily-centered Q difference:

$$\Delta Q_{i,d} = Q_{i,d+1} - Q_{i,d-1} \quad (3.5)$$

where i is the station and d is the day. Under this definition, increased daily streamflow is positive ΔQ .

3.2.1.4 Precipitation and surface air temperatures

We utilize Precipitation-elevation Regressions on Independent Slopes Model (PRISM) daily gridded precipitation (P), average (T_{avg}), maximum (T_{max}) and minimum (T_{min}) surface air temperatures (Daly et al., 1994, 2008; PRISM Climate Group). For this study, we use the 4-km horizontal resolution and daily temporal resolution version of PRISM data (Daly, 2013) from 1996 to 2015. Temperatures and precipitation are mated with snow pillow and stream gauge observations by assigning the closest PRISM grid box to a given snow pillow or stream gauge.

3.2.2 Contingency analysis of cloudiness and snowmelt

As an initial investigation of local cloudiness' relationship with snowmelt, we conduct a categorical evaluation using a contingency analysis (Pearson, 1904) and evaluate the results using the chi-squared test (Howell, 2011). We account for both snow accumulation and melt [determined using equation (3.3)] to compare how both snow regimes vary with different cloudiness regimes (clear, moderate and cloudy). An alternate contingency analysis using the diurnal temperature range ($dT = T_{max} - T_{min}$) as proxy for cloudiness is provided in the Supporting Information; the dT is inversely proportional to cloudiness and hence is a valid indicator of atmospheric transmittance (Grillone et al., 2012).

We derive three equally frequent categories of CC, defining clear condition as a day with CC less than its 33rd percentile value, cloudy condition as a day with CC greater than its

67th percentile, and moderate condition as anything in between. These tercile categories are derived for each site and each of the early (February-March), mid (April-May), and late (June-July) spring periods individually to examine how the relationship varies over different parts of the springtime. Although February can also be categorized as late winter when snow accumulation may still occur, and intermittent snow ablation can occur throughout the entire snow season, interannual climate variability can lead to the start of snow ablation period earlier than the canonical April 1st. Only days when snow is present (SWE > 0) are included in the analysis.

3.2.3 Multivariate linear regression analysis of cloudiness and snowmelt/streamflow

We construct multivariate linear regression models of MELT and of ΔQ with CC as the predictor to quantify the association of CC with MELT and ΔQ :

$$Y_{i,d} = \sum_n C_{i,d-n} * X_{i,d-n} + \varepsilon \quad (3.6)$$

$$X = \text{overhead CC} \quad (3.6a)$$

$$Y = \text{MELT, } \Delta Q \quad (3.6b)$$

$$C = \text{regression coefficient} \quad (3.6c)$$

$$\varepsilon = \text{error term} \quad (3.6d)$$

Here i is the station index, d is the concurrent day, and n is the number of days before d (for $0 \leq n \leq 5$ days). The regression model is configured such that the predictand is the anomaly of MELT or ΔQ on a given day, and the predictors are the anomaly of CC from 5 antecedent days up to the concurrent day. Each variable is de-seasonalized by subtracting its smoothed daily climatological value, derived using a 29-day centered (± 14 day) moving average of the daily climatological average of the time series. De-seasonalizing allows us to focus on

intraseasonal processes. Some examples of the raw and de-seasonalized time series of CC, MELT and ΔQ are shown in the Supporting Information.

A separate regression model is built for each month. Statistical significance is evaluated using an F-test (Fisher, 1925). The square of the correlation between the observed and the modeled MELT or ΔQ , i.e., the coefficient of determination (R^2), measures the amount of MELT or ΔQ variance accounted by the CC. The strength and sign of the regression coefficient (C) weighs the relative importance and represents the partial correlation of each predictor to MELT or ΔQ . Although collinearity between the predictors exists, our results (Section 3.3.3) demonstrate that the relative importance of the predictors can be evaluated consistently, e.g., with respect to the lag/auto correlation analysis (Section 3.3.2).

3.2.4 REOF analysis of cloud cover

A larger scale perspective is the extent to which snowmelt and streamflow respond coherently to regional cloudiness variations. To investigate this, Rotated Empirical Orthogonal Function (REOF) analysis of de-seasonalized daily CC over high-elevation terrains (>800 m) for all months of 1996-2015 were derived [see Sumargo & Cayan (2017) for an analog]. Principally, the REOF analysis here identifies the leading modes of CC. Each of these modes represents the areas where CC tends to vary in unison, in both space and time. The spatial component is called the REOF, while the temporal component, which is time-varying amplitude of the REOF, is called the Rotated Principal Component (RPC)

3.3 Results

3.3.1 Local cloudiness and snowmelt variations

Table 3.1 is the contingency table (see Section 3.2.2) showing the relationships between daily CC and snow accumulation/melt observed at Gin Flat (2,149 m elevation on the west slope of the Sierra Nevada in California). The χ^2 statistics from this contingency table indicate strong relationship in February-March, with most snowmelt days coincide with clear skies or moderate cloudiness, and snow accumulation days coincide with cloudy conditions. The relationship, judging by the χ^2 statistics, is strongest in April-May, but the distribution skews toward the melt regime. Warmer temperatures and generally greater solar heating in April and May increases the proportion of days with snowmelt; even on days with cloudy conditions snowmelt is relatively high (50% of all April-May cloudy days), but not nearly as high as on days with moderate sky cover (75%) or clear conditions (86%).

Table 3.1.

Numbers of Days associated with Snow Accumulation/Melt coincident with Clear/Moderate/Cloudy Sky for February-July of 1996-2015 at Gin Flat in California (37.767 °N, 119.773 °W, 2,149 m)

Period	MELT	CC			χ^2
		Clear	Moderate	Cloudy	
Feb-Mar	Accumulation	77	170	238	140.94
	Melt	143	86	38	
Apr-May	Accumulation	9	41	121	148.17
	Melt	258	231	148	
Jun-Jul	Accumulation	0	0	2	2.00
	Melt	5	36	40	

Note. The χ^2 value indicates the statistical significance of MELT-CC association (significant at 99% confidence level when $\chi^2 > 9.21$). Only days with non-zero SWE are included.

By early summer, much snow has melted, so there are much fewer days that register with snow to populate the contingency table (Table 3.1). However, based upon the available data, the strength of the relationship between cloudiness and snowmelt degrades in early summer (June-July) as temperature warms and snowpack has largely diminished, with most days registering as having snowmelt regardless of cloudiness category (clear, moderate and cloudy). A similar but slightly weaker (as indicated by the lower χ^2 values) pattern is obtained across the three periods when CC is substituted with dT (Supporting Information).

Most of the days with snowmelt in June-July occur under moderate or cloudy conditions. A closer inspection reveals the amount of snowmelt occurring under cloudy conditions tends to be lower (less than its median value), while that occurring under moderate and clear-sky conditions tends to be higher. This result indicates a limitation of contingency analysis. For example, a day with a small CC value in June/July may still be classified as cloudy, since CC tends to be small and does not vary as much during this period. The use of dT instead of CC does not relieve this issue, although it improves the χ^2 values for some NW sites that we inspect, e.g., Crater Meadows in Idaho (Supporting Information), where cloudiness tends to be relatively persistent across the snowmelt season.

Interestingly, the contingency table contains some days with snow accumulation that coincide with clear-sky conditions. Considering the definition of snow accumulation here, snow accumulation events occurring on the days following those with a clear-sky condition may be responsible. Indeed, ~63% of such days are followed by days with snow accumulation. On the other hand, unlike the snow accumulation, CC does not include information from the preceding or following day. Moreover, CC is a daytime average (7-17

LST), so cloud processes occurring specifically during the early hours and/or the previous night would fail to register in the contingency table.

Similar results and issues are obtained at relatively nearby (e.g., Lower Kibby Ridge and Tuolumne Meadows in California) and distant (e.g., Crater Meadows in Idaho and Stampede Pass in Washington) sites.

3.3.2 Antecedent cloudiness and snowmelt/streamflow fluctuations

In considering effects of cloudiness on snowmelt and streamflow fluctuations, it is of interest to determine if snowmelt is preconditioned by anomalous cloudiness (and thus the amount of radiation) occurring one or more days prior to a given day. To address this, Figures 3.2a and 3.2b show 0-to-5-day lag correlations between de-seasonalized daily CC and de-seasonalized daily MELT anomalies for February-July at two snow pillow sites: a) Gin Flat in California (to represent SW) and b) Crater Meadows in Idaho (to represent NW). Additionally, Figures 3.2c and 3.2d show the lag correlations between de-seasonalized daily CC and de-seasonalized daily ΔQ for the same period at two snow-dominated streams: c) Merced River at Happy Isles Bridge in California, d) South Fork Clearwater River at Stites in Idaho. Like in Section 3.2.3, the de-seasonalizations are done by subtracting the smoothed daily climatological values, derived using a 29-day centered (± 14 day) moving averages of the daily climatological averages of the time series.

Gin Flat and Merced River at Happy Isles Bridge are located within the Yosemite National Park on the west slope of the Sierra Nevada. The Sierra Nevada is characterized with the maritime snowpack regime, with relatively high snowpack and shorter accumulation period (Trujillo & Molotch, 2014). Crater Meadows and South Fork Clearwater River at

Stites are located near the Clearwater National Forest on the Northern Rockies. The Northern Rockies is characterized by the intermountain snowpack regime, with relatively low snowpack and longer accumulation period (Trujillo & Molotch, 2014).

Figures 3.2a and 3.2b exhibit predominantly negative correlations in April-May and, to a lesser extent, in March and June. Negative correlations signify the role of clear skies driving snowmelt and cloud shading in reducing snowmelt. Significant correlations (magnitudes >0.4 and p-values <0.01) at 1-day to 4-day lags suggest that a form of preconditioning operates, where prior-day cloudiness reduces concurrent-day snowmelt. These significant negative correlations also suggest the dominance of cloud-shading effect over the enhanced longwave radiation effect associated with greater cloudiness (Zhang et al., 1996; Stone, 1997; Stone et al., 2002), as the latter can counteract the cloud-shading effect by enhancing snowmelt and runoff.

Importantly, most of these correlations peak at 1-day to 2-day lags, indicating a delayed response of MELT and ΔQ to cloudiness. The autocorrelations (R_{auto}) of de-seasonalized CC drop with time lags, especially at lag > 1 day (e.g., $R_{\text{auto}} = 1, 0.52, 0.28, 0.12, \dots$ at lag = 0, 1, 2, 3, ... days at Gin Flat in April), suggesting the lagged CC-MELT and CC- ΔQ correlations are not simply a signature of persistent multi-day CC anomalies. Stronger correlations typically have longer lags in the early snowmelt season when radiative energy input is lower (discussed in Section 3.3.3.1) and when snowpack is thicker and colder. In such a condition, snowpack requires a longer time to buildup the energy before snowmelt can begin.

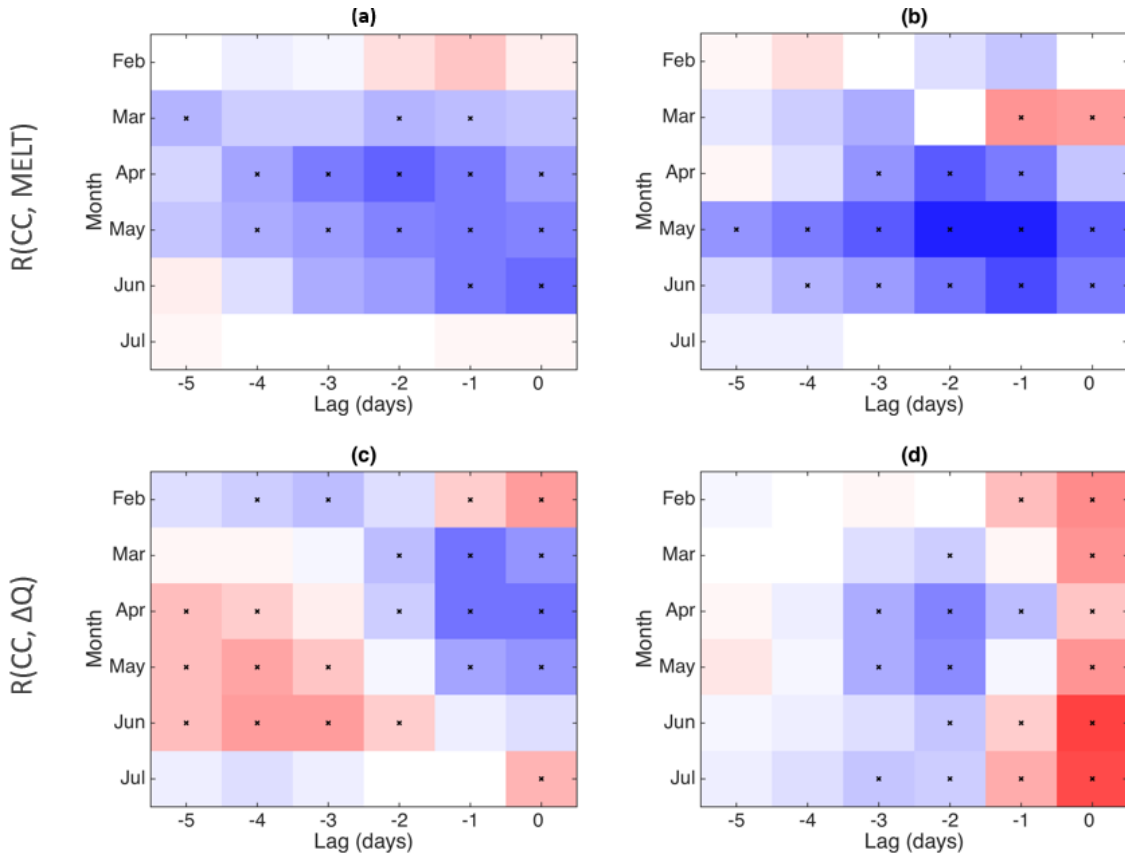


Figure 3.2. Upper: Correlation between de-seasonalized overhead CC and subsequent and concurrent MELT at (a) Gin Flat in California (37.767 °N, 119.773 °W, 2,149 m) and (b) Crater Meadows in Idaho (46.56 °N, 115.29 °W, 1,817 m). Lower: Correlations between de-seasonalized overhead CC and subsequent or coherent ΔQ at (c) Merced River above Happy Isles Bridge in California (37.732 °N, 119.558 °W, 1,224 m) and (d) South Fork Clearwater River at Stites in Idaho (46.087 °N, 115.976 °W, 400 m). Lag < 0 indicates CC leads MELT, ΔQ . The symbol ‘x’ denote statistically significant correlations at 99% confidence level (p-value < 0.01).

Figure 3.2b also shows positive CC-MELT correlations at zero and 1-day lags in March, which seems to indicate snowmelt occurrence during days with cloudy conditions. In March, positive P vs. MELT lag correlation is similarly present (not shown). Further examination reveals ~34% of all March days with snowmelt receive measurable precipitation ($P > 0.254$ mm) and coincide with above freezing T_{avg} , suggesting rain-on-snow events may be involved (see Section 3.3.3.1). However, this correlation becomes negative if MELT

includes accumulation regime, indicating it is an artifact of the analysis method, since Figure 3.2b does not include cloudy days having positive snow accumulation.

Turning to CC vs. ΔQ , Figures 3.2c and 3.2d exhibit some positive correlations at zero to 1-day lags, mainly in February and March, but also in June and July. This feature illustrates a near-term relation with cloudiness, likely reflecting the effect of precipitation and nearly immediate runoff (see Section 3.3.3.2). Additionally, Figure 3.2c also displays relatively strong positive correlations at longer lags in April-June. In April and May, this pattern may reflect the effects of clear/cloudy sky interludes associated with synoptic scale weather events. In June, the snowpack and its runoff are largely diminished, as shown by the weak negative correlations. The strong positive correlations at longer lags may simply reflect multi-day cumulative effect of clear skies, signifying the drying effect of summertime.

The pattern of CC- ΔQ correlations must reflect the different processes operating in different watersheds. Strongest negative correlations occur in April at both Merced River and South Fork Clearwater River, with a peak at 1-day lag for the former and at 2-day lag for the latter. However, statistically significant negative correlations fall away after May at the relatively southern Merced River, but are present through July at the relatively northern South Fork Clearwater River. This result reflects the snowpack's tendency to last longer in NW than in SW. Both sites exhibit statistically significant positive correlations at lag zero in July, signifying the immediate effect of rainfall runoff on streamflow.

3.3.3 Snowmelt/streamflow variations accounted by local cloudiness variability

The correlations in Figure 3.2 demonstrate that, to a certain extent, CC is linearly correlated to MELT and to ΔQ . Following this thread, in this section we use multivariate

regression analysis (see Section 3.2.3) to investigate patterns of linear associations and to what extent CC fluctuations explain variances of MELT and ΔQ . The regression results vary through the snowmelt season, as shown for MELT (ΔQ) on the left (right) column in Figure 3.3 for February, April and June, covering late winter through early summer when various stages of snowmelt occur.

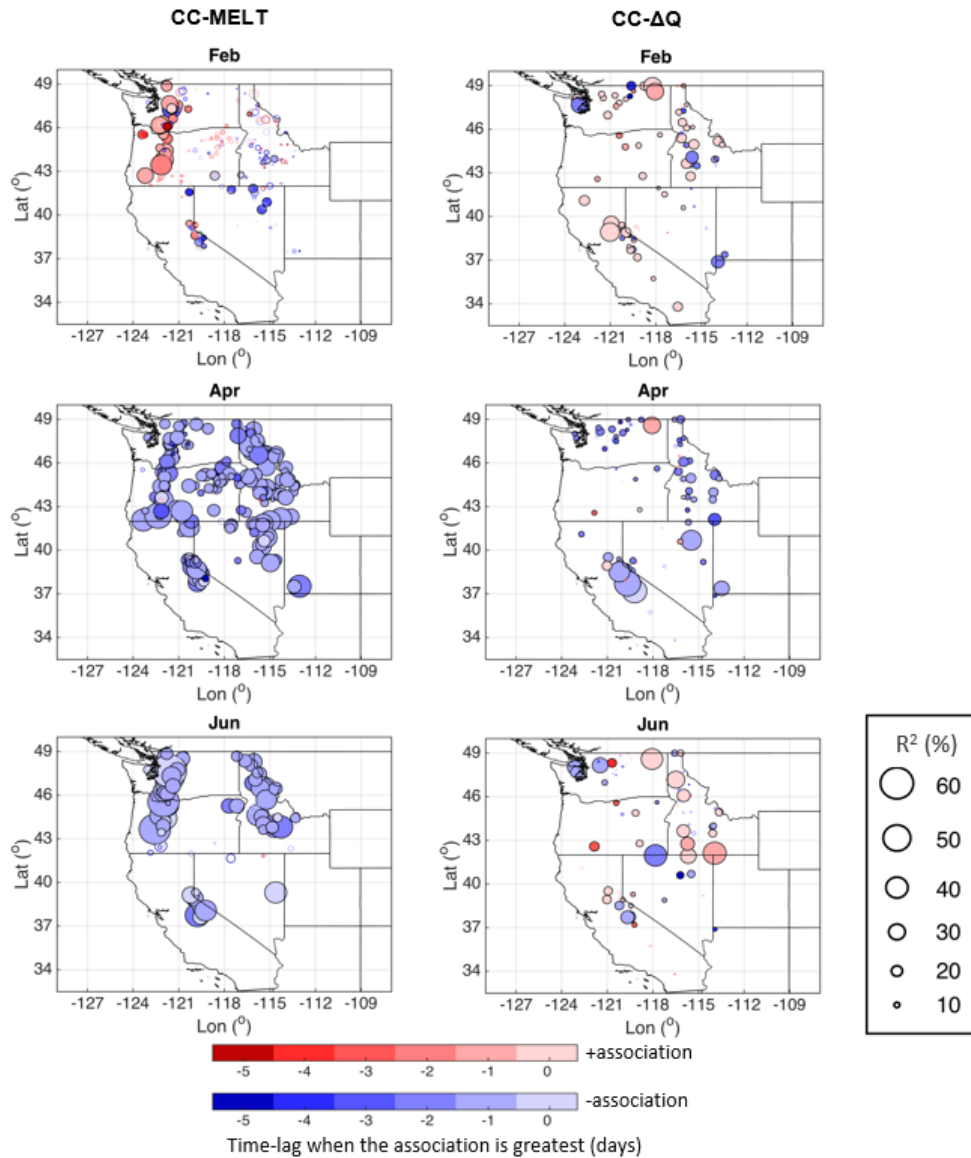


Figure 3.3. Variances of MELT (left) and of ΔQ (right) anomalies explained (%) by anomalous CC predictors in lagged multiple regressions for February, April and June of 1996-2015. Circle size is proportional to R^2 (%). Color tone represents the time lag whose regression coefficient magnitude is strongest, where red (blue) denotes positive (negative) correlation and lag < 0 means CC leads MELT/ ΔQ . Sites with p -value < 0.01 are color-filled.

3.3.3.1 Cloudiness and snowmelt variability

The left column in Figure 3.3 and Tables 3.2 and 3.3 display results from the CC-MELT regressions. The CC-MELT association (R^2) is generally greater in the relatively low elevation northwestern sites (averaging $\sim 1,637$ m) than in the relatively high elevation

southwestern sites (averaging ~2,360 m), and largest in May for all regions (Table 3.2). Some differences also occur between the windward and the leeward sites, with the windward sites having larger R^2 (by ~4% on average) and more negative CC-MELT correlations. The windward-leeward differences may reflect the generally drier climate and snow characteristics of the leeward sites, resulting in less robust CC-MELT relationships. In total, 611 of the 1,410 snowmelt models (from 235 snow pillows and every month of February-July) exhibit statistically significant R^2 results (p-values < 0.01), as determined from the F-test.

Table 3.2.

Area-averaged R^2 (%) of Multiple Regression-modeled MELT, February-July 1996-2015

Month	NW	SW	WUS
Feb	8	6	8
Mar	8	12	9
Apr	17	19	17
May	27	22	25
Jun	24	19	23
Jul	21	7	20

Note. The R^2 are averaged over 173 sites in the Northwest (NW), 62 sites in the Southwest (SW) and 235 sites in the whole western U.S. (WUS), reflecting the degree to which MELT fluctuations are explained by CC variability. The boldface numbers indicate MELT at most of the locations (>60%) have negative correlations with CC.

This result persists, with comparable R^2 across months and regions, when the model and statistics are built and evaluated for training and validation periods separately (Appendix 3.B). However, site-to-site variations can occur. For instance, the peak association occurs in April at Fish Lake and Gin Flat, but it occurs in May at Crater Meadows and Stampede Pass (Table 3.3). Gin Flat also exhibits a secondary peak in June, consistent with the pattern shown in Figure 3.2. The result also differs from dry years to wet years, with generally larger R^2 but shorter snowmelt season in dry years (Appendix 3.C). The windward-leeward

differences are weaker in drier years when the reductions in cloudiness and snowpack are likely greater on the windward sites, with the R^2 of the windward sites being larger by only ~2% on average.

Table 3.3.

The R^2 (%) of Multiple Regression-Modeled MELT for Some Selected Stations

Month	CRM	FIL	GIN	STP
Feb	13	5	5	13
Mar	13	13	11	6
Apr	32	44	30	9
May	53	25	28	21
Jun	33	--	40	15
Jul	--	--	--	--

Note. Stations are Crater Meadows (CRM) in Idaho (46.56 °N, 115.29 °W, 1,817 m), Fish Lake (FIL) in Oregon (42.38 °N, 122.35 °W, 1,420 m), Gin Flat (GIN) in California (37.767 °N, 119.773 °W, 2,149 m) and Stampede Pass (STP) in Washington (47.27 °N, 121.34 °W, 1,174 m).

In February, as shown in Figure 3.3 (top row), most SW and interior NW locations exhibit weak and inconsistent (both positive and negative) CC-MELT relationships, with only 47 snow pillow sites yield statistically significant results (p -value < 0.01), signifying minimal snowmelt activities. In contrast, Figure 3.3 shows that most Cascade locations, including Stampede Pass in Table 3.3, exhibit moderate positive CC-MELT correlations, indicating cloudier (clearer) sky produces more (less) snowmelt. This occurrence may reflect greater snowmelt due to enhanced incoming longwave radiation flux with cloudiness (Zhang et al., 1996; Stone, 1997; Stone et al., 2002) and/or rain-on-snow events (Würzler et al., 2016). The relatively low elevations of Cascade Mountain sites (averaging ~1,374 m, compared to ~1,902 m over the interior NW and ~2,360 m over SW) may also allow more rain-on-snow episodes by having more days with above freezing temperature and liquid

precipitation. Rain-on-snow events have been shown to be relatively common in the Cascades (McCabe et al., 2007).

Subsequent scrutiny of days in February when cloudy days coincide with snowmelt, i.e., when both CC and MELT anomalies are positive, shows that most have above-freezing T_{avg} and positive T_{avg} anomalies. Further, when February days registering precipitation are excluded from the analysis, the CC-MELT associations at stations along the Cascades diminish, indicating the presence of rainfall on cloudy days with snow loss (i.e., an impact of rain on snow). This result is similarly reflected by the relative importance of P compared to CC, T_{max} and T_{min} in February (Supporting Information).

From March onward, almost all locations across the WUS exhibit negative correlations, indicating cloudier (clearer) skies produce lesser (greater) snowmelt. The number of locations exhibiting statistically significant results also increases (87 sites). Negative regression coefficients demonstrate the dominance of cloud-shading (or SWF when clouds are lacking) effects over other processes, such as the cloud-precipitation.

Reinforcing results from Figure 3.2, MELT often exhibits a delayed peak response to CC, as shown by the color-coding in Figure 3. The delay becomes progressively shorter through the snowmelt season. In February-March, the peak CC association is less definite. A slight majority of locations has peak associations from 1-day (112 sites total for February-March) to 2-day (114 sites) lags, with most of the rest of the maxima occurring at zero lag (92 sites) and even fewer at each of the lags >2 days.

During the early snowmelt season (February-March), snowmelt requires preconditioning by a warming phase, i.e., when snowpack temperature is raised to an isothermal condition at the melting point, followed by the ripening phase when melting starts

to occur at snow surface and the melt water subsequently percolates into deeper, colder layer in which it refreezes (Dingman, 1994; Boike et al., 2003). Thus, snowmelt during these months may happen more slowly regardless of cloudiness fluctuations (also see Supporting Information). By April, shown by the light blue color-shading, the number of locations having peak associations at 1-day lag increases, and the number at lags >1 day decreases significantly, especially in SW. In April, there are 200 sites exhibiting statistically significant results. This transition to more rapid responses reflects the greater solar heating and warmer climate and, presumably, earlier spring onset in SW. In fact, CC becomes increasingly important in modulating MELT in April (Supporting Information).

The number of sites with peak association at zero lag rises to 58 in May, which also has 126 sites with peak association at 1-day lag, but only 51 sites with peak association at lag >1 day. The number of sites with statistically significant results is slightly fewer (181 sites) than that in April.

In June and July when both cloudiness and snowpack have diminished, the number of locations with highest association with CC at zero lag becomes commonplace. Furthermore, only 86 sites in June and 10 sites in July produce statistically significant results. This shift corresponds to a more rapid response of snowmelt to heating in late spring and summer as solar irradiance increases, snowpack diminishes, and snow temperature has increased, inducing the output phase when runoff initiates and the melt water is produced proportionally to the energy input (Boike et al., 2003).

3.3.3.2 Cloudiness and streamflow variability

The CC- ΔQ regression results (right column of Figure 3.3 and Table 3.4) are not as strong and consistent as those for CC-MELT. The R^2 values for streams exhibiting statistically significant regression model results (p -value < 0.01), averaged over the WUS and over February-July, are only 9.6%. In comparison, the area and snowmelt season average R^2 value of CC-MELT regressions are 22.5%. However, like in the CC-MELT case, the windward sites tend to have larger R^2 (by $\sim 3\%$ on average), although this windward-leeward difference is not weaker in drier years. In total, 313 of the total of 474 streamflow regression models (from 79 stream gauges and every month of February-July) exhibit statistically significant results, as determined from the F-test at the 99% level of significance.

Table 3.4.

R^2 (%) of Multiple Regression-modeled ΔQ for February-July of 1996-2015

Month	NW	SW	WUS
Feb	7	7	7
Mar	5	8	6
Apr	6	10	7
May	7	6	7
Jun	6	6	6
Jul	9	6	8

Note. The R^2 averaged over 51 sites in the Northwest (NW), 28 sites in the Southwest (SW) and 79 sites in the whole western U.S. (WUS), reflecting the degree to which ΔQ fluctuations are explained by CC variability. The boldface numbers indicate ΔQ at most of the locations ($>60\%$) have negative correlations with CC.

The relatively weak associations and large residuals (not shown) between the modeled and measured ΔQ during the peak snowmelt season seem to reflect the convoluting effects of multiple factors directly or indirectly related to cloudiness, including precipitation, evapotranspiration, local and upstream snowmelt-runoff. For instance, cloudiness can reduce net radiation and thus evapotranspiration, which in turn allows higher streamflow. The

importance of the cloudiness to evapotranspiration is stronger than that of temperature and is accentuated in the spring when the intraseasonal variability of evapotranspiration anomaly associated with cloudiness is highest (Hidalgo et al., 2005). Likewise, greater snowmelt rate (Barnhart et al., 2016), cooler temperature and higher soil moisture during antecedent cool season (Woodhouse et al., 2016), which are not accounted for in this study, correlate with higher flows. The generally weak linear associations of T_{\max} , T_{\min} and P with ΔQ similarly reflect this phenomenon (Supporting Information).

The most consistent model results appear in April (Figure 3.3, middle row) and May (not shown, but similar to April), when the strongest linear correlations are negative, i.e., greater (lesser) cloud cover yields negative (positive) flow departures. The other months exhibit lower R^2 and less consistent correlations between CC and ΔQ , having both negative and positive correlations. Similar results are retained even when the model and statistics are built and evaluated separately for the training and validation periods (Appendix 3.B). These seasonally varying results are also illustrated in dry-year and wet-year subsets (Appendix 3.C). For the dry-year subset, June stands out in having relatively large positive correlations throughout most of the WUS, evidently indicating precipitation effect on streamflow.

In February, CC and ΔQ are weakly correlated, with 62 of the 79 stream gauge sites registering statistically significant results. There is 1 site in northern California and 2 sites in eastern Washington that yield $R^2 > 20\%$ (Figure 3). The map shows that the strongest correlations are predominantly positive, mostly (~58%) occurring without time lag. This result indicates streamflow fluctuations are inconsistently related to cloudiness. For instance, the streamflow increases occur with rainfall. In a few other cases, the streamflow increases

occur under clear skies as shown by negative correlations, which presumably induces snowmelt.

In March, stronger associations reflect that snowmelt occurrence has become widespread across the WUS. More locations exhibit negative correlations and time lags, mainly in central California and southern Idaho, albeit only 53 sites yield statistically significant results. The negative correlations confirm the cloud shading mechanism, i.e., ΔQ increases as CC decreases, and vice versa. The previously noted sites with positive correlations and $R^2 > 20\%$ have diminished, presumably with the declining winter precipitation, indicating snowmelt becomes more important than precipitation in streamflow generation. Although the number of sites with peak associations at zero lag is still dominant (23 sites), those at 1-day and 2-day lags are comparable (21 sites each). The emergence of peak timings at 1-day and 2-day lags underlines the role of upstream processes on streamflow.

As the snowmelt season progresses, the association between cloudiness and streamflow fluctuations peaks in April in the SW (centered in California) and in May in the NW (centered in Idaho) (Table 3.4). In these peak months, the number of locations with peak negative correlation at time lags of one or more days increases (68 sites in April and 73 sites in May) when compared to March (56 sites). The lengthening of travel-time from source regions as snow lines retreat to higher elevations apparently contributes to the increases in lag time (Lundquist et al., 2005). There are 60 sites in April and, interestingly, only 50 sites in May that yield statistically significant results.

The associations between CC and ΔQ change markedly in June, with shifts from negative to positive correlations at many locations throughout the WUS (37 sites), with 38

sites exhibiting statistically significant results. This shift intensifies in July (50 sites), most notably in Central California where a cluster of positive relationships emerges. Correspondingly, the number of sites with statistically significant results increases to 50 sites.

Analogous to the CC-MELT linear associations, the emergence of statistically significant positive CC- ΔQ correlations appear, on one hand, to reflect a runoff response to rainfall. These positive correlations also signify the drying that takes place with the onset of summer (i.e., less cloud, more solar radiation but little or no snow to melt and feed the streams), where evapotranspiration becomes the dominant influence on streamflow fluctuations (Lundquist & Cayan, 2002; Mutzner et al., 2015). The result from a contingency analysis (as in Table 3.1) performed on ΔQ at some selected gauge locations suggests that negative ΔQ anomalies tend to coincide with clear-sky condition (Supporting Information), which verifies the drying effect of summertime.

3.3.3.3 Elevational dependence of snowmelt and streamflow responses to cloudiness variability

The CC-MELT and CC- ΔQ associations depend upon elevation (Figure 3.4, left column). In the MELT case, the magnitudes and signs of the correlations (r) between the MELT response to CC and elevation vary considerably across months, reflecting changes in snowmelt processes with elevation across the melt season. The strength of MELT response decreases with elevation in February ($r = -0.35$), increases with elevation in March ($r = 0.22$) and April ($r = 0.15$), and again decreases with elevation in May ($r = -0.12$), June ($r = -0.33$) and July ($r = -0.48$).

The negative r in February corresponds to the precipitation effect in early snowmelt season, i.e., rainfall at lower elevations and snowfall at higher elevations. Positive CC-MELT associations at most lower elevation sites (>70% of all low elevation sites) and only a few positive CC-MELT associations at higher elevation sites (<40%) further confirm this result. The negative r in May onwards corresponds to the earlier and greater drying effect at lower elevations in late snowmelt season.

The positive r in March-April suggests higher MELT sensitivity to CC at higher-elevation sites during the peak snowmelt season, when SWE is typically greatest. During the peak snowmelt period, solar radiation and, plausibly, cloud-shading effect are higher than during the early snowmelt season, especially at colder, higher-elevation sites. Downward longwave radiation associated with the vegetation may complicate CC-MELT relationship in lower elevation areas, where vegetation density is typically higher.

The ΔQ case is more complicated, since the stream gauges generally are situated downstream of a considerable higher elevation catchment area upstream, so the elevation identified by the gauge elevation is only an index of true elevation (Figure 3.4, right column). The correlations between ΔQ response (R^2) to CC and elevation range from -0.3 in February to 0.37 in May. The negative correlation in February indicates the higher ΔQ sensitivity to CC variation at lower-elevation gauges during early snowmelt season. Positive correlations are observed from March to June, indicating higher ΔQ sensitivity to CC variation at higher-elevation gauges during peak snowmelt season. This pattern is consistent with the CC-MELT results and consequently demonstrates the snowmelt-runoff association with streamflow. Higher sensitivity to CC at lower-elevation gauges may reflect the dependence of these gauges on both local runoff and upstream tributaries. By July, the correlations fade ($r = -$

0.07), indicating the dependence of streamflow fluctuations on cloudiness varies little with elevation.

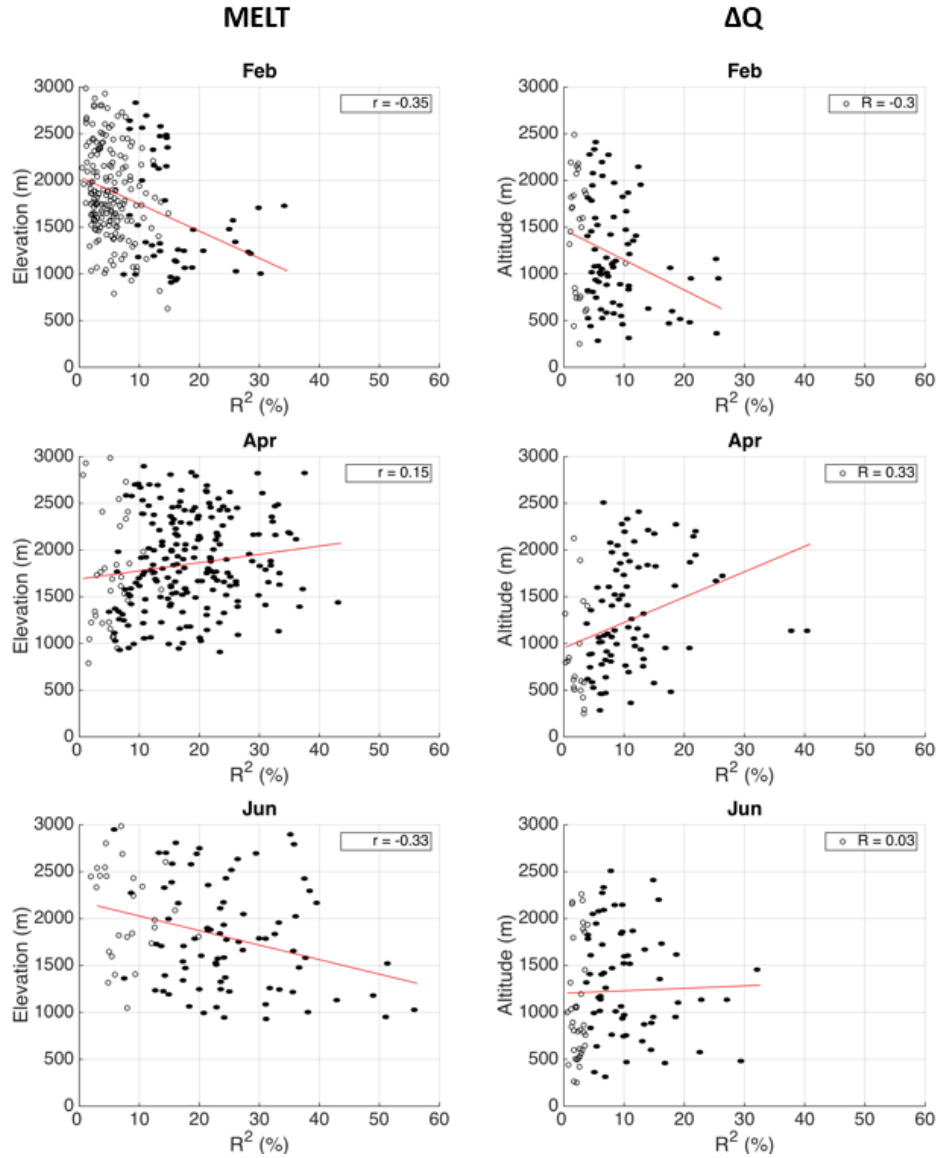


Figure 3.4. Scatter plots of R^2 between modeled and measured MELT (left) and ΔQ (right) as a function of station altitude for February, April and June, showing the variations of CC-MELT association with elevation and month. The red lines are least-square fits denoting the data trends. Sites with p -value < 0.01 are color-filled.

3.3.4 Regional cloudiness vs. snowmelt/streamflow variability

The two leading CC REOF modes representing regionally coherent non-seasonal cloud variability over NW and SW are displayed in Figures 3.5 and 3.6 (left panels), respectively. The time-varying amplitudes (RPCs) of these two REOF modes are then correlated with MELT and ΔQ over all snow and stream locations in the WUS for February, April and June (Figures 3.5 and 3.6, center and right panels).

The correlations demonstrate how anomalous cloudiness is associated with short period snowmelt and streamflow fluctuations over regional scales. The resulting maps exhibit correlations over relatively broad regions, with highest p-values < 0.01 in locations with large REOF weightings. The REOF-NW correlations with MELT and ΔQ are strongest over Idaho (Figure 3.5), while the REOF-SW correlations with MELT and ΔQ are strongest over California and Nevada (Figure 3.6). The REOF-MELT correlations are relatively strong, with values < -0.3 in many cases. Compared to the REOF-MELT correlations, the REOF- ΔQ correlations are weaker, evidently reflecting the complex variation of short-term streamflow fluctuations and the multifold controls that affect them (Section 3.3.3.2).

As exhibited by the local regression models, predominantly negative correlations between CC and MELT, and between CC and ΔQ during springtime indicate the role of cloud shading. In other words, as cloudiness increases, solar insolation decreases and as a result, there is less energy input to melt the snowpack that in turn feeds streamflows. However, some sizeable positive correlations also occur, most notably over NW in February in MELT case (Figure 3.6), indicating snowmelt occurrence with greater cloudiness. ΔQ case shows notable positive correlations over the northern Idaho and southern California/Nevada

in February and June (Figures 3.5 and 3.6), indicating a more immediate runoff as a response to greater cloudiness and, presumably, rainfall.

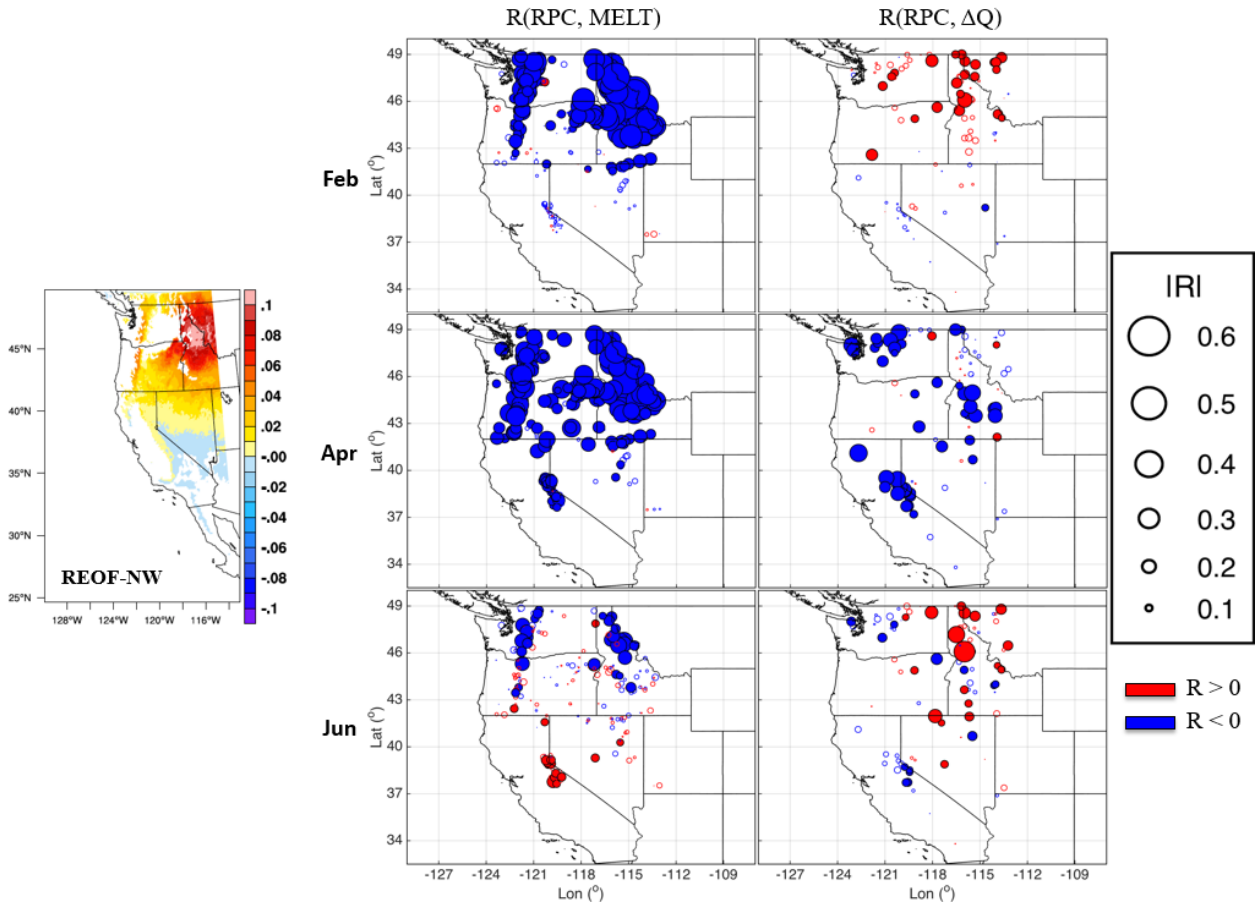


Figure 3.5. Left: The NW REOF of February to July de-seasonalized daily CC anomalies from 1996-2015. Center: Correlations between the NW RPC daily time series and MELT anomalies for February, April and July. Right: Same as center panel, except between the NW RPC time series and ΔQ . Sites with p-value < 0.01 are colored-filled.

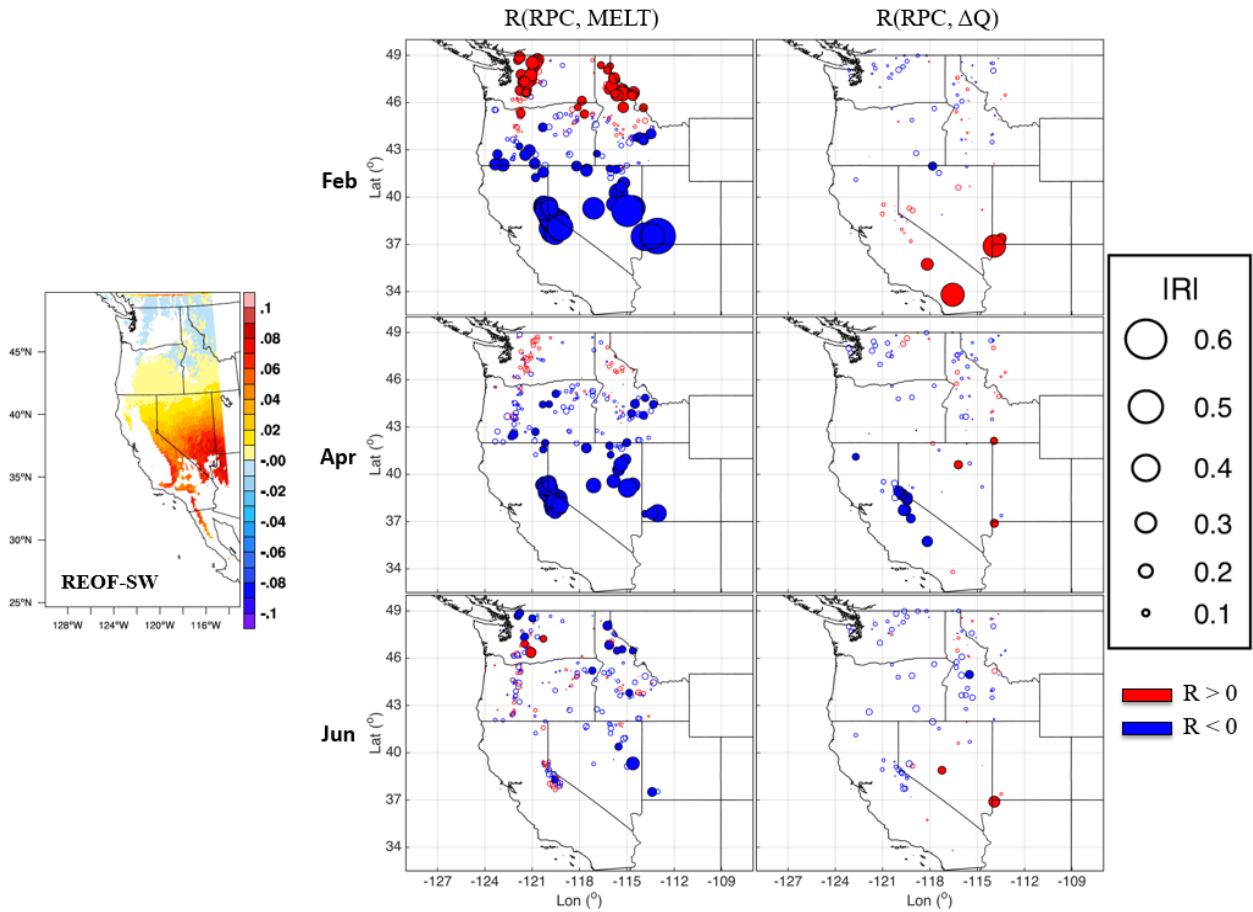


Figure 3.6. Same as Figure 3.5, except for the SW daily CC REOF.

3.4 Summary and conclusions

The results demonstrate the varying degrees to which daily cloudiness (CC) variability linearly correlates with daily snowmelt (MELT) and daily streamflow (ΔQ) fluctuations over the western U.S. within the snowmelt season (February-July). The CC-MELT association is greater in the relatively low elevation northwestern sites than in the relatively high elevation southwestern sites. The CC- ΔQ associations vary in magnitude, but not systematically, across the western U.S. Both CC-MELT and CC- ΔQ associations vary considerably over the period between February and July.

While cloud cover is often associated with precipitation, it also provides shading for the snowpack and thus modulates the melt and runoff timings during the springtime. Contingency analysis and linear regressions reflect this shading mechanism, showing that snowmelt tends to coincide with clear days, and vice versa, especially in mid spring (April-May). This effect also shows up in an asymmetry between dry and wet years, where negative springtime CC correlations with MELT and with ΔQ are more persistent, albeit weaker, in wetter years, particularly in the southwest. The dry vs. wet years asymmetry may also provide an outlook on the variations in snowmelt and streamflow responses to cloudiness variability under the future intensification of dry/wet hydrologic extremes (Swain et al., 2018). Importantly, cloudiness-driven MELT and ΔQ fluctuations operate on regional scales, demonstrated by temporal correlation coefficients between the CC rotated empirical orthogonal functions and anomalies of MELT and ΔQ .

Throughout the western U.S., snowmelt tends to have a lagged as well as a contemporaneous response to cloudiness variations. Regressions indicate that fluctuations of daily snowmelt are associated with variations in cloudiness of that day itself as well as variations of cloudiness on antecedent days. For many months and locations, correlations of cloudiness with snowmelt or streamflow fluctuations have peak values when cloudiness leads by one to three days. This phenomenon is likely related to snowpack energy depletion throughout its depth, so cold content increases and melt is inhibited. Peak correlations between cloud variations and snowmelt fluctuations exhibit longer lags in the early season when days are shorter and cooler, and snowpack is thicker. Streamflow also exhibits a delayed relationship with cloud variations, but they operate at longer lags. For streamflow,

upstream effects sometimes dominate local processes (Lundquist et al., 2005), which introduce time delays into the peak CC- Δ Q associations.

Finally, although elevation is clearly an important factor in seasonal snowpack and runoff generation (Garvelmann et al., 2015; Gleason et al., 2017; Tennant et al., 2017), cloudiness-associated snowmelt and streamflow fluctuations also appear to depend on the elevation. This dependence is complex, however. CC-MELT and CC- Δ Q associations are stronger at lower elevations in the early (particularly February) and late (particularly July) snowmelt season, but are stronger at higher elevations in the peak snowmelt season (particularly March and April) when overall snowmelt is greatest.

In summary, cloudiness influences snowmelt and streamflow in different ways throughout the snowmelt season, i.e., the cloud-precipitation effect in early and late snowmelt season, and cloud shading effect in peak snowmelt season. The relatively inactive snowmelt earlier in the season, followed by peak activity in April-May and decline in June-July underpins a link between snowpack dynamics and annual streamflow, which Rheinheimer et al. (2016) similarly noted from their work at Yuba River watershed in northern California. The low-to-moderate strengths in these linear associations indicate the non-linear nature in cloudiness-snowmelt-streamflow processes, and that other factors are involved in snowmelt and streamflow fluctuations. The lagged peak associations suggest the importance of antecedent cloudiness variations, which are important in understanding snowmelt and streamflow fluctuations.

Future works should address the non-linearity in cloudiness-snowmelt and cloudiness-streamflow relationships and how these relationships may evolve with future hydroclimatic changes. If the study involves “big data”, machine learning techniques will be

particularly useful when non-linearity is present (Bair et al., 2018). Other aspects needing further investigations include the effects on cold content, longwave and turbulent fluxes, and what roles local topography and vegetations play in these relationships. In addition, streamflow is a confluence of upstream snow-fed tributaries and is thus affected by upstream cloudiness. Consequently, upstream cloudiness is an important variable with potential applications in hydrologic predictions, such as dam and reservoir operations.

Acknowledgements

Edwin Sumargo was funded by the California Department of Water Resources Award 4600010378. Daniel Cayan was funded by the California Energy Commission, the NOAA RISA program, and the Southwest Climate Science Center sponsored by the U.S. Department of Interior and the USGS. Many thanks to Michael Dettinger, Jan Kleissl, Joel Norris, Shang-Ping Xie, and three anonymous reviewers for the thoughtful comments and discussions. GOES albedo product was retrieved from NOAA CLASS website at <https://www.class.ncdc.noaa.gov>. The cloud cover indices can be accessed from Sumargo & Cayan (2018) repository on <https://doi.org/10.6075/J0PC30K6>. Snow water equivalent was obtained from CDWR/CSS CDEC website at <http://cdec.water.ca.gov/> and USDA/NRCS SNOTEL website at <https://www.wcc.nrcs.usda.gov/snow/>. Streamflow was obtained from USGS website at <http://waterdata.usgs.gov/ca/nwis/>. Daily precipitation, maximum and minimum temperatures were obtained from Oregon State University PRISM climate group website at <http://prism.oregonstate.edu/>. This chapter, in full, has been submitted for publication to *Water Resources Research*, with slight modifications. Sumargo, E., and D. R. Cayan, 2018: The Influence of Cloudiness on Hydrologic Fluctuations in the Mountains of

the Western United States. *Submitted for publication in Water Resour. Res.* The dissertation author was the primary investigator and author.

Appendix 3A: Cloudiness relationships with precipitation and diurnal air temperature

Linear relationships among cloud cover (CC), precipitation (P), diurnal air temperature range (dT), i.e., the difference between daily maximum and minimum air temperatures, are investigated. For this purpose, correlations formed from each pair of the four variables for individual months to investigate the sign and strength of correlations, and how they vary through the year.

Figure 3.A1 shows the correlations for two sites representing different regions (Figures 3.1, 3.5 and 3.6). The CC has strong positive correlations ($R > 0.5$) with P and strong negative correlations ($R < -0.5$) with dT at both sites, despite the monthly variations, inferring the close connection between cloudiness and precipitation and the cloud modulating effect on daytime and nighttime temperatures. For the latter, cloud cover reduces the incoming solar radiation at the surface during the daytime, which cools the daytime temperature. In contrast, cloud cover traps outgoing longwave radiation from the surface, which warms the nighttime temperature. These strong correlations are evident during springtime, emphasizing the importance of CC on P and dT, and their relevance to spring snowmelt. Similarly but to a lesser degree, P has strong negative correlations with dT ($R < -0.4$).

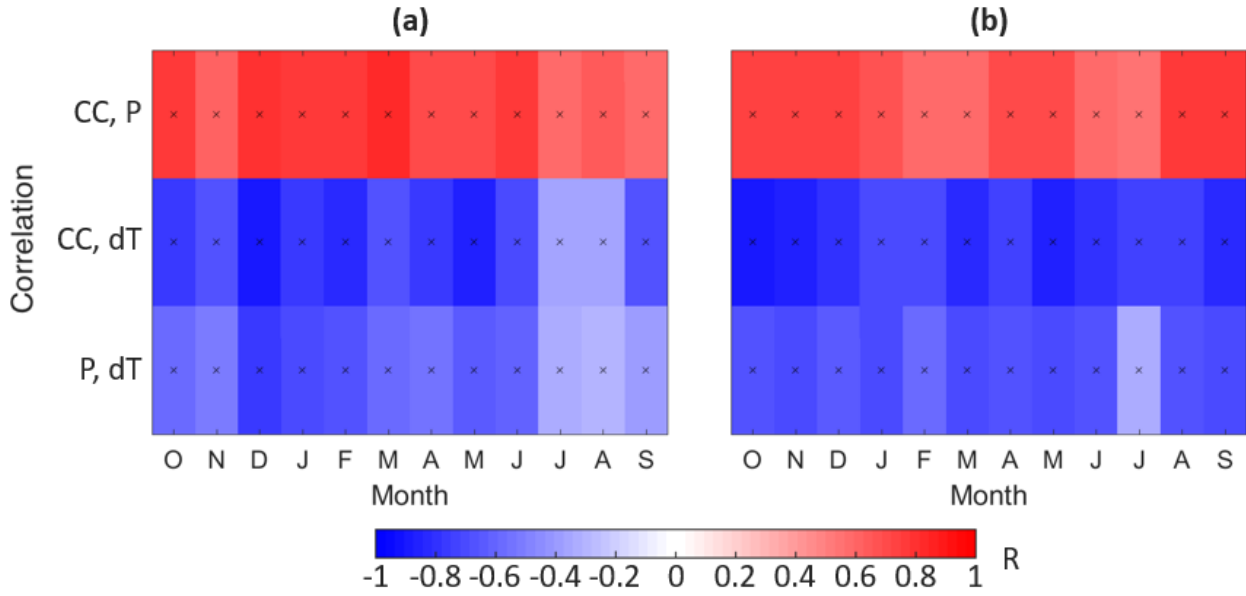


Figure 3.A1. Monthly correlations (R) (1996-2015) between de-seasonalized CC, P, and dT at (a) Gin Flat in California (37.767 °N, 119.773 °W, 2,149 m) and (b) Crater Meadows in Idaho (46.56 °N, 115.29 °W, 1,817 m), ordered according to water-year months (October-September). The symbol ‘x’ denote where p-value < 0.01.

Appendix 3B: Training and validation of MELT and ΔQ models

The analyses in Section 3.3.3 are repeated with two-third of the years (1996-1997, 1999-2000...2014-2015) as the training period and one-third of the years (1998, 2001...2013) as the validation period. MELT and ΔQ models are reconstructed using the validation period only. The modeled MELT and ΔQ are subsequently evaluated against the observed MELT and ΔQ over the training and validation periods, separately. The purpose is to test whether the models have consistent predictive skills in different years with different hydroclimatic conditions.

Table 3.B1 demonstrates that the arrangement seen in Table 3.2 is largely maintained in both training and validation periods. For instance, in NW and WUS, the R^2 for both training and validation periods show peak associations in May. Of course, some differences exist, as no two or more water years have the exact same hydroclimatic condition. For

example, in SW, this remains true only for the training period, as the peak R^2 shifts to April for the validation period. Nevertheless, the magnitudes of R^2 in both training and validation periods are comparable, demonstrating that the model has a reasonably consistent predictive skill.

A similar conclusion can be drawn from the ΔQ case (Table 3.B2), and from when the analyses are conducted for dry-year and wet-year subsets (not shown).

Table 3.B1.

Same as Table 3.2, except for when the training and validation periods are treated separately

Month	NW		SW		WUS	
	Training	Validation	Training	Validation	Training	Validation
Feb	11	4	8	4	10	4
Mar	11	5	11	13	11	7
Apr	14	25	17	23	15	24
May	25	35	22	26	24	33
Jun	25	22	25	9	25	19
Jul	26	35	6	6	25	32

Note. The training period consists of 1996-1997, 1999-2000...2014-2015, and the validation period consists of 1998, 2001...2013.

Table 3.B2.

Same as Table 3.4, except for when the training and validation periods are treated separately

Month	NW		SW		WUS	
	Training	Validation	Training	Validation	Training	Validation
Feb	9	7	9	5	9	6
Mar	6	4	10	5	8	5
Apr	5	12	9	13	6	13
May	7	9	7	6	7	8
Jun	7	6	9	4	8	5
Jul	10	6	7	4	9	5

Note. The training period consists of 1996-1997, 1999-2000...2014-2015, and the validation period consists of 1998, 2001...2013.

Appendix 3C: Asymmetry of cloudiness associations between dry years and wet years

Dry years and wet years are determined using October-July total PRISM precipitation (P) at each individual snow pillow and stream gauge. The dry-year and wet-year subsets are prescribed as those with the 10 lowest and 10 highest October-July cumulative P. Subsequently, separate regression models are derived for the dry and wet-year subsets.

From the observed data, dry years generally exhibit larger CC-MELT association (R^2), but they undergo an earlier seasonal fall-off, reflecting shorter springtime and earlier summer, particularly in the SW. This contrast is most clearly depicted by June maps in Figure 3.C1 and by Table 3.C1, showing statistically significant negative correlations throughout the WUS in wet years, but confined to the NW in dry years.

This difference between dry and wet CC-MELT regression results in June reflects the longer-lasting snow cover and snowmelt in wetter years. Moreover, wetter years are associated with higher precipitation and hence with greater cloudiness, where the proportion of shortwave input to snowmelt energy balance is reduced. Along with this pattern is a relatively weaker MELT response to CC than to T_{\max} and T_{\min} in wetter years (Supporting Information).

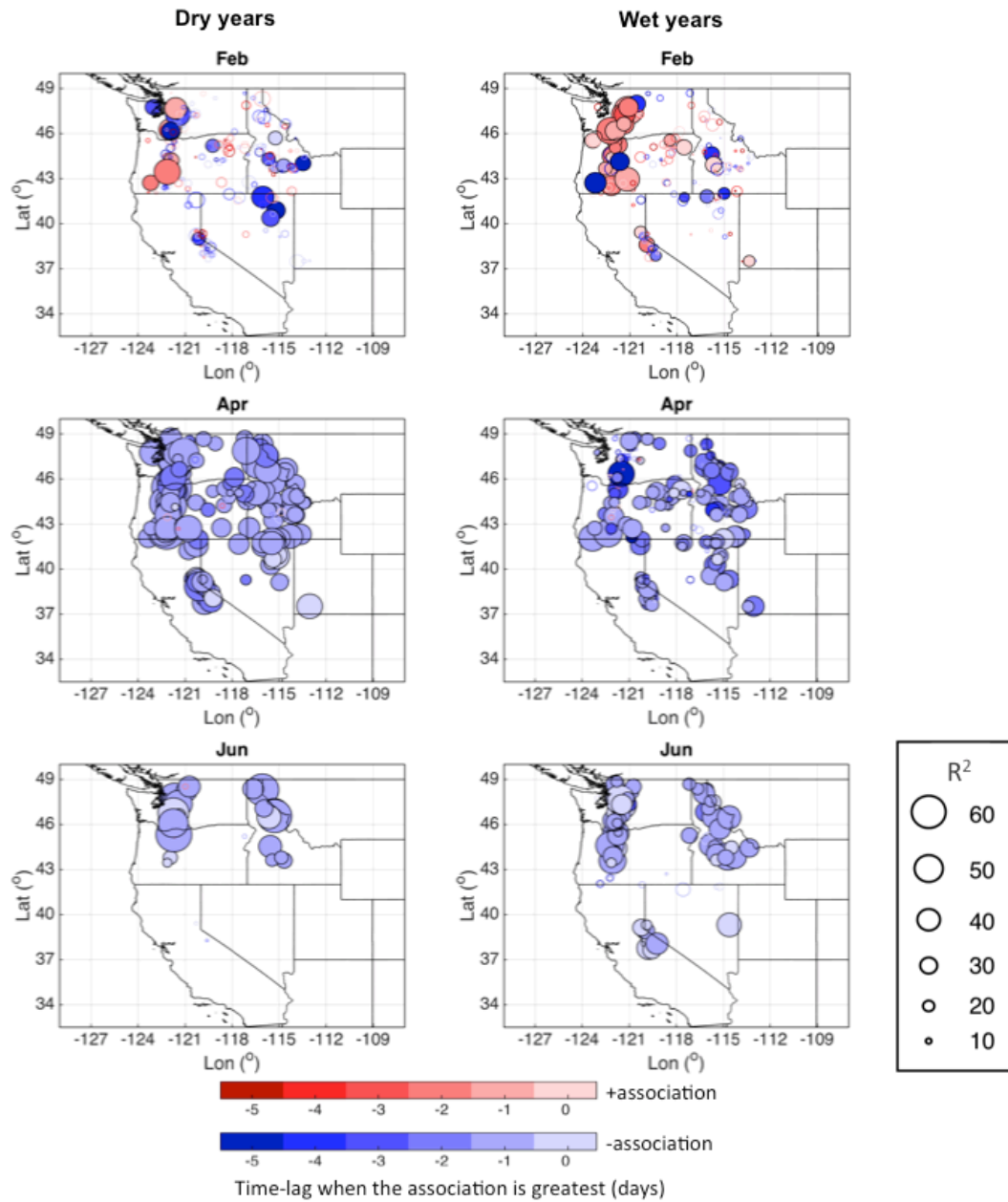


Figure 3.C1. Daily MELT variance explained by anomalous CC (%) for February, April and June during dry years (left) and wet years (right) of 1996-2015. Circle size is proportional to R^2 (%). Color tone denotes time lag of MELT relative to CC predictor whose regression coefficient has strongest magnitude, where red (blue) designates positive (negative) correlation. Sites with p -value < 0.01 are color-filled.

Table 3.C1.*Same as Table 3.2, except for the Dry-year and Wet-year Subsets*

Water Year	Month	NW	SW	WUS
Dry	Feb	11	12	12
	Mar	12	16	13
	Apr	27	26	27
	May	34	28	32
	Jun	33	10	31
	Jul	30	--	30
	Wet	Feb	15	10
Mar		12	12	12
Apr		15	16	16
May		27	22	26
Jun		25	21	24
Jul		22	7	10

The CC- Δ Q set shows the springtime progression in April, with most streams in SW exhibiting higher R^2 values in both subsets (Figure 3.C2 and Table 3.C2). Also, more streams in NW have negative correlations in the wet-year subset. The main difference from the CC-MELT set is that many locations exhibit strong positive CC- Δ Q correlation in June, marking the onset of summertime precipitation activities common in the mountains of western U.S. (Whiteman, 2000). However, in the dry-year subset, there are more sites with larger R^2 and positive correlations, especially in SW. This phenomenon is probably a symptom of a weaker snowmelt influence on streamflow fluctuations, owing to lower snowpack, and hence a stronger signal from rainfall and a drying effect from clear days that correlates positively to cloudiness.

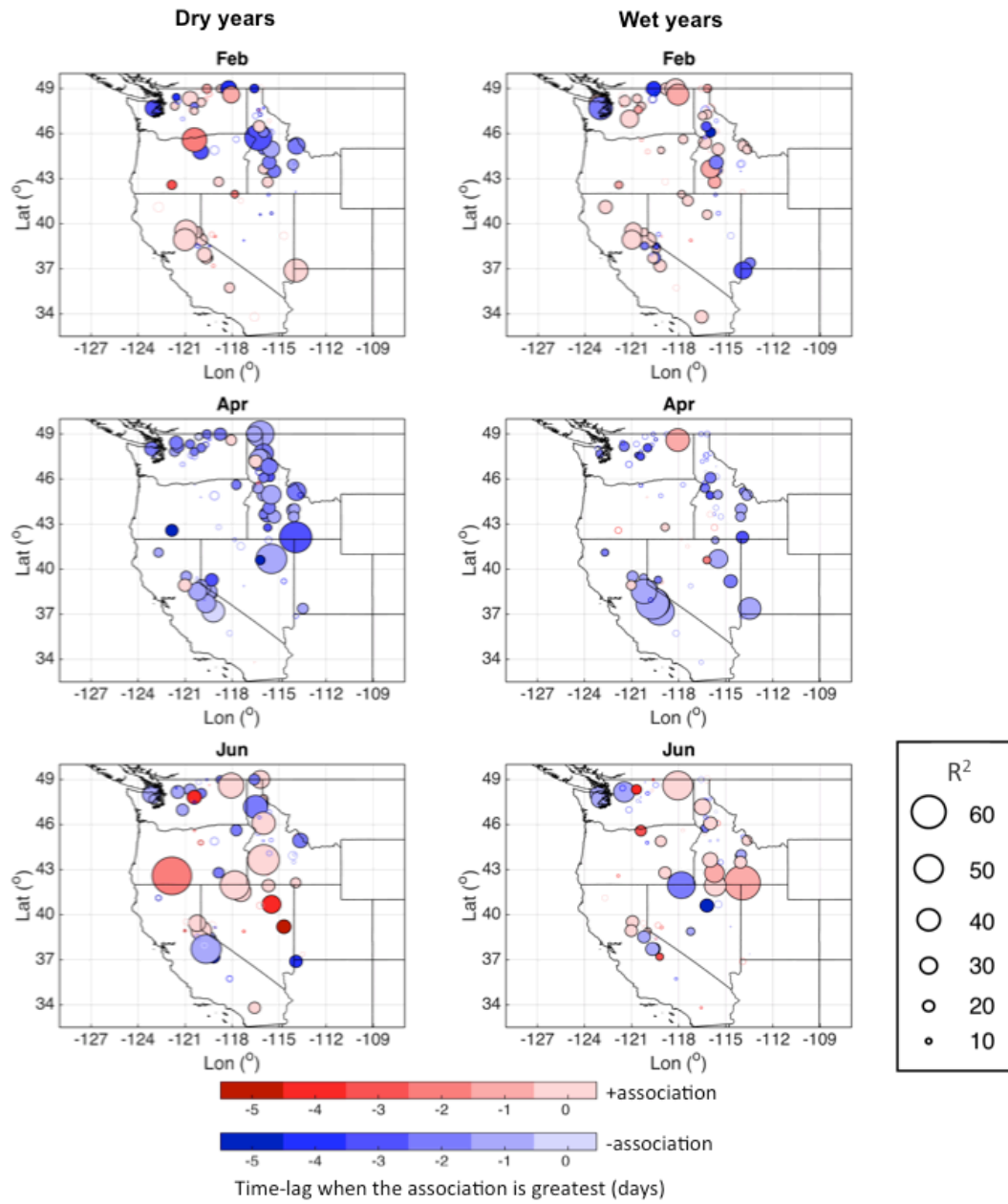


Figure 3.C2. Same as Figure 3.C1, except for ΔQ .

Table 3.C2.*Same as Table 3.4, except for the Dry-year and Wet-year Subsets*

Water Year	Month	NW	SW	WUS
Dry	Feb	10	9	10
	Mar	7	11	8
	Apr	11	11	11
	May	9	9	9
	Jun	10	13	11
	Jul	13	14	14
	Wet	Feb	10	10
Mar		7	10	8
Apr		7	13	9
May		9	9	9
Jun		8	8	8
Jul		12	8	11

References

Andreadis, K. M., Storck, P., & Lettenmaier, D. P. (2009). Modeling snow accumulation and ablation processes in forested environments. *Water Resources Research*, 45, W05429. doi:10.1029/2008WR007042.

Bair, E. H., Calfa, A. A., Rittger, K., & Dozier, J. (2018). Using machine learning for real-time estimates of snow water equivalent in the watersheds of Afghanistan. *The Cryosphere*, 12(5), 1579.

Bales, R. C., Molotch, N. P., Painter, T. H., Dettinger, M. D., Rice, R., & Dozier, J. (2006). Mountain hydrology of the western United States. *Water Resources Research*, 42(8).

Barnett, T. P., Adam, J. C., & Lettenmaier, D. P. (2005). Potential impacts of a warming climate on water availability in snow-dominated regions. *Nature*, 438, 303–9.

Barnett, T. P., Pierce, D. W., Hidalgo, H., Bonfils, C., Santer, B., Das, T., Bala, G., Wood, A., Nozawa, T., Mirin, A., Cayan, D., & Dettinger, M. (2008). Human-induced changes in the hydrology of the western United States. *Science*, 316, 1080-1083.

Barnhart, T. B., Molotch, N. P., Livneh, B., Harpold, A. A., Knowles, J. F., & Schneider, D. (2016). Snowmelt rate dictates streamflow. *Geophysical Research Letter*, 43, doi:10.1002/2016GL069690.

Boike, J., Roth, K., & Ippisch, O. (2003). Seasonal snow cover on frozen ground: Energy balance calculations of a permafrost site near Ny-Ålesund, Spitsbergen. *Journal of Geophysical Research*, 108(D2), 8163. doi:10.1029/2001JD000939.

California Department of Water Resources (2017, September). What a Difference a Year Makes. *Water Year 2017: What a Difference a Year Makes*.

- Cano, D., Monget, J. M., Albuissou, M., Guillard, H., Regas, N., & Wald, L. (1986). A method for the determination of the global solar radiation from meteorological satellite data. *Solar Energy*, 37, 31-39.
- Cayan, D. R., Kammerdiener, S., Dettinger, M. D., Caprio, J. M., & Peterson, D. H. (2001). Changes in the onset of spring in the western United States. *Bulletin of American Meteorological Society*, 82(3), 399-415.
- Cline, D. W. (1997). Snow surface energy exchanges and snowmelt at a continental, midlatitude Alpine site. *Water Resources Research*, 33(4), 689-701.
- Comola, F., Schaeffli, B., Da Ronco, P., Botter, G., Bavay, M., Rinaldo, A., & Lehning, M. (2015). Scale-dependent effects of solar radiation patterns on the snow-dominated hydrologic response. *Geophysical Research Letter*, 42. doi:10.1002/2015GL064075.
- Daly, C. (2013). Descriptions of PRISM spatial climate datasets for the conterminous United States. PRISM Doc., 14 pp. (Available online at http://www.prism.oregonstate.edu/documents/PRISM_datasets_aug2013.pdf.)
- Daly, C., Neilson, R. P., & Phillips, D. L. (1994). A statistical-topographic model for mapping climatological precipitation over mountainous terrain. *Journal of Applied Meteorology and Climatology*, 33, 140-158. doi:10.1175/1520-0450(1994)033<0140:ASTMFM.2.0.CO;2.
- Daly, C., Halblieb, M., Smith, J. I., Gibson, W. P., Doggett, M. K., Taylor, G. H., Curtis, J., & Pasteris, P. P. (2008). Physiographically sensitive mapping of climatological temperature and precipitation across the conterminous United States. *Int. J. Climatol.*, 28, 2031-2064. doi:10.1002/joc.1688.
- Dettinger, M. D., & Cayan, D. R. (1995). Large-scale atmospheric forcing of recent trends toward early snowmelt runoff in California. *Journal of Climate*, 8, 606-623.
- Diaz, H. F., & Eischeid, J. K. (2007). Disappearing “alpine tundra” Köppen climatic type in the western United States. *Geophysical Research Letter*, 34(18).
- Dickerson-Lange, S. E., Gersonde, R. F., Hubbart, J. A., Link, T. E., Nolin, A. W., Perry, G. H., Roth, T. R., Wayand, N. E., & Lundquist, J. D. (2017). Snow disappearance timing is dominated by forest effects on snow accumulation in warm winter climates of the Pacific Northwest, USA. *Hydrological Processes*, 31, 1846-1862. <https://doi.org/10.1002/hyp.11144>
- Dingman, S. L. (1994). *Physical Hydrology*, 575 pp., Prentice-Hall, Old Tappan, N. J.
- Fisher, R. A. (1925). *Statistical methods for research workers*, Genesis Publishing Pvt Ltd.
- Fosu, B. O., Simon Wang, S., & Yoon, J. (2016). The 2014/15 Snowpack Drought in Washington State and its Climate Forcing. *Bulletin of American Meteorological Society*, 97, S19-S24. <https://doi.org/10.1175/BAMS-D-16-0154.1>

- Garvelmann, J., Pohl, S., & Weiler, M. (2014). Variability of Observed Energy Fluxes during ROS and Clear Sky Snowmelt in a Midlatitude Mountain Environment. *Journal of Hydrometeorology*, *15*, 1220–1237. doi: <http://dx.doi.org/10.1175/JHM-D-13-0187.1>
- Garvelmann, J., Pohl, S., & Weiler, M. (2015). Spatio-temporal controls of snowmelt and runoff generation during rain-on-snow events in a mid-latitude mountain catchment. *Hydrological Processes*, *29*, 3649–3664. DOI:10.1002/hyp.10460
- Gautier, C., Diak, G., & Masse, S. (1980). A Simple Physical Model to Estimate Incident Solar Radiation at the Surface from GOES Satellite Data. *Journal of Applied Meteorology and Climatology*, *19*, 1005–1012. doi: [http://dx.doi.org/10.1175/1520-0450\(1980\)019<1005:ASPMTE>2.0.CO;2](http://dx.doi.org/10.1175/1520-0450(1980)019<1005:ASPMTE>2.0.CO;2).
- Gleason, K. E., Nolin, A. W., & Roth, T. R. (2017). Developing a representative snow-monitoring network in a forested mountain watershed. *Hydrology and Earth System Sciences*, *21*, 1137-1147. doi:10.5194/hess-21-1137-2017.
- Grillone, G., Agnese, C., & D'Asaro, F. (2012). Estimation of daily solar radiation from measured air temperature extremes in the mid-Mediterranean area. *Journal of Irrigation and Drainage Engineering*, *138*(10), 939-947.
- Henn, B., Clark, M. P., Kavetski, D., & Lundquist, J. D. (2015). Estimating mountain basin-mean precipitation from streamflow using Bayesian inference. *Water Resources Research*, *51*, 8012– 8033. doi:10.1002/2014WR016736.
- Hidalgo, H. G., Cayan, D. R., & Dettinger, M. D. (2005). Sources of Variability of Evapotranspiration in California. *J. Hydrometeor.*, *6*, 3–19. <https://doi.org/10.1175/JHM-398.1>.
- Hinkelman, L. M., Lapo, K. E., Cristea, N. C., & Lundquist, J. D. (2015). Using CERES SYN surface irradiance data as forcing for snowmelt simulation in complex terrain. *Journal of Hydrometeorology*, *16*, 2133–2152. doi:10.1175/JHM-D-14-0179.1.
- Hoerling, M. P., Dettinger, M., Wolter, K., Lukas, J., Eischeid, J., Nemani, R., Liebmann, B., & Kunkel, K. E. (2013). Present weather and climate: Evolving conditions, in *Assessment of Climate Change in the Southwest United States: A Report Prepared for the National Climate Assessment*, edited by G. Garfin et al., pp. 74–100, A report by the Southwest Climate Alliance, Isl. Press, Washington, D. C.
- Howell, D. C. (2011). Chi-square test: analysis of contingency tables, 250-252 pp., *International Encyclopedia of Statistical Science*, Springer Berlin Heidelberg.
- Ineichen, P., & Perez, R. (1999). Derivation of cloud index from geostationary satellites and application to the production of solar irradiance and daylight illuminance data. *Theor. Appl. Climatol.*, *64*, 119–130.
- IPCC (2013). *Climate Change 2013: The Physical Science Basis*, Contribution of Working Group I to the Fifth Assessment Report of the Intergovernmental Panel on Climate Change (Stocker, T.F., D. Qin, G.-K. Plattner, M. Tignor, S.K. Allen, J. Boschung, A. Nauels, Y.

Xia, V. Bex and P.M. Midgley (eds.), 1535 pp., Cambridge Univ. Press, Cambridge, United Kingdom and New York, NY, USA.

Kapnick, S., & Hall, A. (2012). Causes of recent changes in western North American snowpack. *Clim. Dyn.*, *38*, 1885-99.

Karl, T. R., & Riebsame, W. E. (1989). The impact of decadal fluctuations in mean precipitation and temperature on runoff: A sensitivity study over the United States. *Clim. Change*, *15*, 423–447.

Karl, T. R., & Koss, W. J. (1984). *Regional and National Monthly, Seasonal, and Annual Temperature Weighted by Area, 1895-1983*, in *Hist. Climatol. Ser. 4-3*, pp. 38, Natl. Clim. Data Cent., Asheville, NC.

Lapo, K. E., Hinkelman, L. M., Landry, C. C., Massmann, A. K., & Lundquist, J. D. (2015a). A simple algorithm for identifying periods of snow accumulation on a radiometer. *Water Resources Research*, *51*, 7820–7828. doi:10.1002/2015WR017590.

Lapo, K. E., Hinkelman, L. M., Raleigh, M. S., & Lundquist, J. D. (2015b). Impact of errors in the downwelling irradiances on simulations of snow water equivalent, snow surface temperature, and the snow energy balance. *Water Resources Research*, *51*, 1649–1670. doi:10.1002/2014WR016259.

Lettenmaier, D. P. (2017). Observational breakthroughs lead the way to improved hydrological predictions. *Water Resources Research*, *53*, 2591–2597. doi:10.1002/2017WR020896.

Li, D., Wrzesien, M. L., Durand, M., Adam, J., and Lettenmaier, D. P. (2017). How much runoff originates as snow in the western United States, and how will that change in the future?. *Geophys. Res. Lett.*, *44*(12), 6163-6172. doi:10.1002/2017GL073551.

Luce, C. H., Lopez-Burgos, V., & Holden, Z. (2014). Sensitivity of snowpack storage to precipitation and temperature using spatial and temporal analog models. *Water Resources Research*, *50*, 9447–9462. doi:10.1002/2013WR014844.

Lundquist, J. D., & Flint, A. F. (2006). Onset of Snowmelt and Streamflow in 2004 in the Western United States: How Shading May Affect Spring Streamflow Timing in a Warmer World. *Journal of Hydrometeorology*, *7*, 1199–1217. doi: <http://dx.doi.org/10.1175/JHM539.1>

Lundquist, J. D., & Cayan, D. R. (2002). Seasonal and spatial patterns in diurnal cycles in streamflow in the western United States. *J. Hydrometeorology*, *3*(5), 591-603.

Lundquist, J. D., Dettinger, M. D., & Cayan, D. R. (2005). Snow-fed streamflow timing at different basin scales: Case study of the Tuolumne River above Hetch Hetchy, Yosemite, California. *Water Resources Research*, *41*, W07005. doi:10.1029/2004WR003933

Lundquist, J. D., Dettinger, M. D., Stewart, I. T., & Cayan, D. R. (2009). Variability and trends in spring runoff in the western United States. *Climate warming in western North*

America: evidence and environmental effects. University of Utah Press, Salt Lake City, Utah, USA, 63-76.

Lundquist, J. D., Wayand, N. E., Massmann, A., Clark, M. P., Lott, F., & Cristea, N. C. (2015). Diagnosis of insidious data disasters. *Water Resources Research*, *51*, 3815–3827. doi:10.1002/2014WR016585.

Lundquist, J. D., Dickerson-Lange, S. E., Lutz, J. A., & Cristea, N. C. (2013). Lower forest density enhances snow retention in regions with warmer winters: A global framework developed from plot-scale observations and modeling. *Water Resources Research*, *49*(10), 6356-6370.

Mann, M. E., & Gleick, P. H. (2015). Climate change and California drought in the 21st century. *Proceedings of the National Academy of Sciences of the United States of America*, *112*(13), 3858–3859. doi:10.1073/pnas.1503667112.

Mao, Y., Nijssen, B., & Lettenmaier, D. P. (2015). Is climate change implicated in the 2013–2014 California drought? A hydrologic perspective. *Geophysical Research Letter*, *42*, 2805–2813. doi: 10.1002/2015GL063456.

Marks, D., & Dozier, J. (1992). Climate and energy exchange at the snow surface in the alpine region of the Sierra Nevada: 2. Snow cover energy balance. *Water Resources Research*, *28*(11), 3043-3054.

McCabe, G. J., Hay, L. E., & Clark, M. P. (2007). ROS Events in the Western United States. *Bulletin of American Meteorological Society*, *88*, 319–328. doi: <http://dx.doi.org/10.1175/BAMS-88-3-319>.

McCabe, G. J., & Wolock, D. M. (2011). Independent effects of temperature and precipitation on modeled runoff in the conterminous United States. *Water Resources Research*, *47*, W11522. doi:10.1029/2011WR010630.

Meyer, J. D. D., Jin, J., & Wang, S.-Y. (2012). Systematic patterns of the inconsistency between snow water equivalent and accumulated precipitation as reported by the Snowpack Telemetry Network. *Journal of Hydrometeorology*, *13*, 1970–1976.

Mote, P. W. (2003). Trends in snow water equivalent in the Pacific Northwest and their climatic causes. *Geophysical Research Letter*, *30*, 1601. doi:10.1029/2003GL017258

Mote, P. W. (2006). Climate-driven variability and trends in mountain snowpack in western North America. *Journal of Climate*, *19*, 6209–6220.

Mote, P. W., Hamlet, A. F., & Salathe, E. (2008). Has spring snowpack declined in the Washington Cascades?. *Hydrology and Earth System Sciences*, *12*, 193–206.

Mote, P. W., Hamlet, A. F., Clark, M. P., & Lettenmaier, D. P. (2005). Declining mountain snowpack in western North America. *Bulletin of American Meteorological Society*, *86*, 39-49.

- Mote, P. W., Rupp, D. E. Li, S., Sharp, D. J., Otto, F., Uhe, P. F., Xiao, M., Lettenmaier, D. P., Cullen, H., & Allen, M. R., (2016). Perspectives on the causes of exceptionally low 2015 snowpack in the western United States. *Geophysical Research Letters*, *43*, 10980-10988. doi: 10.1002/2016GL069965.
- Musselman, K. N., Clark, M. P., Liu, C., Ikeda, K., & Rasmussen, R. (2017). Slower snowmelt in a warmer world. *Nature Climate Change*. doi: 10.1038/NCLIMATE3225
- Mutzner, R., Weijs, S. V., Tarolli, P., Calaf, M., Oldroyd, H. J., & Parlange, M. B. (2015). Controls on the diurnal streamflow cycles in two subbasins of an alpine headwater catchment. *Water Resources Research*, *51*, 3403–3418. doi:10.1002/2014WR016581.
- Nowak, K., Hoerling, M., Rajagopalan, B., & Zagona, E. (2012). Colorado River basin hydroclimatic variability. *Journal of Climate*, *25*, 4389–4403.
- Null, S. E., Viers, J. H., Deas, M. L., Tanaka, S. K., & Mount, J. F. (2013). Stream temperature sensitivity to climate warming in California’s Sierra Nevada: impacts to coldwater habitat. *Climatic Change*, *116*(1), 149-170.
- Paech, S. J., Mecikalski, J. R., Sumner, D. M., Pathak, C. S., Wu, Q., Islam, S., & Sangoyomi T., (2009). A calibrated, high resolution GOES satellite solar insolation product for a climatology of Florida evapotranspiration. *Journal of the American Water Resources Association*, *45*(6), 1328–1342.
- Pearson, K. (1904). On the theory of contingency and its relation to association and normal correlation; On the general theory of skew correlation and non-linear regression. *Cambridge Univ. Press*.
- Perez, R., Ineichen, P., Moore, K., Kmiecik, M., Chain, C., George, R., & Vignola, F. (2002). A new operational model for satellite-derived irradiances: description and validation. *Solar Energy*, *73*, 307-317.
- Pierce, D. W., Barnett, T. P., Hidalgo, H. G., Das, T., Bonfils, C., Santer, B. D., Bala, G., Dettinger, M. D., Cayan, D. R., Mirin, A., Wood, A. W., & Nozawa, T. (2008). Attribution of Declining Western U.S. Snowpack to Human Effects. *Journal of Climate*, *21*, 6425-6444. doi:10.1175/2008JCLI2405.1
- PRISM Climate Group, Oregon State University, <http://prism.oregonstate.edu>, created 29 Apr 2016.
- Raleigh, M. S., Livneh, B., Lapo, K., & Lundquist, J. D. (2016). How does availability of meteorological forcing data impact physically-based snowpack simulations?. *Journal of Hydrometeorology*, *17*(1), 99–120. doi:10.1175/JHM-D-14-0235.1.
- Raleigh, M. S., Rittger, K., Moore, C. E., Henn, B., Lutz, J. A., and Lundquist, J. D. (2013). Ground-based testing of MODIS fractional snow cover in subalpine meadows and forests of the Sierra Nevada. *Remote Sens. Environ.*, *128*, 44-57. doi:10.1016/j.rse.2012.09.016.
- Ralph, F. M., Hecht, C., & Kawzenuk, B. (2017, April 6). *How Many Atmospheric Rivers Have Hit the U.S. West Coast During the Remarkably Wet Water Year 2017?*. Retrieved

from <http://cw3e.ucsd.edu/how-many-atmospheric-rivers-have-hit-the-u-s-west-coast-during-the-remarkably-wet-water-year-2017/>

Regonda, S. K., Rajagopalan, B., Clark, M. & Pitlick, J. (2005). Seasonal cycle shifts in hydroclimatology over the western United States. *Journal of Climate*, *18*, 372–384.

Rheinheimer, D. E., Bales, R. C., Oroza, C. A., Lund, J. R., & Viers, J. H. (2016). Valuing year-to-go hydrologic forecast improvements for a peaking hydropower system in the Sierra Nevada. *Water Resources Research*, *52*, 3815–3828. doi:10.1002/2015WR018295.

Rice, R., Bales, R. C., Painter, T. H., & Dozier, J. (2011). Snow water equivalent along elevation gradients in the Merced and Tuolumne River basins of the Sierra Nevada. *Water Resour. Res.*, *47*, W08515. doi:10.1029/2010WR009278.

Rittger, K., Bair, E. H., Kahl, A., and Dozier, J. (2016). Spatial estimates of snow water equivalent from reconstruction. *Adv. Water Resour.*, *94*, 345-363. doi:10.1016/j.advwatres.2016.05.015.

Serreze, M. C., Clark, M. P., Armstrong, R. L., McGinnis, D. A., & Pulwarty, R. S. (1999). Characteristics of the western United States snowpack from snowpack telemetry (SNOTEL) data. *Water Resources Research*, *35*(7), 2145-2160.

Shukla, S., Safeeq, M., AghaKouchak, A., Guan, K., & Funk, C. (2015). Temperature impacts on the water year 2014 drought in California. *Geophysical Research Letter*, *42*, 4384–4393. doi:10.1002/2015GL063666.

Simpson, J. J., Dettinger, M. D., Gehrke, F., McIntire, T. J., & Hufford, G. L. (2004). Hydrologic scales, cloud variability, remote sensing, and models: Implications for forecasting snowmelt and streamflow. *Weather and forecasting*, *19*(2), 251-276.

Slack, J. R., & Landwehr, J. M. (1992). Hydro-Climatic Data network (HCDN): A U.S. Geological Survey streamflow data set for the United States for the study of climate variations, 1874–1988. U.S. Geological Survey Open-File Rep. 92-129, 193 pp.

Slater, A. G. (2015). Surface Solar Radiation in North America: A Comparison of Observations, Reanalyses, Satellite and Derived Products. *J. Hydrometeorol.*, *17*(1), 401-420. doi:10.1175/JHM-D-15-0087.1.

Sproles, E. A., Roth, T. R., & Nolin, A. W. (2017). Future snow? A spatial-probabilistic assessment of the extraordinarily low snowpacks of 2014 and 2015 in the Oregon Cascades. *The Cryosphere*, *11*, 331-341. doi:10.5194/tc-11-331-2017.

Stewart, I., Cayan, D. R., & Dettinger, M. D. (2004). Changes in snowmelt runoff timing in western North America under a ‘Business as Usual’ climate change scenario. *Climatic Change*, *62*(1), 217-232.

Stewart, I. T., Cayan, D. R., & Dettinger, M. D. (2005). Changes towards earlier streamflow timing across western North America. *Journal of Climate*, *18*, 1136-1155.

- Stoelinga, M. T., Albright, M. D., & Mass, C. F. (2009). A new look at snowpack trends in the Cascade Mountains. *Journal of Climate*, *23*(10), 2473–2491. doi:10.1175/JCLI3321.1.
- Stone, R. S. (1997). Variations in western Arctic temperatures in response to cloud- radiative and synoptic-scale influences. *Journal of Geophysical Research*, *102*(D18), 21,769 – 21,776.
- Stone, R. S., Dutton, E. G., Harris, J. M., & Longenecker, D. (2002). Earlier spring snowmelt in northern Alaska as an indicator of climate change. *Journal of Geophysical Research*, *107*(D10), 4089. doi:10.1029/2000JD000286.
- Sumargo, E., & Cayan, D. R. (2017). Variability of cloudiness over mountain terrain in the Western United States. *Journal of Hydrometeorology*, *18*, 1227–1245. <https://doi.org/10.1175/JHM-D-16-0194.1>.
- Sumargo, E., & Cayan, D. R. (2018). Data from: The Influence of Cloudiness on Hydrologic Fluctuations in the Mountains of the Western United States. UC San Diego Library Digital Collections. Dataset. <https://doi.org/10.6075/J0PC30K6>.
- Swain, D. L., Langenbrunner, B., Neelin, J. D., & Hall, A. (2018). Increasing precipitation volatility in twenty-first-century California. *Nature Climate Change*, *1*.
- Tennant, C. J., Harpold, A. A., Lohse, K. A., Godsey, S. E., Crosby, B. T., Larsen, L. G., Brooks, P. D., Van Kirk, R. W., & Glenn, N. F. (2017). Regional sensitivities of seasonal snowpack to elevation, aspect, and vegetation cover in western North America. *Water Resources Research*, *53*, doi:10.1002/2016WR019374.
- Trujillo, E., & Molotch, N. P. (2014). Snowpack regimes of the Western United States. *Water Resour. Res.*, *50*, 5611–5623. doi:10.1002/ 2013WR014753.
- Whiteman, C. D. (2000). *Mountain Meteorology: Fundamentals and Applications*, 355 pp., Oxford Univ. Press, New York.
- Williams, A. P., Seager, R., Abatzoglou, J. T., Cook, B. I., Smerdon, J. E., & Cook, E. R. (2015). Contribution of anthropogenic warming to California drought during 2012–2014. *Geophysical Research Letter*, *42*, 6819–6828. doi:10.1002/2015GL064924.
- Woodhouse, C. A., Pederson, G. T., Morino, K., McAfee, S. A., & McCabe, G. J. (2016). Increasing influence of air temperature on upper Colorado River streamflow. *Geophysical Research Letter*, *43*, 2174–2181. doi:10.1002/2015GL067613.
- Würzer, S., Jonas, T., Wever, N., & Lehning, M. (2016). Influence of initial snowpack properties on runoff formation during rain-on-snow events. *Journal of Hydrometeorology*, *17*(6) 1801-1815. doi:10.1175/JHM-D-15-0181.1.
- Zelenka, A., Perez, R., Seals, R., & Renne, D. (1999). Effective accuracy of satellite-derived hourly irradiances. *Theoretical and Applied Climatology*, *62*, 199-207.
- Zhang, T., Stamnes, K., & Bowling, S. A. (1996). Impact of clouds on surface radiative fluxes and snowmelt in the Arctic and Subarctic. *Journal of Climate*, *9*, 2110–2123.

Chapter 4

Effects of Cloud Variability on Snow-fed Runoffs in California's Sierra Nevada

We investigate how runoff responds to varying cloudiness by comparing runoffs in two neighboring watersheds, the upper Tuolumne River and upper Merced River watersheds in California's Sierra Nevada. Daily cloud cover indices (CC) from the Geostationary Operational Environmental Satellite are used to derive daily solar irradiance input in the Precipitation-Runoff Modeling System, from which the Baseline simulation is generated. We then conduct three experiments: 1) removing daily CC fluctuations under which every day has climatological cloud cover, 2) removing CC at different (high, mid, low) elevation bands, and 3) amplifying daily CC fluctuations. Each experiment is then compared to the baseline simulation to isolate the influence of daily CC variability on runoff, to reveal the relative importance of CC at different elevation bands, and to understand the runoff sensitivity to intensified daily CC fluctuations, respectively. Overall, the influence of cloudiness on the seasonal runoff is greater on the runoff timing than on the runoff volume. Variability of daily CC moderates the seasonal runoff, characterized by higher flows in the early and late snowmelt season and lower flows in the mid snowmelt season. In the first experiment, we find the baseline simulation produces 1-3 days earlier spring onsets. From the second experiment, we find higher elevation fluctuating CC exerts a greater influence on the runoff than lower elevation fluctuating CC does. Across all elevation bands, the baseline simulation produces 2-15 days later spring onsets. From the third experiment, we find a greater runoff response to the "relatively cloudy-sky periods get cloudier" scheme than to the "relatively

clear-sky periods get clearer” scheme, with the former producing 3-5 days later spring onsets than the baseline simulation.

4.1 Introduction

Cloud cover variability is the principal regulator of incoming solar radiation, or short wave flux (SWF) at the surface (Harrison et al., 1990; Simpson et al., 2004). In a mountainous region like the western United States (U.S.), SWF is the primary input to snowmelt energy balance (Marks and Dozier, 1992; Cline, 1997; Bales et al., 2006; Comola et al., 2015; Painter et al., 2017). Consequently, understanding cloud cover variability is essential for hydrologic applications in mountainous catchments and their downstream ecosystem and societies, such as irrigation, water supply, hydropower generation and environmental services (Viviroli et al., 2011).

California’s highly seasonal Mediterranean climate and its setting in the lower edge of the North Pacific winter storm track exposes the Sierra Nevada mountain range to considerable fluctuations in winter and spring cloudiness (Sumargo and Cayan, 2017), precipitation and runoff (Lundquist et al., 2005; Cayan et al., 2016) variabilities in California. The exceptionally wet water year (WY; defined as the year running from October to September) 2017, marked by high mountain snowpack (California Department of Water Resources, 2017; Lettenmaier, 2017) and frequent Atmospheric River events (Ralph et al., 2017), following the multiyear severe drought occurring in WYs 2012-2015 (Mao et al., 2015; Seager et al., 2015; Williams et al., 2015) exemplify these variabilities.

Over the mountain regions like the Sierra Nevada, winter precipitation is strongly influenced by the orographic effect (Dettinger et al., 2004; Lundquist et al., 2010) and arrives

mostly as snowfall that is subsequently stored as seasonal snowpack (Dettinger et al., 2011). The snowpack sporadically melts and feeds into the streams throughout the spring and summer, providing water for 60%-75% of California's agricultures and cities (Rosenthal and Dozier, 1996; Downing, 2015). During the snowmelt season, cloudiness variability is a major regulator of snowmelt variations, accounting for ~10%-40% of snowmelt variations over the peak months in the Sierra Nevada (Sumargo and Cayan, 2018). For this reason, this study emphasizes the spring-summer period when cloudiness-snowmelt-runoff processes are most active.

However, unlike surface hydrologic response to precipitation and temperature (e.g., Karl and Riebsame, 1989; Mote, 2006; Stoelinga et al., 2009; McCabe and Wolock, 2011; Nowak et al., 2012; Luce et al., 2014; Woodhouse et al., 2016; Sproles et al., 2017), the response to cloudiness variability over montane watersheds has not been thoroughly studied.

The significance of this study is heightened with climate change, since many hydrologic applications rely on historical statistics, which will become less reliable as climate continues to change (Lundquist et al., 2009; Rice et al., 2011). For instance, storm tracks, cloud cover patterns (Yin, 2005; Held and Soden, 2006; O'Gorman and Schneider, 2008; Dettinger, 2011) and radiative properties (Zelinka et al., 2017) are expected to evolve with climate change. The warming trend has resulted in greater rain-to-snow ratio (Knowles et al., 2006), changes in winter precipitation, seasonal snowpack and annual flow (Hantel and Hirtl-Wielke, 2007; Schöner et al., 2009; Beniston, 2010, Das et al., 2011), and earlier streamflow timing (Stewart et al., 2005; Horton et al., 2006; Morán-Tejeda et al., 2014). It is also projected to decrease the snowmelt rate (Musselman et al., 2017) and summer soil moisture (Gergel et al., 2017). These factors will inevitably complicate the association

between cloudiness variability and surface hydrologic variations, especially in mountain environment where surface energy balance and hydroclimatic processes are inherently complex (Brauchli et al., 2017).

The geographic foci in this study are two neighboring watersheds, i.e., the Tuolumne River and the Merced River watersheds on the west-central slope of California's Sierra Nevada. The close proximity between the two watersheds allows a direct comparison of the surface hydrologic responses to cloudiness in the respective watersheds, owing to their similar climate. These watersheds are characterized by high elevations and cold fall-winter-spring conditions (Lundquist et al., 2016), which allow more snowfall vs. rainfall and the development of a substantial snowpack which persists into later spring or early summer.

Additionally, the steep terrain, shallow soils and abundant granodiorite rocks allow minimal losses of surface water to subsurface processes—often a major source of uncertainties in determining the water balance in many other watersheds (Lundquist et al., 2016). This characteristic makes the surface hydrology of both basins relatively straightforward (Slack and Landwehr, 1992; Jeton et al., 1996; Rice et al., 2011), thus enabling direct examinations of weather/climatic influence on the surface hydrology. Nevertheless, some differences should emerge since no two basins are identical. Therefore, the Tuolumne River and Merced River watersheds are suitable for this research.

In this paper, we use a hydrological model, driven by observed and idealized meteorological inputs, to explore how runoffs in the Tuolumne River and Merced River catchments respond to different forms of cloudiness variation. To investigate different types of cloudiness effects, we conduct a series of experiments with a recent version (see section 4.2.1) of Precipitation-Runoff Modeling System (PRMS) (Leavesley et al., 1983; Markstrom

et al., 2015) as our primary tool. We also examine how this response varies with elevation, since the elevation of these watersheds covers a wide range where cloudiness, rainfall and snowfall vary considerably (Dettinger et al., 2004; Simpson et al., 2004), as does the sensitivity to climate variation of snowmelt and other processes (Rice et al., 2011). Finally, motivated by the projected increase in static stability (Frierson, 2006) and by projected intensification of occasional extreme precipitation (Shi and Durran, 2016) over the midlatitudes, we investigate how runoff changes when the relatively clear-sky periods get clearer and the relatively cloudy-sky periods get cloudier.

4.2 Precipitation-Runoff Modeling System (PRMS)

4.2.1 Model description

The Precipitation-Runoff Modeling System (PRMS) is an operational, watershed-scale hydrologic model developed by the U.S. Geological Survey (Leavesley et al., 1983; Markstrom et al., 2015). The PRMS is a deterministic, distributed-parameter, physical-process-based model developed to evaluate watershed hydrologic responses to weather/climate and land use. The watershed is partitioned to segments called the Hydrologic Response Units (HRUs), which are based on the physical characteristics of the watershed, such as the surface elevation, slope and aspect, vegetation and soil types. The model requires daily maximum and minimum air temperatures, precipitation and solar radiation (optional) as inputs.

In this study, we use version 4.0.1 of the PRMS model. Specifically, we utilize the California Department of Water Resources (CDWR) PRMS modules of the Tuolumne and Merced River basins. The two models already have precipitation and temperature inputs

provided by the CDWR modeling team and have undergone calibrations by the modeling team at the CDWR. On the other hand, SWF inputs are not provided. The primary reason is SWF and, in fact, any weather measurement networks in mountainous watersheds tend to be sparse, owing to installation and maintenance problems related to the difficult access and snow-laden seasons (Dettinger, 2014; Henn et al., 2015; Lapo et al., 2015; Le Moine et al., 2015; Raleigh et al., 2016).

If not provided, SWF is estimated using degree-day method based on diurnal temperature range (DTR), which is a proxy for cloud cover, and clear-sky solar radiation (Leavesley et al., 1983). This simple method remains to be a standard practice in hydrologic modeling communities (Bohn et al., 2013). However, the relationship between DTR and cloud cover is not robust (Pellicciotti et al., 2011), and the estimated SWF may contain significant biases. Problems that arise from the DTR-based estimates are shown for example at the Dana Flat location at 2,987 m in the Tuolumne River watershed in Figure 4.1, which also shows that SWF estimates using Geostationary Operational Environmental Satellite (GOES) performs much better in replicating surface observations of SWF. For this reason, we explore the use of GOES observations of clouds to derive SWF (described in section 4.3.2) and demonstrate that this method brings significant improvements to SWF (Figure 4.1) and runoff (appendix 4C) estimates.

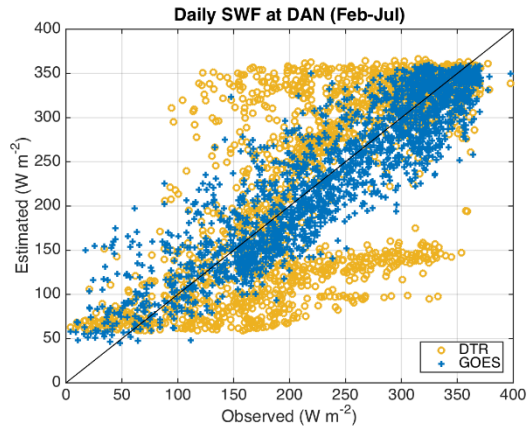


Figure 4.1. Observed vs. estimated daily SWF at Dana Meadows (DAN; 37.897 °N, 119.257 °W, 2,987 m) for snowmelt season (February-July) of 1996-2014. The observed SWF record is obtained from the California Data Exchange Center (<http://cdec.water.ca.gov/>) operated by the California Cooperative Snow Survey. The SWF estimates are derived using PRMS version of diurnal temperature range (DTR) algorithm and using Ineichen-Perez algorithm with using GOES α (GOES). The diagonal line is the 1:1 line.

If provided, the provided SWF, instead of the default SWF, is used as a forcing in the water balance and energy balance computations, including in snowmelt and potential evapotranspiration (PET) estimations. The snowmelt is principally a function of SWF and snow albedo, such that the amount of SWF applied to the snowpack is proportional to $1 - \text{albedo}$ (Markstrom et al., 2015). The snow albedo is a function of time where it decays with time as snowpack ages, computed using an empirical relationship developed by the U.S. Army Corps of Engineer (1956). (Note that the albedo does affect the longwave radiation from the atmosphere in PRMS.) The PRMS Tuolumne and Merced modules we employ estimate the PET using the Jensen-Haise formulation (Jensen and Haise, 1963; Jensen et al., 1969).

The PRMS Tuolumne River basin covers a larger basin area and represents the watershed as being distributed among 405 HRUs and 10 sub-basins, with a terminus downstream of Lagrange dam (TRLG; USGS gauge 11289650) (Figure 4.2, top left panel).

The model spans from WY 1969 to WY 2014 by default, but our simulations can only run from 1996 onward due to the availability of GOES data (described in section 4.3.2). The simulations are divided into two segments of approximately equal lengths: 1) training period (1996-2005) for calibration (appendix 4C), and 2) validation period (2006-2014) for evaluation.

The Hetch Hetchy Reservoir (HTH) affects flows over downstream areas. Therefore, the analysis is focused on sub-basins 1-3 above HTH, which altogether constitute the upper Tuolumne basin, with a terminus at HTH. Likewise, the sum of total runoff from sub-basins 1-3 is equivalent to the total inflow to HTH. The time series of the observed inflow to HTH is provided by the San Francisco Public Utilities Commission. The upper Tuolumne River basin consists of 161 HRUs, with HRU centroid elevations ranging from 1,152 m to 3,471 m, and averaging 2,621 m.

The PRMS Merced River basin has 659 HRUs and 3 sub-basins, with a terminus at Merced River below Merced Falls Dam (MRMF; USGS gauge 11270900) (Figure 4.2, top right panel). By default, the model runs from WY 1949 to WY 2013, but again, our simulations start from 1996 following the availability of GOES dataset. Like the Tuolumne module, the simulations are divided into: 1) training period (1996-2004) for calibration (appendix 4C), and 2) validation period (2005-2013) for evaluation.

Dams are also present in most parts of the basin, including in one of the upstream sub-basins (sub-basin 2). Only sub-basin 1 does not contain a dam, which has a terminus at Merced River at Pohono Bridge (POH; USGS gauge 11266500). This situation makes the calibration effort tricky, since calibrating the model on sub-basin 1 only would not account for flows from sub-basin 2, while including sub-basin 2 or calibrating on a whole-basin scale

would include dams' effects. We choose to focus the calibration and analyses on sub-basin 1 only, hereby called the upper Merced basin. The observed streamflow data from POH is provided by the CDWR modeling team. The upper Merced River basin consists of 298 HRUs, with HRU centroid elevations ranging from 1,198 m to 3,733 m, and averaging 2,494 m.

The Merced basin is adjacent to the Tuolumne basin, so the hydroclimates of both basins should be similar. To verify this similarity, the wavelet coherence between the inflow to HTH and streamflow at POH is computed using Aslak Grinsted's MATLAB[®] script (Grinsted et al., 2004; available on <http://www.glaciology.net/wavelet-coherence>). The result reveals close correspondence between the two variables at periods >7 days nearly across the entire WYs 1996-2013 (Figure 4.2, bottom panel), indicating both basins have nearly identical behaviors on weekly and longer time scales.

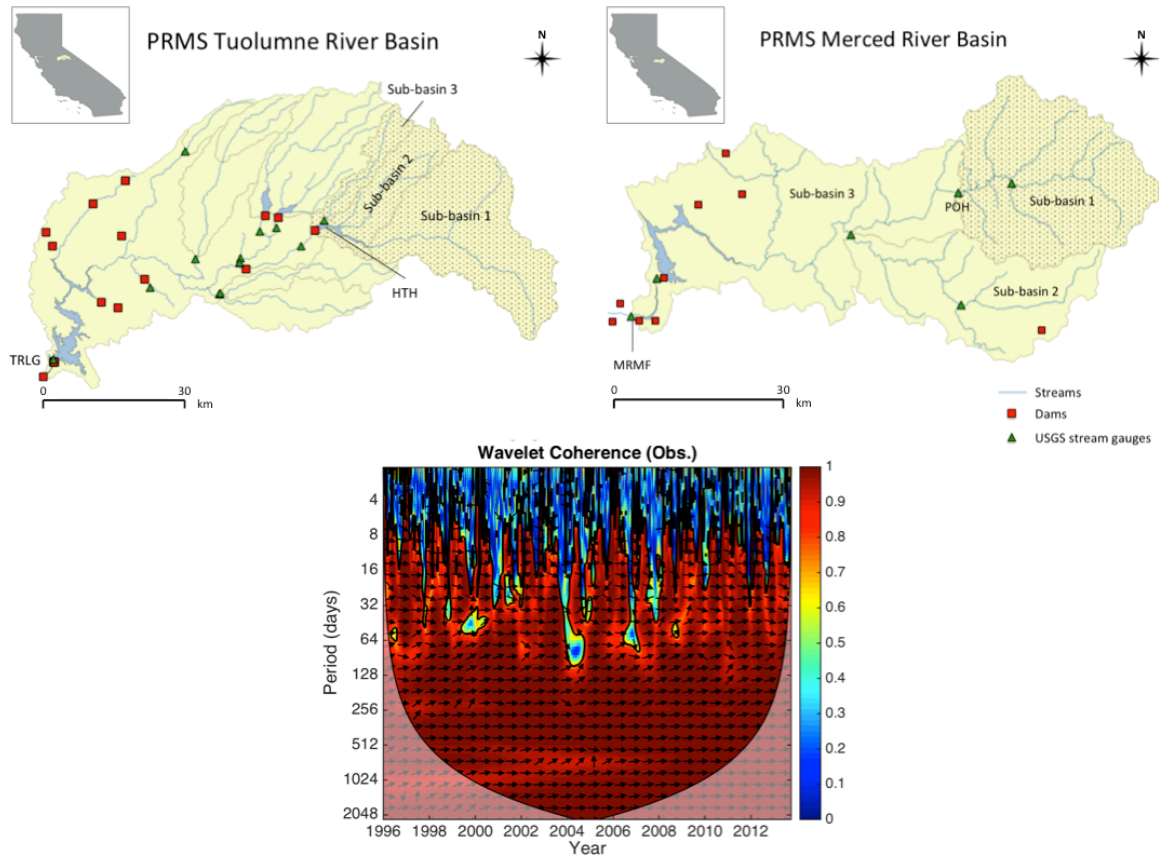


Figure 4.2. Top left: PRMS Tuolumne River basin, with a terminus at Tuolumne River below La Grange Dam (TRLG). The upper Tuolumne basin is hatched, with a terminus at Hetch Hetchy Reservoir (HTH). Top right: PRMS Merced River basin, with a terminus at Merced River at Merced Falls (MRMF). The upper Merced basin is hatched, with a terminus at Merced River at Pohono Bridge (POH) in Yosemite National Park. Bottom: Wavelet coherence between the observed daily inflow to HTH and observed daily streamflow at POH, for WYs 1996-2013. The color shadings represent the strength of the relationship. The arrows denote the phase of the relationship, with rightward arrows denoting both variables are in-phase. The thick contours demarcate the 5% significance level against red noise.

4.2.2 GOES-derived solar radiation input

Satellite remote sensing technology has enabled researchers from various disciplines to retrieve and use high quality image data. Geostationary satellites like the GOES are particularly useful for operational purposes. Examples of such applications include solar energy and hydrologic forecasting. Here we utilize GOES-West visible albedo product, which has 4-km spatial and 30-minute temporal resolutions over the western U.S.

For this study, we derive SWF using the Ineichen-Perez algorithm (Ineichen and Perez, 1999). The algorithm requires cloud cover index (CC), also known as cloud dynamical range (Cano et al., 1986), clear-sky SWF (estimated using a simple algorithm in the American Society of Civil Engineers' evapotranspiration equations, available on <http://maeresearch.ucsd.edu/kleissl/files/R.m>), Linke turbidity factor (obtained from <http://www.soda-pro.com/help/general-knowledge/linke-turbidity-factor>), and station latitude, longitude and elevation as inputs.

The CC is defined as:

$$CC(i, d, t) = \frac{\alpha(i, d, t) - LB(i, d, t)}{UB(i, d, t) - LB(i, d, t)} \quad (4.1)$$

where α is the raw albedo, LB and UB are the lower and upper bounds of cloud dynamical range, respectively, i denotes the HRU, d denotes the day and t denotes the time of the day [see Cano et al. (1986), Ineichen and Perez (1999) for explanation]. The LB and UB are determined as the minimum and maximum values of α , respectively, within prescribed time windows (Perez et al., 2002). Based on our diagnostic where we compare the estimated SWF to the observed SWF at several stations, we determine that setting the daily-centered time windows to 7 days (± 3 days) for LB and to 91 days (± 45 days) for UB is optimal (appendix 4A).

The PRMS simulations run using Ineichen-Perez SWF are hereby called Baseline simulations. Compared to the default runs where DTR-based SWF is used, the Baseline simulations show a better performance in estimating the basin runoff throughout the snowmelt season, particularly in replicating the early and peak snowmelt season discharges (appendix 4C). In the PRMS modules that we employ, this improvement is noticeably greater in the Tuolumne River basin model than in the Merced River basin model.

Unless otherwise noted, any modifications to the cloudiness as a part of the experiments (section 4.3) are done on the cloud albedo component (α_{cloud}), defined as:

$$\alpha_{cloud}(i, d, t) = \alpha(i, d, t) - LB(i, d, t) \quad (4.2)$$

following Sumargo and Cayan (2017), where i denotes the HRU, d denotes the day and t denotes the time of the day. Other variables, such as temperature and precipitation, are kept the same. The LB is subsequently added back to the modified α_{cloud} to generate a modified α , which is then used to derive SWF.

4.3 PRMS Experiments to Explore Response to Cloudiness

A set of experiments are conducted to explore how cloudiness temporal variability and the spatial distribution of clouds affect runoff in west-slope Sierra Nevada, the primary source of water resources for California. These experiments compare runoff that occurs during a 19-year historical period from the upper Tuolumne River and upper Merced River basins simulations using the observed weather (precipitation, temperature and GOES-estimated SWF), called the Baseline simulations, with those whose cloudiness variability is altered, as described below.

4.3.1 Snow-fed streamflow response to daily cloudiness variability

The first experiment investigates snow-fed streamflow response to daily cloudiness variability by removing the artifacts of daily cloudiness variability in SWF input. For this purpose, the SWF input is similarly derived using Ineichen-Perez algorithm, except that the numerator of CC (α_{cloud}) is replaced with the annual harmonic of α_{cloud} , while other inputs/variables are kept the same. We find that replacing α_{cloud} with its annual harmonic

results in a $3,000 \text{ W m}^{-2}$ ($\sim 4\%$) deficit in the snowmelt season's (February-July) total SWF, when averaged over the 1996-2014 period over the upper Tuolumne River watershed. Over the upper Merced River watershed, this deficit amounts to $1,464 \text{ W m}^{-2}$ ($\sim 1\%$).

Figure 4.3 displays the behavior and magnitude of the resulting SWF estimate (hereby called “Annual harmonic clouds”), which retains the annual cycle of GOES SWF (Baseline), but with substantially smaller high-frequency variability. The difference between the Baseline simulation and “Annual harmonic clouds” simulation should reveal the relative contribution of daily cloudiness variations.

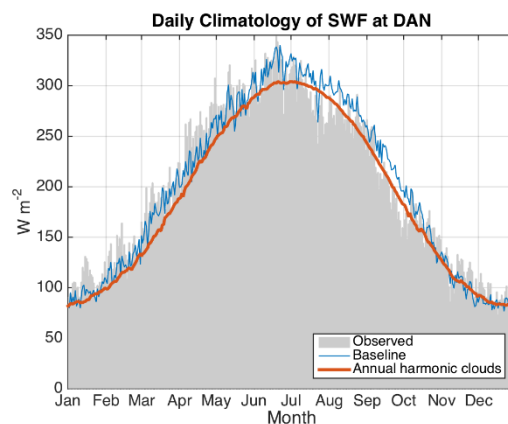


Figure 4.3. Daily climatology (1996-2014) of SWF at Dana Meadows (DAN) from observation, Ineichen-Perez algorithm with original α_{cloud} (Baseline), and Ineichen-Perez algorithm with annual harmonic α_{cloud} (Annual harmonic clouds).

4.3.2 Snow-fed streamflow response to high/mid/low elevation cloudiness

The second experiment investigates the effect of cloudiness at a specific elevation band on the snow-fed streamflow by removing α_{cloud} at high/mid/low elevation HRUs, while maintaining α_{cloud} at the other elevation HRUs. The other inputs/variables are kept the same. Different from the first experiment where the cloudiness is replaced with its annual harmonic, this experiment removes the cloudiness entirely, resulting in ~ 2 (from removing

low-elevation cloudiness)-3 (from removing mid and high-elevation cloudiness) times larger changes in February-July total basin-average SWF than those in the first experiment. Consequently, SWFs at high/mid/low elevation HRUs are the clear-sky SWFs, while SWFs at the other elevation HRUs remain unchanged. The modified simulations are hereby called “No clouds at high/mid/low elevation HRUs”.

For this purpose, the α_{cloud} multiplication factor (f) is defined as:

$$f(i) = \begin{cases} 1, & \text{if } z(i) < z_{t1} \\ 1, & \text{if } z_{t1} \leq z(i) \leq z_{t2} \\ 0, & \text{if } z(i) > z_{t2} \end{cases} \quad (4.3)$$

when α_{cloud} at high elevation HRUs are removed and α_{cloud} at the other elevation HRUs are maintained. Variable z is the HRU centroid elevation, while z_{t1} is the first tercile (33rd percentile) value of the elevations (2,481 m for upper Tuolumne and 2,302 m for upper Merced) and z_{t2} is the second tercile (67th percentile) value of the elevations (2,881 m for upper Tuolumne and 2,773 m for upper Merced). The tercile values are used as the elevation bands' cutoffs such that each elevation band consists of an equivalent number of HRU. When α_{cloud} at mid/low elevation HRUs are removed instead, the second/first criterion in Eq. (4.3) becomes 0, while the other criteria become 1.

The modified α_{cloud} is then:

$$\alpha'_{cloud}(i, d, t) = f(i) * \alpha_{cloud}(i, d, t) \quad (4.4)$$

where i denotes the HRU, d denotes the day and t denotes the time of the day. As a result, CC becomes 0 when $f = 0$, and remains unchanged when $f = 1$. SWF is subsequently derived using Ineichen-Perez algorithm. The differences between the Baseline and modified simulations should reveal the relative importance of cloudiness over high/mid/low elevation HRUs on streamflow.

For reference, the climatological mean February-July CCs of each HRU in the upper Tuolumne and upper Merced watersheds are displayed in Figure 4.4. The figure illustrates the spatial distributions of snowmelt season cloudiness in both watersheds, which are typically greater over higher elevation HRUs. Following this pattern, we find that the resulting increases in SWF from removing cloudiness are typically greater at higher elevation bands in both watersheds.

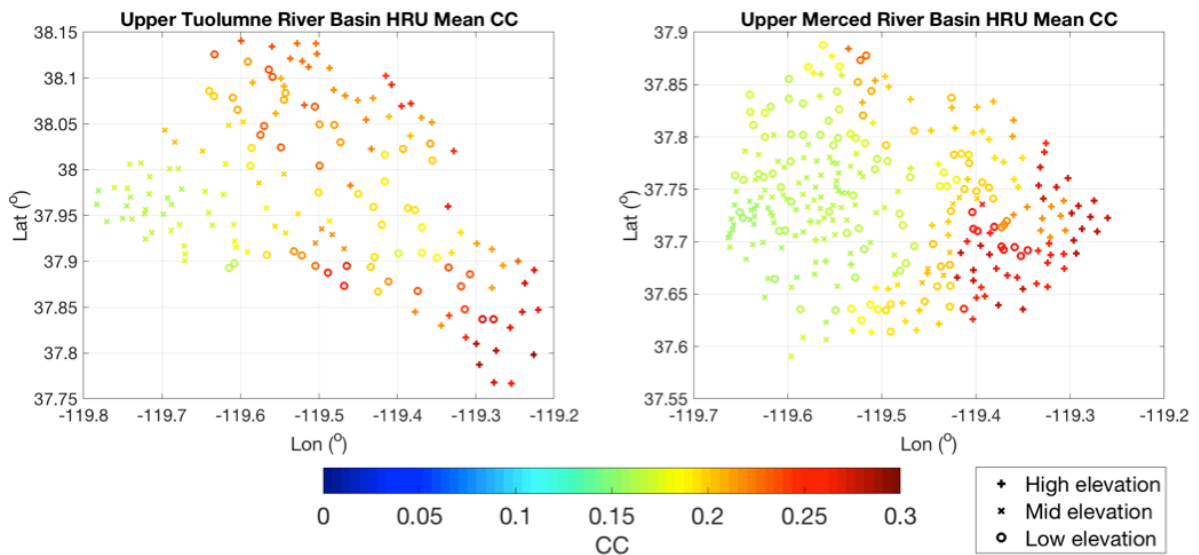


Figure 4.4. Snowmelt season (February-July) daily climatological mean (1996-2014 for Tuolumne and 1996-2013 for Merced) CC at each HRU in the Upper Tuolumne (left) and Merced (right) watersheds.

4.3.3 Snow-fed streamflow response to intensified daily cloudiness fluctuation

The third experiment investigates snow-fed streamflow response to intensified daily cloudiness fluctuations. This scheme is implemented on a daily basis by amplifying α_{cloud} to cloudy-sky condition during the relatively cloudy condition (Cloudy gets cloudier), or de-amplifying α_{cloud} to clear-sky condition during the relatively clear condition (Clear gets clearer). The “Cloudy gets cloudier” and the “Clear gets clearer” scenarios are conducted separately. As before, the other inputs/variables remain unchanged. A similar approach to

that in section 4.3.2 is applied. The amplification depends on the α_{cloud} value itself instead of the HRU elevation (z) and on the median value of α_{cloud} (α_{cm}) from all WYs, but specific to the HRU and time of the day. The median value is used as the clear/cloudy threshold, so each clear/cloudy category consists of an equivalent number of HRUs.

For the “Clear gets clearer” scenario, CC is set to 0 when α_{cloud} is less than α_{cm} and remains unaltered otherwise. This scheme results in 3,364 W m⁻² (~4%) and 631 W m⁻² (<1%) higher February-July total SWFs than in the Baseline, when averaged over the upper Tuolumne and Merced watersheds, respectively. For the “Cloudy gets cloudier” scenario, CC is set to 1 when α_{cloud} value is greater than α_{cm} and remains unaltered otherwise. This scheme results in disproportionately greater changes in the February-July total SWFs, with 26,791 W m⁻² (~31%) and 15,944 W m⁻² (~8%) lower February-July total SWFs than in the Baseline over the upper Tuolumne and Merced watersheds, respectively.

Subsequently, SWF is re-derived using Ineichen-Perez algorithm. To enable a direct comparison to the Baseline simulation, we impose a condition where the WY total SWF must equal to that in the Baseline simulation. The resulting WY total SWF difference from that in the Baseline simulation is added/subtracted from the “Clear gets clearer” and “Cloudy gets cloudier” simulations equally to/from each day of the WY. The differences between the Baseline and modified simulations should represent the relative importance of cloudiness on streamflow during the relatively clear/cloudy condition.

4.4 Results and Discussion

4.4.1 Snow-fed streamflow response to daily cloud variability

The 2010-2013 time series of the resulting hydrographs at HTH and POH from Baseline and “Annual harmonic clouds” simulations are displayed in Figure 4.5. The figure illustrates the behaviors of snow-fed streamflow response to daily cloudiness variations across different WYs, including the relatively wet WYs 2010 and 2011, and the relatively dry WYs 2012 and 2013. The daily climatological averages, including those for dry-year and wet-years subsets, are summarized in appendix 4D. Despite the different flow magnitudes, the plots exhibit similar behaviors between the HTH and POH hydrographs, consistent with the result from the wavelet coherence analysis (Figure 4.2). At both locations, the magnitudes of flow difference between the Baseline and “Annual harmonic clouds” simulations are comparable across the WYs (Figure 4.5, bottom panels).

Daily cloudiness variability results in slightly higher annual flows. When averaged over all WYs (1996-2014 for HTH and 1996-2013 for POH), the annual total runoff volume transport (Q_T) at HTH (POH) is ~ 44 (69) $\text{m}^3 \text{s}^{-1}$ higher in the Baseline simulations, equivalent to $\sim 0.4\%$ (1.1%). Over February-July period, these numbers become ~ 21 (41) $\text{m}^3 \text{s}^{-1}$, equivalent to $\sim 0.2\%$ (0.7%) higher in the Baseline simulations, signifying that 48% (60%) of the runoff difference at HTH (POH) occurs during the snowmelt season.

Over a seasonal scale, the Baseline simulation yields higher flows in early spring (by 5% at HTH and 7% at POH in February-April) and lower flows in mid spring (by 3% at both HTH and POH in May-June) than the “Annual harmonic clouds” simulation does. This feature is especially evident in the drier WYs 2012 and 2013 as shown in Figure 4.5, which indicates the Baseline runoff occurs earlier than the “Annual harmonic clouds” runoff.

However, the lag correlation between the flow time series from the two simulations shows a peak correlation at lag zero, suggesting this feature does not necessarily represent a shift in hydrograph, but a higher early-snowmelt-season flow in the Baseline simulation.

Indeed, in the wetter WYs 2010 and 2011, the Baseline simulation also yields higher flows in early summer (by 3% at both HTH and POH in July-August), along with higher early snowmelt season flows. In other words, compared to the climatological cloudiness cases, the observed daily cloudiness variability moderates the runoff by distributing it more evenly throughout the snowmelt season, especially in wetter years (also see appendix 4D). This dampening effect is emphasized over the change in annual/seasonal Q_T , reasonably since annual Q_T largely depends on the precipitation input, which is not modified in this experiment. Similar effects are observed for the snowmelt hydrographs (not shown), confirming the snowmelt-runoff correspondence.

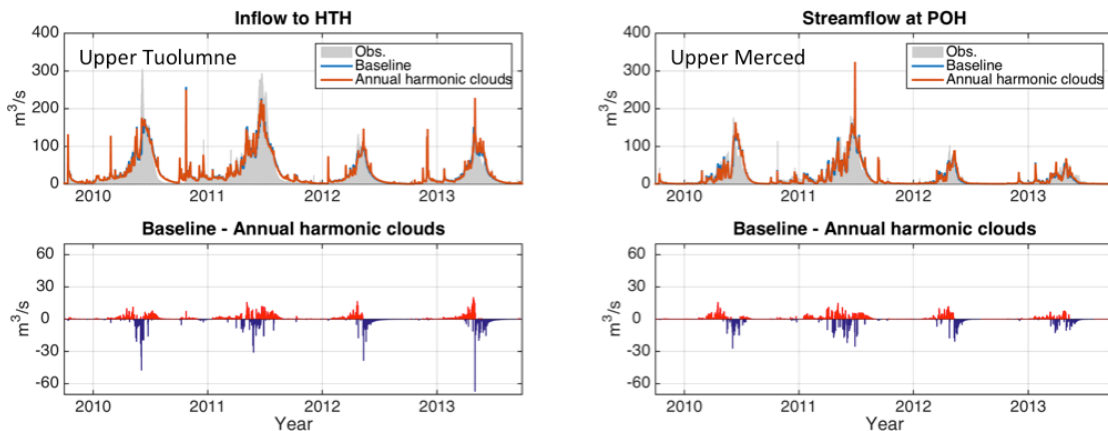


Figure 4.5. Top: WYs 2010-2013 time series of Tuolumne River inflow to HTH (left), and of Merced River inflow to POH (right), from Baseline (blue) and “Annual harmonic clouds” (orange) simulations. Bottom: Differences, Baseline minus “Annual harmonic clouds” simulations, where positive differences are shown as red and negative differences are shown as blue.

This pattern reflects the clear-cloudy sky interludes associated with daily CC fluctuations in the Baseline simulation. On the one hand, CC fluctuations can result in more cloudy-sky episodes, which strongly correlate with precipitation (Lapo et al., 2017; Sumargo and Cayan, 2018). The effect of rainfall-runoff is evident from the intermittent spikes in the hydrographs throughout the entire year.

On the other hand, CC fluctuations can also result in more clear-sky episodes with higher SWF for snowmelt energy input. In turn, more snowmelt-runoff can occur in early snowmelt season, leading to lower streamflow in mid snowmelt season. The HRU spring onsets [as defined in Cayan et al. (2001)] are mostly 1-4 days earlier in the Baseline simulation, especially at mid elevations (Figure 4.6). This characteristic is accentuated in the drier 2012 and 2013 (also see appendix 4D) and similarly present in the evapotranspiration (ET) plots, showing (~1%) higher ETs in early March and noisy, yet overall (~1%) lower ET in the subsequent months in the Baseline simulations (Figure 4.7). The relatively strong springtime ET fluctuations associated with daily CC variations supplements what Hidalgo et al. (2005) found across lower elevation sites in California.

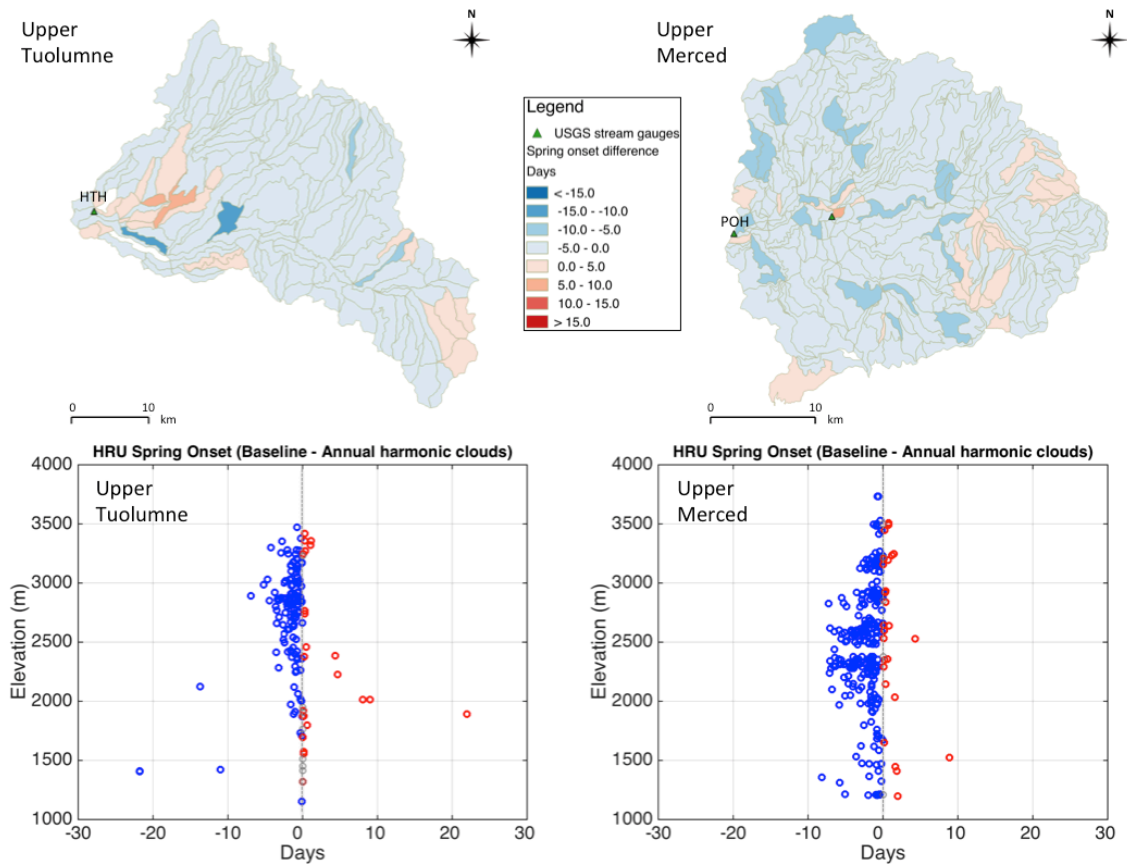


Figure 4.6. Differences in HRU spring onsets, for each year of 1996-2014, between Baseline and “Annual harmonic clouds” simulations, mapped (top) and plotted against HRU elevations (bottom), for the upper Tuolumne (left) and Merced (right) River basins. Reds denote positive differences, blues denote negative differences, and gray denotes no difference. Positive differences mean Baseline simulation results in later spring onsets, and vice versa. The plots are the daily climatological averages.

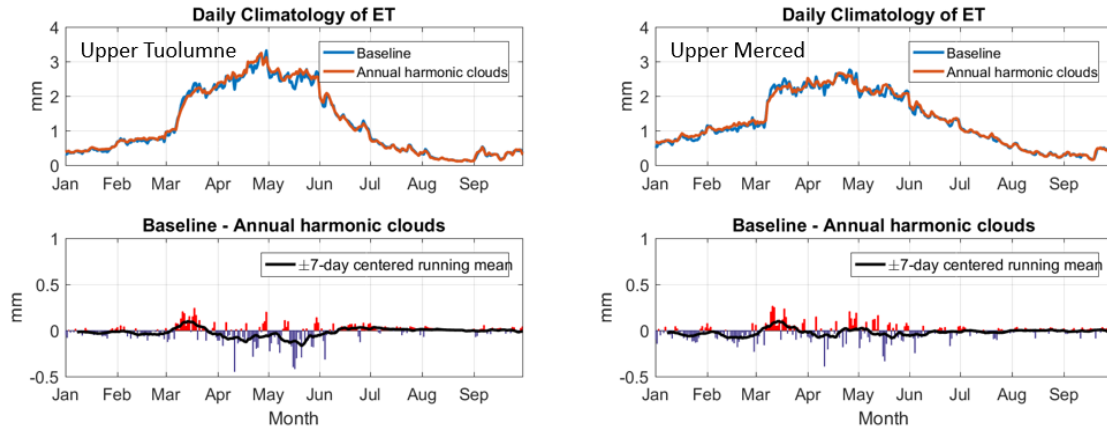


Figure 4.7. Daily climatological averages of basin area-weighted evapotranspiration (ET) of the Upper Tuolumne River (left) and the Upper Merced River (right) basins, for the Baseline and “Annual harmonic clouds” simulations (top) and those of the differences between the two simulations (bottom).

4.4.2 Snow-fed streamflow response to cloudiness at different elevation bands

The relative importance of cloudiness over high, mid and low elevation HRUs is illustrated in Figure 4.8. As expected, the differences between the Baseline and modified simulations consistently exhibit lower flows in earlier snowmelt period and higher flows in later snowmelt period in the Baseline simulation. This result illustrates the delayed flow timings due to cloudiness over all elevation bands, confirming the cloud-shading effect on snowpack and its runoff.

The flow differences between the Baseline and modified simulations exhibit different signatures across different elevation bands. The delays in flow timing are roughly comparable in the high and mid elevation cases (Figure 4.8, top and middle panels), but smaller in the low elevation case (Figure 4.8, bottom panels). However, qualitatively, the annual amplitudes of daily flow differences between the Baseline and modified simulations are largest in the mid elevation HRUs and smallest in the low elevation HRUs. The

magnitudes of flow difference between the Baseline and the modified simulations are reduced (heightened) in dry (wet) years.

Furthermore, the shifts in flow timing between the two simulations, i.e., when the flow difference is zero, take place earlier (later) in dry (wet) years. This behavior persists across all elevation bands when the analysis is performed for the dry-year and wet-year subsets (not shown). The differences in the climatological average of total February-July runoff Q_T at both HTH and POH are largest in the “No clouds at high elevation HRUs” scenario. Like in the previous experiment, however, the Q_T differences are small (<4%).

The small Q_T differences can partly be attributed to changes in ET, characterized by lower ET until April/May and higher ET afterwards in the Baseline simulation (not shown). The ET change is typically greater at lower-elevation HRUs owing to the warmer temperatures, with snowmelt season (February-July) averages of ~7% and of ~4% lower ET in the Baseline simulations of the upper Tuolumne and upper Merced watersheds, respectively. These numbers are smaller in dry years (6% and 2%, respectively) and larger in wet years (10% and 7%, respectively), reflecting the greater cloudiness difference between the Baseline and “No clouds at low elevation HRUs” scenarios, and its effect on ET in wetter years. The percentages of ET change are small (<1%) at mid and high-elevation HRUs. Overall, this result indicates that the effect of cloudiness and solar radiation variations in the PRMS model is greater on ET than on the streamflow.

As verification, this experiment is repeated using different elevation band cutoffs, e.g., at 2,500 m and 3,000 m instead of at the first (2,481 m for upper Tuolumne and 2,302 m for upper Merced) and second (2,881 m for upper Tuolumne and 2,773 m for upper Merced) terciles, respectively. The resulting hydrographs exhibit similar delays in flow timing (not

shown), but different magnitudes of flow differences between the Baseline and modified simulations, since each elevation band now contains a different number of HRU from before.

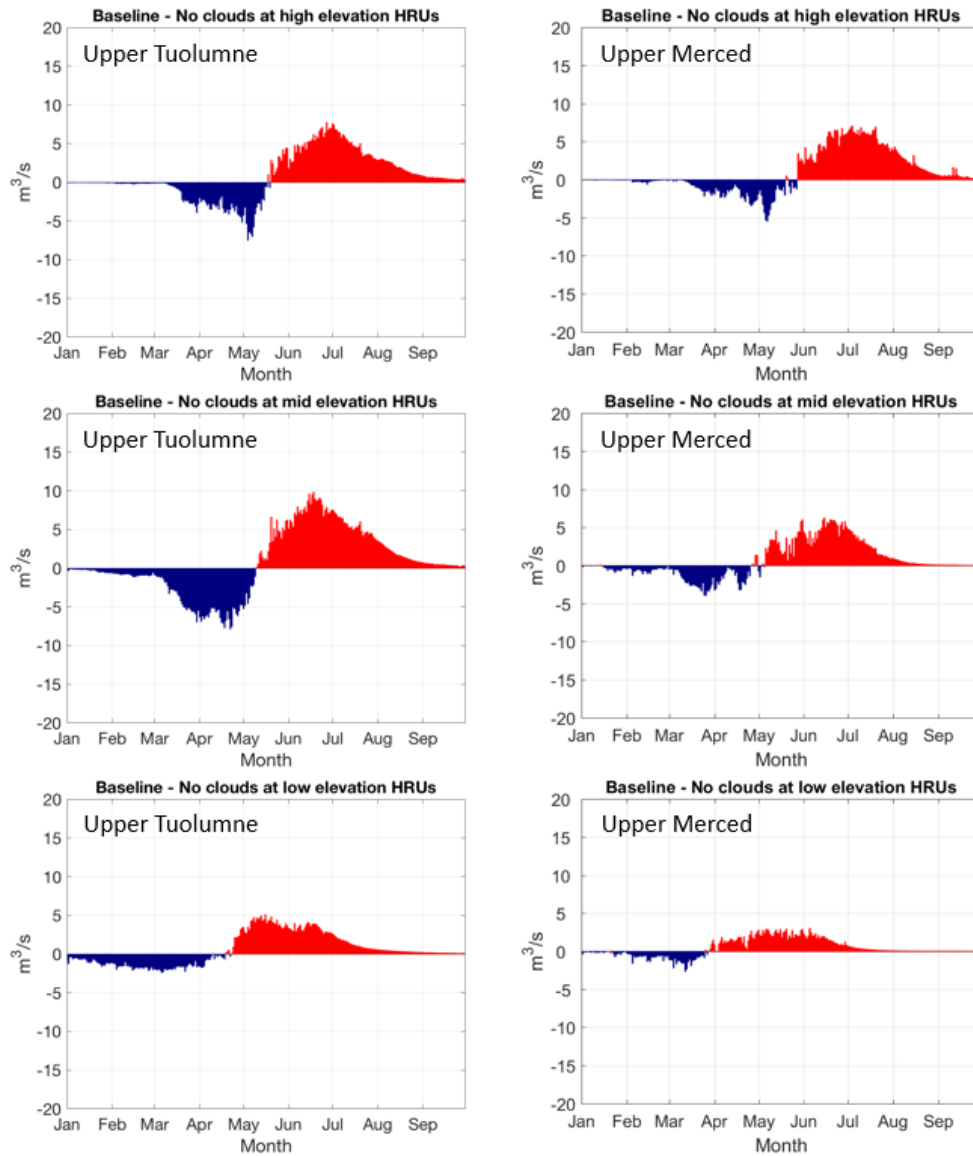


Figure 4.8. The differences in daily climatological averages of inflow to HTH (left) and of streamflow at POH (right) between Baseline simulation and “No clouds at high elevation HRUs” (top), or “No clouds at mid elevation HRUs” (middle), or “No clouds at low elevation HRUs” (bottom) simulation. Positive differences (red) mean Baseline simulation results in higher flows, and vice versa.

The delaying effect of cloudiness on the flow timing at HTH is further demonstrated by the spring onset differences (Figure 4.9), exhibiting 2-15 days (averaging ~3 days) later onsets in the Baseline simulations in most HRUs. On average, these numbers vary by ± 1 day in the dry-year and wet-year subsets, indicating the relative importance of cloudiness at each elevation band to spring onset is consistent across different WYs. Interestingly, earlier onsets associated with cloudiness also occur at some low elevation HRUs (Figure 4.9c), particularly along the main tributary of Tuolumne River near HTH (see Figure 4.2). The upper Merced River basin experiment yields similar results (not shown).

Forest cover and other local factors (e.g., topography and wind) that are not accounted for in this study may also influence the micrometeorology and snow distribution, thereby modifying snow mass and energy fluxes (Harding and Pomeroy, 1996; Trujillo et al., 2007; Lehning et al., 2008; Schirmer et al., 2011; Brauchli et al., 2017). To a lesser degree, a similar phenomenon happens at mid elevation HRUs, but in this case due to cloudiness over high elevation HRUs (Figure 4.9a).

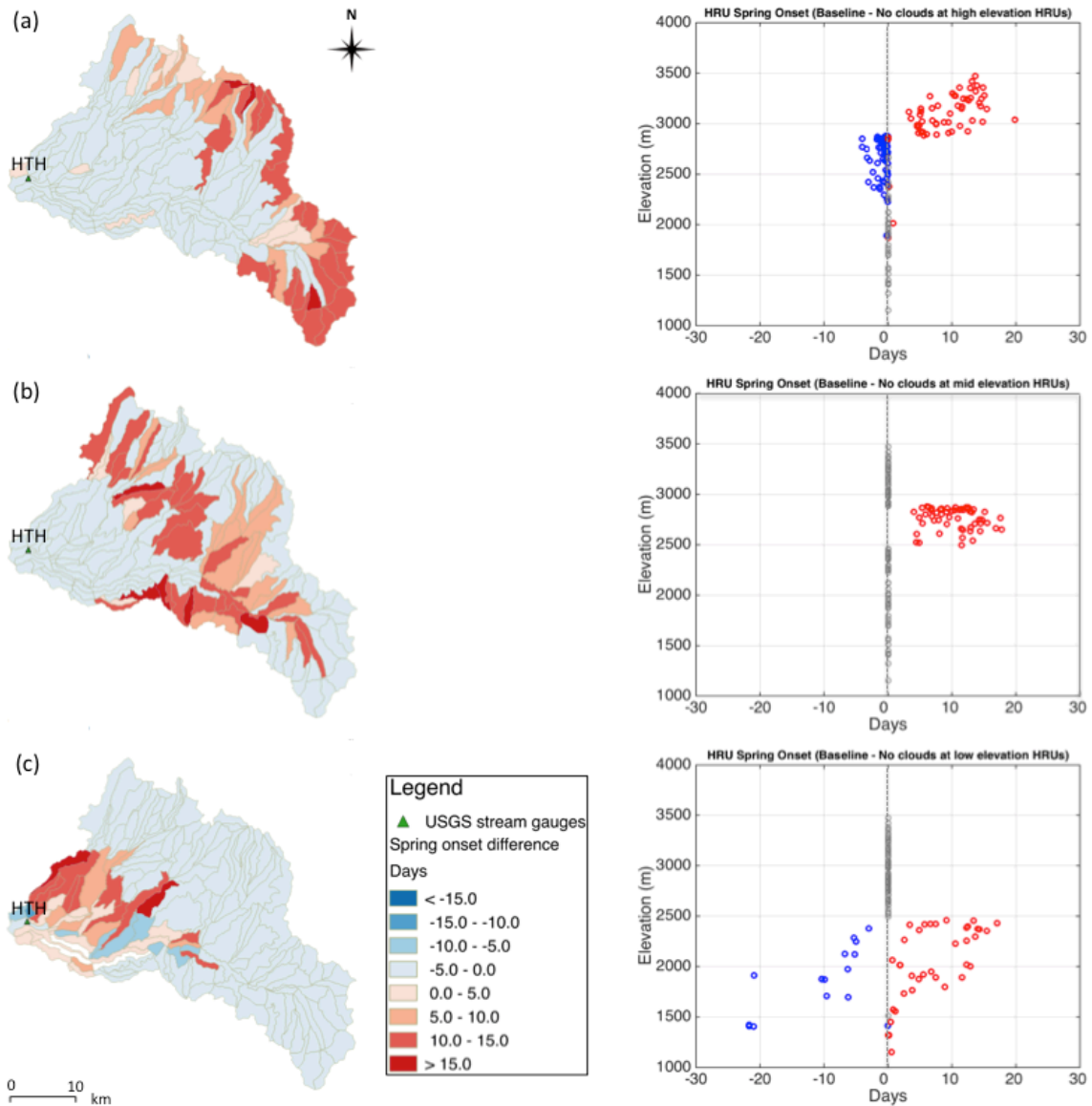


Figure 4.9. Differences in Upper Tuolumne River basin’s HRU spring onsets between Baseline simulation and No clouds at (a) high, (b) mid, and (c) low elevations HRUs simulations, mapped (left) and plotted against HRU elevations (right). Reds denote positive differences, blues denote negative difference, and gray denotes no difference. Positive differences mean Baseline simulation results in later spring onsets, and vice versa. The plots are the daily climatological averages.

4.4.3 Snow-fed streamflow response to intensified daily cloudiness fluctuations

Figure 4.10 illustrates the importance of cloudiness during the relatively clear-sky periods (top panels) and during the relatively cloudy-sky periods (bottom panels). As

expected, the Baseline simulations produce later hydrographs compared to the “Clear gets clearer” simulation, albeit with relatively tiny magnitudes of flow difference. Like in the previous experiments, the differences in the February-July climatological averages of HTH and POH Q_T between the two simulations are tiny ($\ll 1\%$).

In contrast, the Baseline simulations yield earlier hydrographs compared to the “Cloudy gets cloudier” simulation, with slightly elevated February-July HTH (by 2%) and POH (by 1%) Q_T , signifying the higher sensitivity of snow-fed streamflow to cloudiness perturbation during a relatively cloudy condition. The flow timings are noticeably earlier in the Baseline than in the “Cloudy gets cloudier” simulation, with mostly 2-7 days earlier spring onsets in both basins, averaging ~ 3 (5) days throughout the upper Tuolumne (Merced) River basin. The lag correlation between the daily climatological averages of the inflows to HTH from the two simulations suggests, on average, the Baseline simulation leads the “Cloudy gets cloudier” simulation by 5 days. This result is slightly different in the upper Merced case, with the strongest correlation at zero lag and a secondary peak correlation at 5-day lag.

Interestingly, the February-July mean ET difference between the Baseline and “Cloudy gets cloudier” simulations is only $\sim 1\%$. The small ET difference between the two simulations is likely an artifact of maintaining the same WY total SWF in both simulations (see Section 4.3.3). When this constrain is removed, the February-July mean ET is $\sim 6\%$ higher in the Baseline simulations, reasonably as cloudiness is lesser in the Baseline simulation.

This outcome seems to imply that the streamflow is more sensitive to cloudiness perturbation during the relatively cloudy condition. However, it may also be an artifact of the

clear/cloudy threshold used in the experiment, which is determined as the median value of all days throughout the time series for each individual HRU. When a different threshold (e.g., the 75th percentile) is used, the magnitudes of flow differences between the Baseline and the “Clear gets clearer” simulations becomes comparable to that between the Baseline and the “Cloudy gets cloudy” simulations. This discrepancy reflects the disproportionately greater number of days included in the “Clear gets clearer” case.

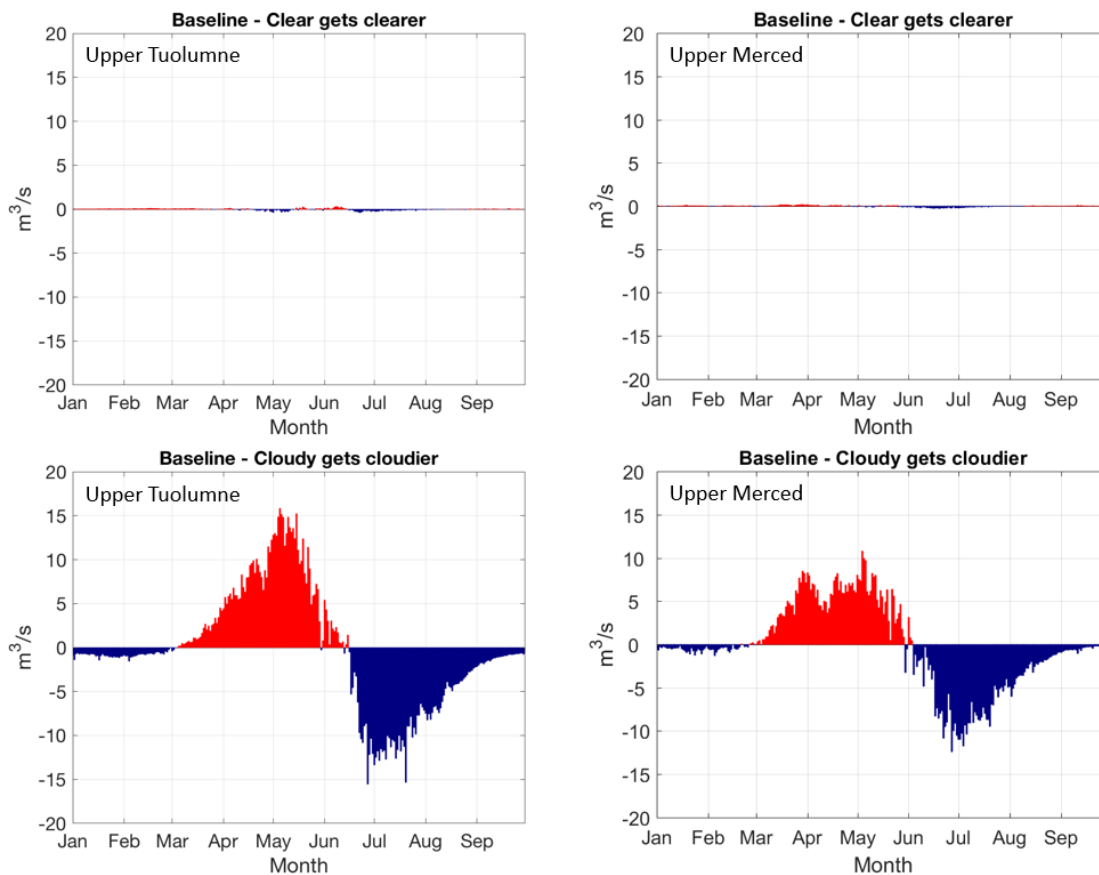


Figure 4.10. The differences in daily climatological averages of inflow to HTH (left) and of streamflow at POH (right) between Baseline simulation and “Clear gets clearer” simulation (left), and between Baseline simulation and “Cloudy gets cloudier” simulation (right). Positive differences (red) mean Baseline simulation results in higher inflows, and vice versa.

Further, using the median values as thresholds means each HRU has different threshold. When the threshold is set uniformly (e.g., to 0.1) across all HRUs, the results virtually look the same as those displayed in Figure 4.10. This means the HRUs with relatively abundant clear-sky conditions will lose more days than the HRUs with relatively abundant cloudy-sky conditions, so the former have disproportionately small contributions to the total flow.

The climatological averages of spring onset differences between the Baseline and the “Clear gets clearer” simulations are <2 days later in the Baseline simulations virtually across all HRUs of both basins. The same result is obtained for both dry-year and wet-year subsets. Also, the climatological averages of the February-July HTH and POH Q_T are $\ll 1\%$ lower in the Baseline simulation in both dry-year and wet-year subsets. The differences between the two simulations indicate consistently small flow timing and magnitude deviations in both dry-year and wet-year subsets.

On the other hand, the delay in hydrograph in the “Cloudy gets cloudier” simulation is longer in wet years than in dry years (Figure 4.11). The lag correlations between the daily climatological averages of both HTH and POH flows from the Baseline and “Cloudy gets cloudier” simulations suggest the delays are, on average, 5 days in wet years and 0 days in dry years. This dry-wet year asymmetry occurs despite the relatively small (± 2 days) variation in the spring onset.

By comparison, the climatological averages of the February-July Q_T are only $\sim 1\%$ lower in the Baseline simulation in the dry-year subset and $\sim 2\text{-}3\%$ higher in the Baseline simulation in the wet-year subset. This behavior consistently exemplifies the importance of flow timing over Q_T differences between the two simulations in dry years and wet years

alike. Overall, this result indicates amplified streamflow sensitivity to cloudiness perturbation in wetter years, reasonably as wetter years are generally cloudier (appendix 4B) and as this sensitivity is greater during a relatively cloudy condition in the first place (see above).

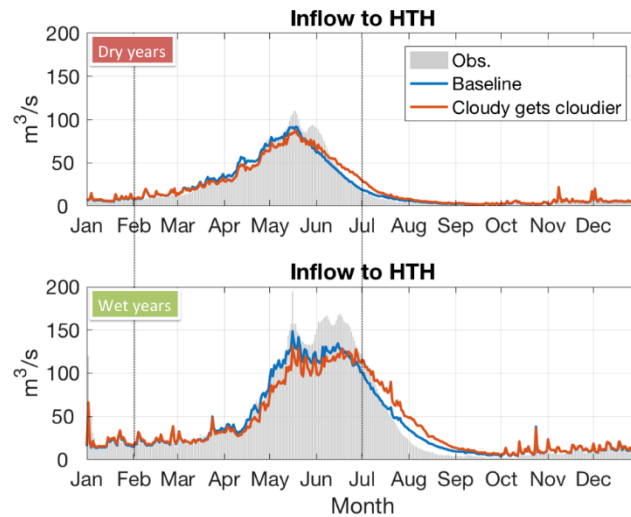


Figure 4.11. The daily climatological averages of the observed and simulated inflows to HTH for the dry-year (top) and wet-year (bottom) subsets, illustrating the different flow timings and discrepancies between the Baseline and “Cloudy gets cloudier” simulations between the two subsets. The vertical lines demarcate the February-July window when snowmelt is typically most active.

4.5 Summary and conclusions

We employ a recent version of the PRMS hydrological model, driven by observed and idealized meteorological inputs, to explore how runoff responds to varying cloudiness in the close-by snow-fed upper Tuolumne River and upper Merced River catchments on the west slope of the Sierra Nevada. This investigation considered three specific questions were addressed:

- 1) *How does the runoff generated within the basins respond to variations in cloudiness?*
- 2) *How does the runoff in the basins respond to elevation band-specific cloudiness?*
- 3) *How does snow-fed streamflow respond to intensified cloudiness fluctuations?*

We find that cloudiness variability modulates snow-fed streamflows by distributing the flows more evenly throughout the snowmelt season (February-July) in both upper Tuolumne and upper Merced River basins. The resulting seasonal flow distribution is more dominant than the resulting difference in flow volume, expectedly since we do not modify the precipitation input. This feature is evidenced by the higher flows in early (February-April) and late (July) snowmelt seasons, and lower flows in mid/peak (May-June) snowmelt season, with 1-4 days earlier spring onsets but virtually no shift in the overall hydrographs.

On the one hand, cloudiness variability allows more clear-sky episodes with relatively abundant solar radiation to melt the snowpack that, in turn, feeds into the streams. On the other hand, it also allows more cloudy-sky episodes that help to conserve the snowpack. These occurrences imply a competing effect of clear/cloudy sky on seasonal snowpack due to daily cloudiness variability. Subsequently, the snow-fed streamflows are lower in mid snowmelt season because of the modulation.

When comparing the effects of cloudiness from different elevation bands (i.e., high, mid and low), we find that higher elevation cloudiness has a greater influence on both flow volume and timing. Like in the first experiment above, the effect on the flow timing is greater than that on the flow volume. We also find significant evapotranspiration (ET) response to cloudiness at low elevation sites, with basin-average spring-summer reduction in ET by 4%-7% due to cloudiness. Averaged over the 1996-2014 period, cloudiness delays the spring onset by 2-15 days (averaging ~3 days) regardless of the elevation band. These numbers also indicate the greater effect from removing cloudiness than from removing the day-to-day cloudiness fluctuations (as in the previous experiment) on the spring onset. Similar patterns are observed in the dry-year and wet-year subsets, with spring onset variations of ± 1 day

from the all-year subset, indicating the relative importance of cloudiness at each elevation band is consistent across different WYs.

In evaluating the effects of intensification in cloudiness, we find that snow-fed streamflow is more sensitive to perturbation during the relatively cloudy periods. This sensitivity manifests as larger annual amplitude of daily flow difference and as shifts in hydrograph and in spring onset. For example, averaged across all HRUs, the spring onsets are 3-5 days later as cloudy periods get cloudier and virtually unchanged as clear periods get clearer. By comparison, widespread warming in the western North America during the second half of the 20th century resulted in 1-4 weeks earlier spring onsets (Stewart et al., 2005), which highlights the potential role of cloudiness in moderating the effect of climate change-related springtime warming. These numbers barely change from dry to wet years, varying by ± 2 days only. However, the delay in the annual hydrograph because “cloudy periods get cloudier” is, on average, 5 days in wet years and 0 day in dry years. These patterns are also sensitive to the clear/cloudy threshold (i.e., the definition of clear vs. cloudy condition) used in the analysis, so care must be taken when evaluating hydrologic sensitivity to future change in cloudiness.

Acknowledgement. ES was funded by the California Department of Water Resources Award 4600010378. DRC was funded by the California Energy Commission, the NOAA RISA program, and the Southwest Climate Science Center sponsored by the U.S. Department of Interior and the U.S. Geological Survey. Many thanks to Sam Iacobellis for providing access to GOES imagery, to Bruce Cornuelle, Michael Dettinger, Alexander Gershunov and Steven Margulis for thoughtful discussions, to Bruce McGurk for providing access to Hetch

Hetchy Reservoir inflow data, and to John King for providing access to CDWR modules of PRMS model. This chapter is currently being prepared for submission for publication. Sumargo, E., Effects of Cloud Variability on Snow-fed Runoffs in California's Sierra Nevada. The dissertation author was the sole investigator and author.

APPENDIX 4A

Determining the Time Windows of UB and LB

The time windows for UB and LB (T) used in this study is determined from the Ineichen-Perez model performance in estimating SWF. Theoretically, UB represents the cloudiest condition a GOES pixel can get and, for this reason, UB is relatively constant over time (Perez et al., 2002). The LB represents the contributions of surface and non-cloud atmospheric constituents, which can rapidly evolve within a few days and has seasonality, especially at pixels with seasonal snow cover. For this purpose, we test the optimal T by varying it from as low as 7 days (± 3 days) to as high as 181 days (± 90 days) in both UB and LB cases. The SWF is then computed separately for each value of these T . The correlations (R) and root-mean-squared errors (RMSE) between the observed and modeled SWF are calculated to evaluate the model's performance.

The top panels of Figure 4.A1 show the R and RMSE of the UB case as functions of T when they are calculated for all months and for the February-July period (snowmelt season), with the T of the LB case being held constant at 7 days. The plots exhibit remarkable initial improvements in the algorithm's performance by showing significantly higher R and lower RMSE as T increases. Changes in R and RMSE start to plateau on 91-day time window onward, indicating retarded improvement in the algorithm's performance. Although the

performance keeps improving at $T > 91$ days, any higher T values would require longer dataset to include in the computational process, in which more days, i.e., the first and last T days of the time series, would lose information. For this reason, we determine that the 91-day time window is optimal for the UB case.

The bottom panels in Figure 4.A1 show the R and RMSE of the LB counterpart, with the T of the UB case being held constant at $T = 91$ days. Unlike in the UB case, the sharp increase in R and decrease in RMSE are limited to $T = 7$ days. The values of R and RMSE at $T > 7$ days are virtually constant. Any shorter T values would greatly increase the risk of not having a clear day within the time window. In fact, we find that shorter T values do not necessarily improve the algorithm's performance (not shown). These patterns remain unchanged when the T of the UB case is varied. Therefore, we determine that the 7-day time window is optimal for the LB case.

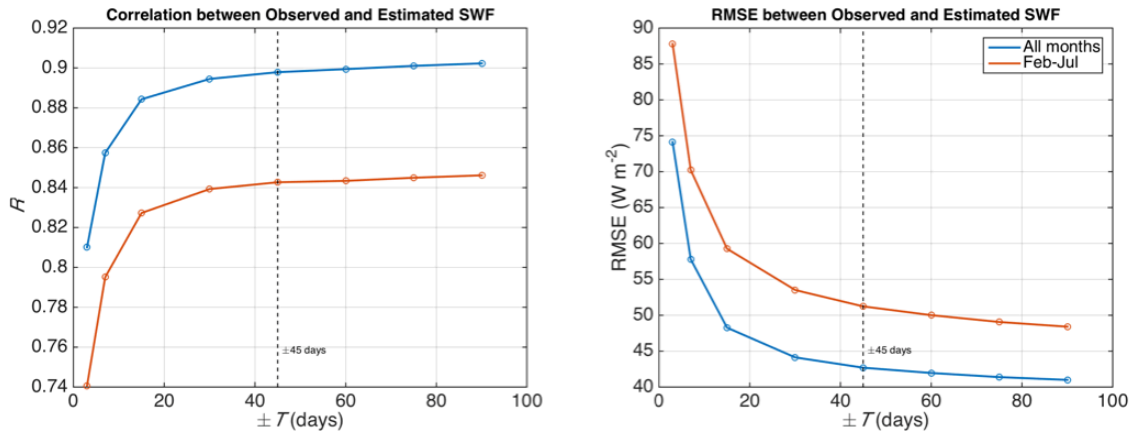


Figure 4.A1. The R (left) and RMSE (right) between the observed and Ineichen-Perez estimated SWF at Dana Meadows in California (37.897 °N, 119.257 °W, 2,987 m) for all months (blue) and February-July period (red) of 1996-2014, for the UB (top) and LB (bottom) cases. The dots represent the specific time windows (T) used to compute UBs and LBs, which are then used to derive the SWFs. The vertical dotted lines denote the ± 45 -day window for UB and the ± 3 -day window for LB used in this study.

APPENDIX 4B

Determining dry vs. wet years

For the Tuolumne River basin, the dry-year and wet-year subsets are determined from the January-September total inflow to HTH (Figure 4.B1, top panel). The 9 driest years are those with lowest total inflow, while the 9 wettest years are those with the highest total inflow on record (1996-2014). As a comparison, the January-September mean α_{cloud} , composited over all HRUs of the upper Tuolumne River basin, is computed for each WY. The result demonstrates that wet years coincide with cloudy years, and vice versa, in most occasions (Figure 4.B1, bottom panel), with a Pearson's correlation coefficient of 0.86, signifying the significance of cloudiness to streamflow throughout winter-summer.

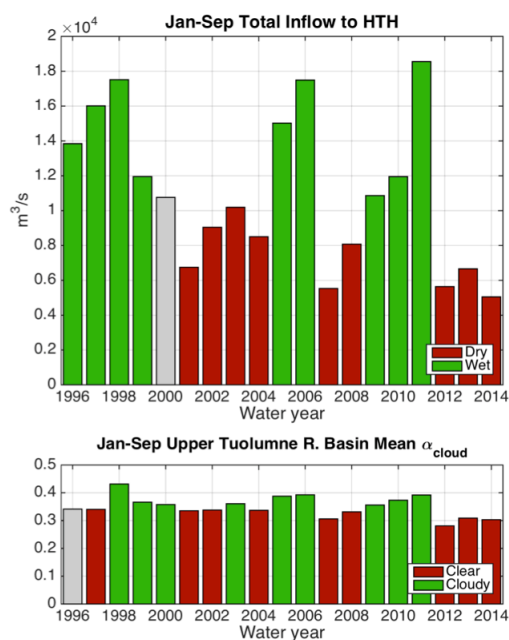


Figure 4.B1. Top: January-September total inflow to HTH for every water year of 1996-2014, showing 9 wettest and 9 driest years in the period. Bottom: January-September upper Tuolumne River basin composite mean α_{cloud} for every water year of 1996-2014, showing its overall consistency with the total inflow.

The same method is applied to streamflow at POH for the Merced River basin, except that 9 driest and 9 wettest years are sorted from 1996-2013 only, following the data availability.

APPENDIX 4C

PRMS model calibration

The initial simulation with GOES SWF input yielded larger bias and root-mean-squared error (RMSE) in daily basin runoff simulation than that with default temperature range-based SWF. Thus, to accommodate the more realistic GOES SWF, a new parameter calibration of the Tuolumne PRMS model was required.

Dr. Chris Graham of San Francisco Public Utilities Commission recommended a selected set of parameters used in PRMS that would likely be the most important for a re-calibration adjustment; he shared a MATLAB[®] code that allowed the user to setup several runs, each with a different combination of parameters. The large number of parameters that could be calibrated, under many possible permutations to derive an optimal model posed a significant challenge to the calibration effort, but the initial choices of likely parameters that probably came into play helped to reduce those.

Having performed numerous runs using the sets of parameters explored within the set of runs described above, the search for an optimal parameter tuning was reduced to a significantly narrower range. As a result, the ongoing calibration effort can employ a more explicit Gauss-Newton optimization [see Verdy et al. (2014) for more detail]. This approach is an inverse method utilizing Taylor's expansion and based on the least-square regression. This technique recognizes that, while the parameters may be non-linear, they are

approximately linear at a certain point/range. The purpose of this optimization method is to generate estimates of optimal parameter values. In our case, the optimization is performed by minimizing the RMSE between the simulated and observed daily time series of inflow to HTH for the Tuolumne module, and of stream discharge at POH for the Merced module.

The performances of PRMS model simulations using the original DTR and calibrated GOES are summarized in Table 4.C1, and illustrated in Figure 4.C1 for the Tuolumne model and in Figure 4.C2 for the Merced model. The results show considerable improvement in the simulated flows in both basins. The improvement is especially noticeable in the Tuolumne case, where the simulation using calibrated GOES SWF better captures both the shape of and the peak hydrograph.

In the dry-year subset (see Appendix 4B), the inflow overestimations in March and April are significantly reduced. In the wet-year subset, the inflow overestimations between June and August are similarly reduced. Similar improvements are observed in the Merced case, except with smaller magnitudes. Nevertheless, the simulation using calibrated GOES SWF still fall short from capturing a few spikes in the hydrographs, which likely reflects the deficiency of precipitation inputs.

Table 4.C1. The correlations (R), root-mean-squared errors (RMSE) and Nash-Sutcliffe Efficiencies (NSE) between the daily climatological averages of the observed and PRMS simulated inflow to HTH and streamflow at POH, using the original diurnal temperature range-based SWF (DTR) and the calibrated Ineichen-Perez SWF based on GOES α (GOES), for all-year, dry-year and wet-year subsets.

Subset	Scenario	HTH			POH		
		R	RMSE	NSE	R	RMSE	NSE
All	DTR	0.97	0.05	0.9	0.97	0.06	0.86
	GOES	0.99	0.03	0.97	0.98	0.06	0.87
Dry	DTR	0.93	0.07	0.85	0.95	0.07	0.85
	GOES	0.99	0.03	0.97	0.95	0.07	0.84
Wet	DTR	0.97	0.06	0.89	0.94	0.07	0.82
	GOES	0.99	0.04	0.95	0.96	0.07	0.83

Note. The hydrographs are normalized using their water yearly amplitudes, so the statistics can be compared directly across all subsets. The GOES simulation becomes the Baseline simulation in the rest of the paper.

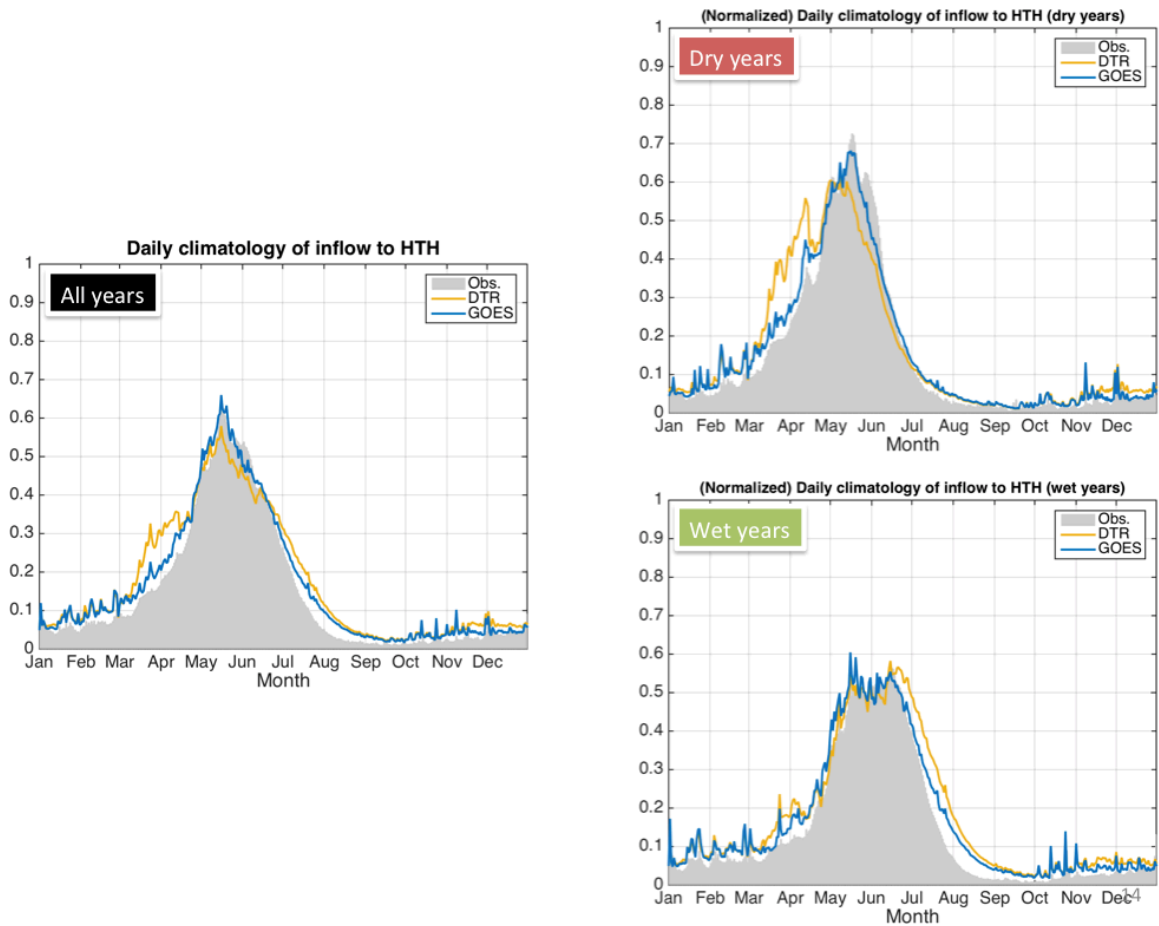


Figure 4.C1. The observed (shade) and simulated (plots) daily climatology of inflow to HTH using the original diurnal temperature range (DTR) method and using calibrated Ineichen-Perez algorithm based on GOES α (GOES), for all-year (left), dry-year (upper right) and wet-year (lower right) subsets. The hydrographs are normalized using their water yearly amplitudes, so the difference between the two simulations can be compared directly across all subsets. Note that GOES simulation becomes the Baseline simulation in the rest of the paper.

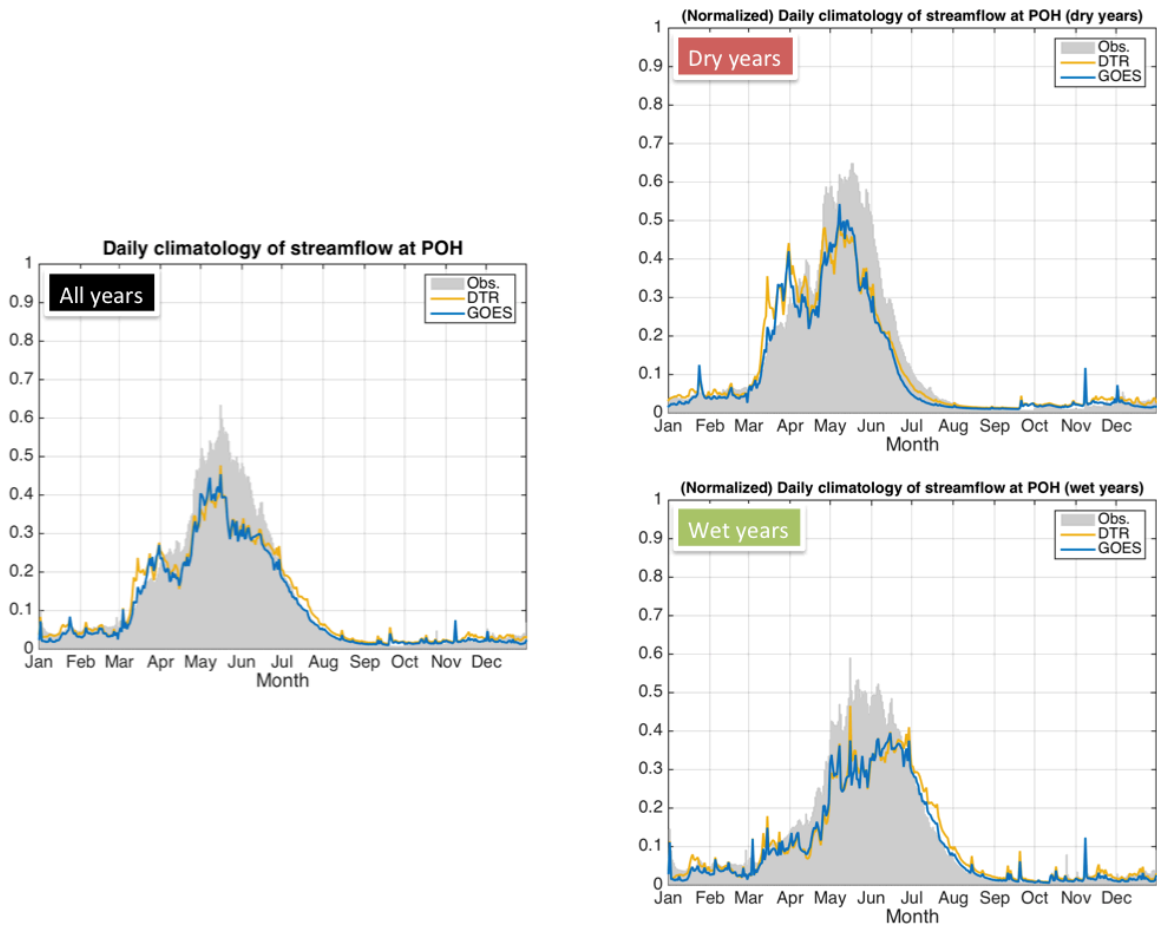


Figure 4.C2. Same as Figure 4.C1, except for the PRMS Merced model.

APPENDIX 4D

Different effects of “Annual harmonic clouds” in dry vs. wet years

Using the “Annual harmonic clouds” (Section 4.3.1) to derive SWF may introduce positive cloudiness bias in dry years and negative cloudiness bias in wet years over seasonal-annual time scales. These biases mean negative SWF bias in dry years and positive SWF bias in wet years, respectively. Therefore, The annual harmonics of GOES α_{cloud} are re-derived for dry-year and wet-year subsets, separately. The dry-year and wet-year subsets are defined in Appendix 4B.

For the upper Tuolumne River basin, the dry-year subset exhibits an earlier streamflow in the baseline simulation (Figure 4.D1, left panel), demonstrating that cloudiness variations hasten streamflow timing. This outcome signifies more frequent clear/cloudy sky interludes and hence more clear-sky episodes, which in turn allow more days with higher SWFs for snowmelt energy input. The wet-year subset does not display a shift in hydrograph (Figure 4.D1, right panel). Instead, it displays a dampened hydrograph, with higher flows in early (February-mid May) and late (mid June-August) snowmelt season, and lower flows in mid snowmelt season (mid May-mid June).

Furthermore, the flow difference between the two simulations appears noisier in the wet-year subset. This reflects the fact that how dry/wet a water year is strongly correlates with cloudiness (Figure 4.B1), and that the frequency of clear-cloudy sky interludes is greater in the Baseline simulation. On one hand, these results indicate the relative importance of cloudiness variations to streamflow timing in drier years. On the other hand, they imply cloudiness variations result in more even runoff distribution throughout the snowmelt season.

The ET profiles (not shown) and the results the upper Merced River basin show largely similar behaviors to those from the upper Tuolumne River basin in both dry-year and wet-year subsets. In the dry-year subset, the main difference occurs in the first half of June, where the Baseline simulation yields a slightly higher flow than the “Annual harmonic clouds” simulation. In the wet-year subset, the dampening of hydrograph appears less defined than in the upper Tuolumne River basin result.

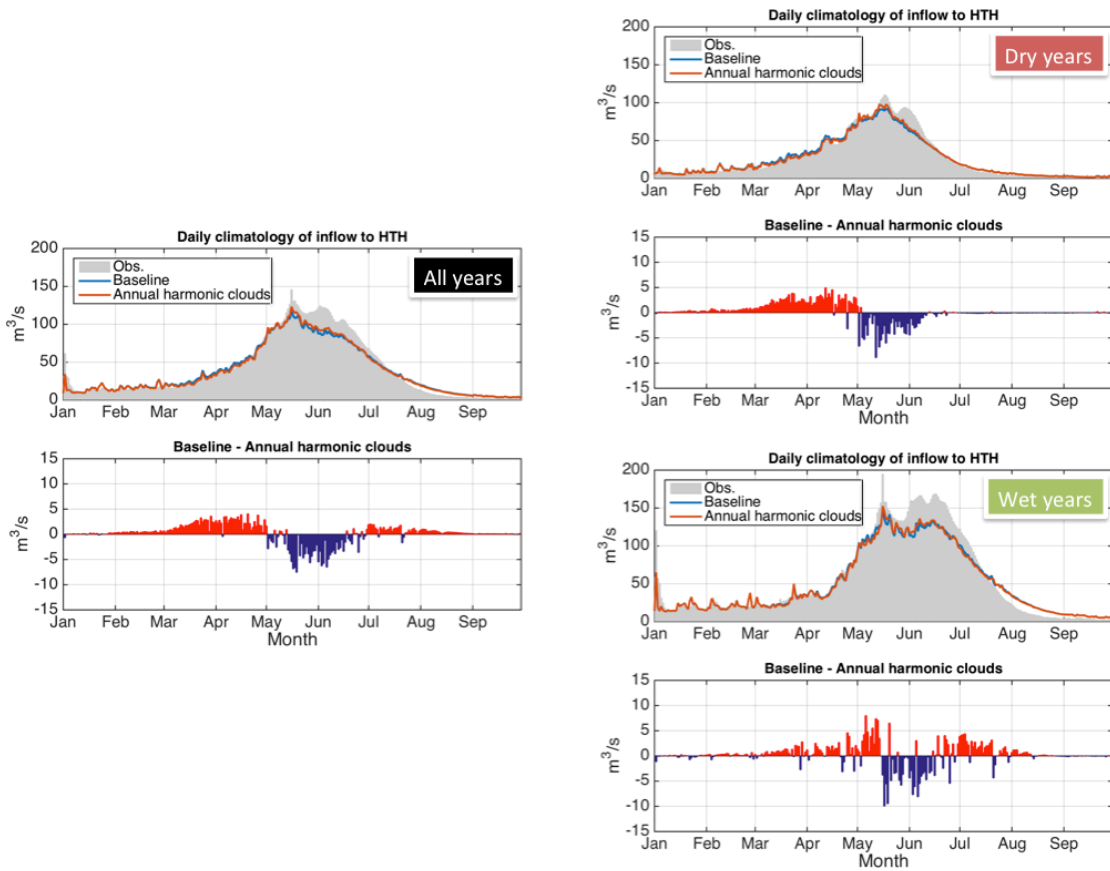


Figure 4.D1. Top sub-panels: Daily climatology (1996-2014) of inflow to HTH for all-year (left), dry-year (top right) and wet-year (bottom right) subsets from PRMS upper Tuolumne River basin model Baseline and “Annual harmonic clouds” simulations. Bottom sub-panels: The resulting difference between the Baseline and “Annual harmonic clouds” simulations. The y-axis scales are set to be different from those in Figure 4.5 for clarity of presentation.

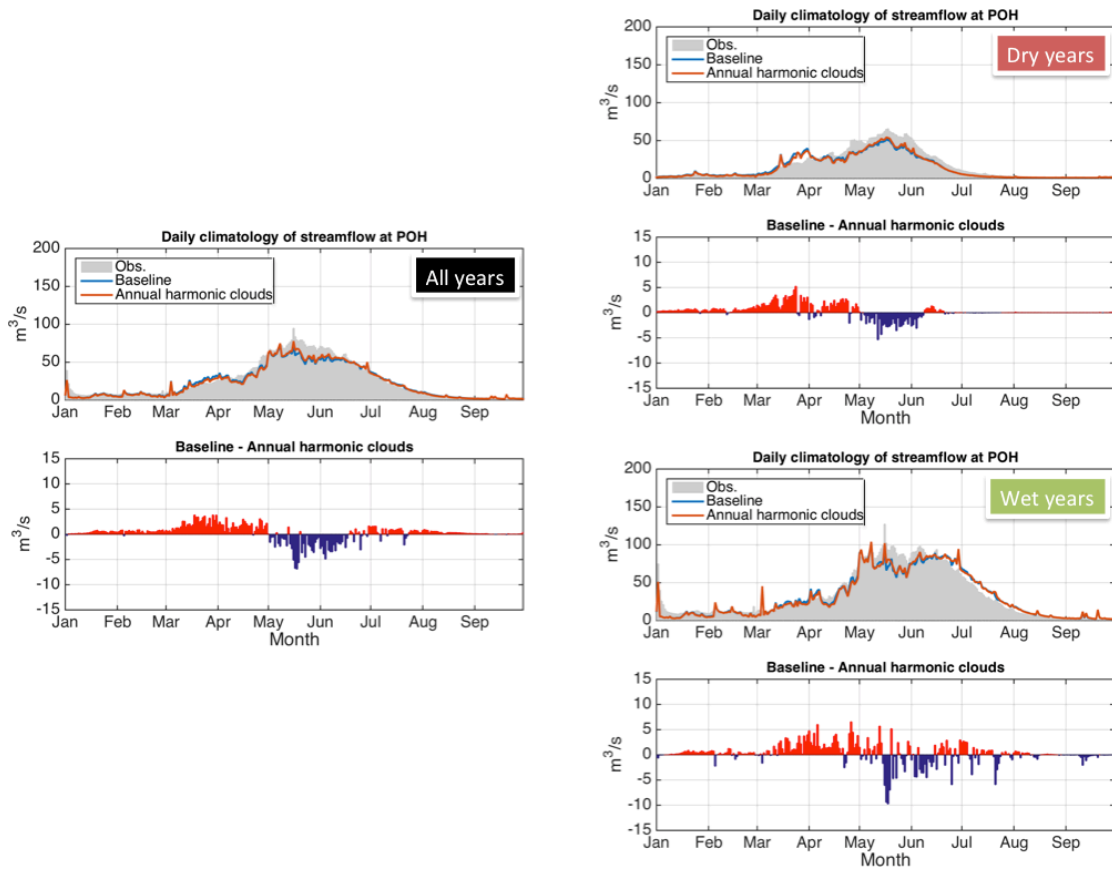


Figure 4.D2. Same as Figure 4.D1, except for streamflow at POH from PRMS upper Merced River basin model.

REFERENCES

- Bales, R. C., N. P. Molotch, T. H. Painter, M. D. Dettinger, R. Rice, and J. Dozier, 2006: Mountain hydrology of the western United States. *Water Resour. Res.*, **42**(8).
- Beniston, M., 2010: Impacts of climatic change on water and associated economic activities in the Swiss Alps. *J. Hydrol.*, **412-413**, 291-296. doi:10.1016/j.jhydrol.2010.06.046.
- Bohn, T. J., B. Livneh, J. Oyler, S. W. Running, B. Nijssen, and D. P. Lettenmaier, 2013: Global evaluation of MTCLIM and related algorithms for forcing of ecological and hydrological models. *Agric. For. Meteorol.*, **176**, 38-49, doi:10.1016/j.agrformet.2013.03.003.
- Brauchli, T., Trujillo, E., Huwald, H., & Lehning, M., 2017: Influence of slope-scale snowmelt on catchment response simulated with the Alpine3D model. *Water Resour. Res.*, **53**. <https://doi.org/10.1002/2017WR021278>
- California Department of Water Resources (2017, September). What a Difference a Year Makes. *Water Year 2017: What a Difference a Year Makes*.

- Cano, D., J. M. Monget, M. Albuissou, H. Guillard, N. Regas, and L. Wald, 1986: A method for the determination of the global solar radiation from meteorological satellite data. *Solar Energy*, **37**, 31-39.
- Cayan, D. R., K. T. Redmond, and L. G. Riddle, 1999: ENSO and Hydrologic Extremes in the Western United States. *J. Climate*, **12**, 2881–2893, [https://doi.org/10.1175/1520-0442\(1999\)012<2881:EAHEIT>2.0.CO;2](https://doi.org/10.1175/1520-0442(1999)012<2881:EAHEIT>2.0.CO;2)
- Cayan, D. R., M. D. Dettinger, D. Pierce, T. Das, N. Knowles, F. M. Ralph, and E. Sumargo, 2016: Natural variability, anthropogenic climate change, and impacts on water availability and flood extremes in the Western United States, in *Water Policy and Planning in a Variable and Changing Climate*, edited by K. A. Miller et al., pp. 17–42, CRC Press, Boca Raton, Fla.
- Cayan, D. R., M. D. Dettinger, H. F. Diaz, and N. E. Graham, 1998: Decadal Variability of Precipitation over Western North America. *J. Climate*, **11**, 3148–3166, [https://doi.org/10.1175/1520-0442\(1998\)011<3148:DVOPOW>2.0.CO;2](https://doi.org/10.1175/1520-0442(1998)011<3148:DVOPOW>2.0.CO;2)
- Cayan, D. R., S. A. Kammerdiener, M. D. Dettinger, J. M. Caprio, and D. H. Peterson, 2001: Changes in the Onset of Spring in the Western United States, *Bull. Amer. Meteorol. Soc.*, **82**, 399–415.
- Cline, D. W., 1997: Snow surface energy exchanges and snowmelt at a continental, midlatitude Alpine site. *Water Resour. Res.*, **33**(4), 689-701.
- Comola, F., B. Schaeffli, P. Da Ronco, G. Botter, M. Bavay, A. Rinaldo, A., and M. Lehning, 2015: Scale-dependent effects of solar radiation patterns on the snow-dominated hydrologic response. *Geophys. Res. Lett.*, **42**. doi:10.1002/2015GL064075.
- Das, T., D. W. Pierce, D. R. Cayan, J. A. Vano and D. P. Lettenmaier, 2011: The importance of warm season warming to western U.S. streamflow changes. *Geophys. Res. Lett.*, **38**, L2403, doi:10.1029/2011GL049660.
- Dettinger, M., 2011: Climate change, atmospheric rivers, and floods in California—A multimodel analysis of storm frequency and magnitude changes. *J. Am. Water Resour. Assoc.*, **47**(3), 514–523, doi:10.1111/j.1752-1688.2011.00546.x.
- Dettinger, M. D., F. M. Ralph, T. Das, P. J. Neiman, and D. Cayan, 2011: Atmospheric rivers, floods, and the water resources of California. *Water*, **3**, 455–478.
- Dettinger, M., 2014: Climate change: Impacts in the third dimension, *Nature Geoscience*, **7**, 166–167, <https://doi.org/10.1038/ngeo2096>.
- Dettinger, M. D., 2013: Atmospheric Rivers as Drought Busters on the U.S. West Coast. *J. Hydrometeorol.*, **14**, 1721–1732, <https://doi.org/10.1175/JHM-D-13-02.1>
- Dettinger, M., K. Redmond, and D. Cayan, 2004: Winter Orographic Precipitation Ratios in the Sierra Nevada—Large-Scale Atmospheric Circulations and Hydrologic Consequences. *J. Hydrometeorol.*, **5**, 1102–1116, <https://doi.org/10.1175/JHM-390.1>

Downing, J., 2015: Forest thinning may increase water yield from the Sierra Nevada. *Calif. Agric.*, **69**, 10–11, <https://doi.org/10.3733/ca.v069n01p10>.

Frierson, D. M. W., 2006: Robust increases in midlatitude static stability in global warming simulations. *Geophys. Res. Lett.*, **33**, L24816, doi:10.1029/2006GL027504.

Gergel, D. R., B. Nijssen, J. T. Abatzoglou, D. P. Lettenmaier, and M. R. Stumbaugh, 2017: Effects of climate change on snowpack and fire potential in the western USA. *Climatic Change*, **141**(2), 287-289.

Grinsted, A., J. C. Moore, S. Jevrejeva, 2004: Application of the cross wavelet transform and wavelet coherence to geophysical time series. *Nonlin. Process. Geophys.*, **11**, 561566.

Grünewald, T., Y. Bühler, and M. Lehning, 2014: Elevation dependency of mountain snow depth. *The Cryosphere*, **8**(6), 2381–2394. <https://doi.org/10.5194/tc-8-2381-2014>.

Guan, B., D. E. Waliser, N. P. Molotch, E. J. Fetzer, and P. J. Neiman, 2012: Does the Madden–Julian Oscillation Influence Wintertime Atmospheric Rivers and Snowpack in the Sierra Nevada?. *Mon. Wea. Rev.*, **140**, 325–342, <https://doi.org/10.1175/MWR-D-11-00087.1>.

Guan, B., N. P. Molotch, D. E. Waliser, E. J. Fetzer, and P. J. Neiman, 2010: Extreme snowfall events linked to atmospheric rivers and surface air temperature via satellite measurements. *Geophys. Res. Lett.*, **37**, L20401, doi:10.1029/2010GL044696.

Hantel, M., and L. M. Hirtl-Wielke, 2007: Sensitivity of Alpine snow cover to European temperature. *Int. J. Clim.*, **27**, 1265–1275.

Harding, R. J., and J. W. Pomeroy, 1996: The energy balance of the winter boreal landscape. *J. Climate*, **9**(11), 2778–2787. [https://doi.org/10.1175/1520-0442\(1996\)009<2778:TEBOTW>2.0.CO;2](https://doi.org/10.1175/1520-0442(1996)009<2778:TEBOTW>2.0.CO;2)

Harrison, E. F., P. Minnis, B. R. Barkstrom, V. Ramanathan, R. D. Cess, and G. G. Gibson, 1990: Seasonal variation of cloud radiative forcing derived from the Earth Radiation Budget Experiment. *J. Geophys. Res. Atmos.*, **95**(D11), 18687-18703.

Held, I. M., and B. J. Soden, 2006: Robust Responses of the Hydrological Cycle to Global Warming. *J. Climate*, **19**, 5686–5699. doi: <http://dx.doi.org/10.1175/JCLI3990.1>

Henn, B., M. P. Clark, D. Kavetski, and J. D. Lundquist, 2015: Estimating mountain basin-mean precipitation from streamflow using Bayesian inference. *Water Resour. Res.*, **51**, 8012–8033, doi:10.1002/2014WR016736.

Hidalgo, H. G., D. R. Cayan, and M. D. Dettinger, 2005: Sources of Variability of Evapotranspiration in California. *J. Hydrometeor.*, **6**, 3–19. <https://doi.org/10.1175/JHM-398.1>.

Horton, P., Schaeffli, B., Mezghani, A., Hingray, B., and Musy, A., 2006: Assessment of climate-change impacts on alpine discharge regimes with climate model uncertainty. *Hydrological Processes*, **20**(10), 2091–2109. <https://doi.org/10.1002/hyp.6197>

Ineichen, P., and R. Perez, 1999: Derivation of cloud index from geostationary satellites and application to the production of solar irradiance and daylight illuminance data. *Theor. Appl. Climatol.*, **64**, 119–130.

Jensen, M.E., and H. R. Haise, 1963: Estimating evapotranspiration from solar radiation: Proceedings of the American Society of Civil Engineers. *Journal of Irrigation and Drainage*, **89**, 15–41.

Jensen, M.E., D. C. N. Rob, and C. E. Franzoy, 1969: Scheduling irrigations using climate-crop-soil data. *Proceedings: New Orleans, La., National Conference on Water Resources Engineering of the American Society of Civil Engineers*, 20.

Jeton, A. E., M. D. Dettinger, and J. L. Smith, 1996: Potential effects of climate change on streamflow, eastern and western slopes of the Sierra Nevada, California and Nevada. *Water Resources Investigations Rep. 95-4260.*, U. S. Geological Survey.

Karl, T. R., and W. E. Riebsame, 1989: The impact of decadal fluctuations in mean precipitation and temperature on runoff: A sensitivity study over the United States. *Clim. Change*, **15**, 423–447.

Knowles, N., M. D. Dettinger, and D. R. Cayan, 2006: Trends in snowfall versus rainfall for the western United States. *J. Clim.*, **19**(18), 4545–4559.

Kottek, M., J. Grieser, C. Beck, B. Rudolf, and F. Rubel, 2006: World Map of the Köppen-Geiger climate classification updated. *Meteorol. Z.*, **15**, 259–263. DOI: 10.1127/0941-2948/2006/0130.

Lapo, K. E., L. M. Hinkelman, C. C. Landry, A. K. Massmann, and J. D. Lundquist, 2015: A simple algorithm for identifying periods of snow accumulation on a radiometer. *Water Resour. Res.*, **51**, 7820–7828, doi:10.1002/2015WR017590.

Lapo, K. E., L. M. Hinkelman, E. Sumargo, M. Hughes, and J. D. Lundquist, 2017: A critical evaluation of modeled solar irradiance over California for hydrologic and land surface modeling. *J. Geophys. Res. Atmos.*, **122**, 299–317, doi:10.1002/2016JD025527.

Le Moine, N., F. Hendrickx, J. Gailhard, R. Garçon, and F. Gottardi, 2015: Hydrologically Aided Interpolation of Daily Precipitation and Temperature Fields in a Mesoscale Alpine Catchment. *J. Hydrometeorology*, **16**, 2595–2618, <https://doi.org/10.1175/JHM-D-14-0162.1>.

Leavesley, G. H., R. W. Lichty, B. M. Troutman, and L. G. Saindon, 1983: Precipitation-runoff modeling system: User's manual. *Water-Resources Investigation Report*, 83-4238 pp., U.S. Geol. Surv.

Lehning, M., H. Löwe, M. Ryser, and N. Raderschall, 2008: Inhomogeneous precipitation distribution and snow transport in steep terrain. *Water Resour. Res.*, **44**, W07404, doi:10.1029/2007WR006545.

Lettenmaier, D. P., 2017: Observational breakthroughs lead the way to improved hydrological predictions. *Water Resour. Res.*, **53**, 2591–2597, doi:10.1002/2017WR020896.

- Luce, C. H., V. Lopez-Burgos, and Z. Holden, 2014: Sensitivity of snowpack storage to precipitation and temperature using spatial and temporal analog models. *Water Resour. Res.*, **50**, 9447–9462, doi:10.1002/2013WR014844.
- Lundquist, J. D., et al., 2016: Yosemite Hydroclimate Network: Distributed stream and atmospheric data for the Tuolumne River watershed and surroundings. *Water Resour. Res.*, **52**, 7478–7489, doi:10.1002/2016WR019261.
- Lundquist, J. D., J. R. Minder, P. J. Neiman, and E. Sukovich, 2010: Relationships between Barrier Jet Heights, Orographic Precipitation Gradients, and Streamflow in the Northern Sierra Nevada. *J. Hydrometeor.*, **11**, 1141–1156, <https://doi.org/10.1175/2010JHM1264.1>.
- Lundquist, J. D., M. D. Dettinger, and D. R. Cayan, 2005: Snow-fed streamflow timing at different basin scales: Case study of the Tuolumne River above Hetch Hetchy, Yosemite, California. *Water Resour. Res.*, **41**, W07005, doi:10.1029/2004WR003933.
- Lundquist, J. D., M. D. Dettinger, I. T. Stewart, and D. R. Cayan, 2009: Variability and trends in spring runoff in the western United States. *Climate warming in western North America: evidence and environmental effects*. University of Utah Press, Salt Lake City, Utah, USA, 63–76.
- Mao, Y., B. Nijssen, and D. P. Lettenmaier, 2015: Is climate change implicated in the 2013–2014 California drought? A hydrologic perspective. *Geophys. Res. Lett.*, **42**, 2805–2813. doi: 10.1002/2015GL063456.
- Marks, D., and J. Dozier, 1992: Climate and energy exchange at the snow surface in the alpine region of the Sierra Nevada: 2. Snow cover energy balance. *Water Resour. Res.*, **28**(11), 3043–3054.
- Markstrom, S. L., R. S. Regan, L. E. Hay, R. J. Viger, R. M. T. Webb, R. A. Payn, and J. H. LaFontaine, 2015: PRMS-IV, the precipitation-runoff modeling system, version 4. *U.S. Geological Survey Techniques and Methods*, book 6, chap. B7, 158 p., <http://dx.doi.org/10.3133/tm6B7>.
- McCabe, G. J., and D. M. Wolock, 2011: Independent effects of temperature and precipitation on modeled runoff in the conterminous United States. *Water Resour. Res.*, **47**, W11522, doi:10.1029/2011WR010630.
- Morán-Tejeda, E., J. Lorenzo-Lacruz, J. I. López-Moreno, K. Rahman, and M. Beniston, 2014: Streamflow timing in mountain rivers in Spain: Recent changes and future projections. *J. Hydrology*, **517**, 1114–1127. doi: 10.1016/j.jhydrol.2014.06.053.
- Mote, P. W., 2006: Climate-driven variability and trends in mountain snowpack in western North America. *J. Climate*, **19**, 6209–6220.
- Mote, P. W., S. Li, D. P. Lettenmaier, M. Xiao, M., and R. Engel, 2018: Dramatic declines in snowpack in the western US. *npj Climate and Atmospheric Science*, **1**(1), 2.
- Musselman, K. N., M. P. Clark, C. Liu, K. Ikeda, and R. Rasmussen, 2017: Slower snowmelt in a warmer world. *Nat. Clim. Change*, **7**(3), 214–219.

Nowak, K., M. Hoerling, B. Rajagopalan, and E. Zagona, 2012: Colorado River basin hydroclimatic variability. *J. Climate*, **25**, 4389–4403.

O’Gorman, P. A., and T. Schneider, 2008: The Hydrological Cycle over a Wide Range of Climates Simulated with an Idealized GCM. *J. Climate*, **21**, 3815–3832. doi: <http://dx.doi.org/10.1175/2007JCLI2065.1>

Painter, T. H., S. McKenzie Skiles, J. S. Deems, W. Tyler Brandt and J. Dozier, 2017: Variation in rising limb of Colorado River snowmelt runoff hydrograph controlled by dust radiative forcing in snow. *Geophys. Res. Lett.*, **44**. <https://doi.org/10.1002/2017GL075826>

Pellicciotti, F., T. Raschle, T. Huerlimann, M. Carenzo, and P. Burlando, 2011: Transmission of solar radiation through clouds on melting glaciers: A comparison of parameterizations and their impact on melt modeling. *J. Glaciol.*, **57**(202), 367–381, doi:10.3189/002214311796406013.

Perez, R., P. Ineichen, K. Moore, M. Kmiecik, C. Chain, R. George, and F. Vignola, 2002: A new operational model for satellite-derived irradiances: description and validation. *Solar Energy*, **73**, 307-317.

Raleigh, M. S., B. Livneh, K. Lapo, and J. D. Lundquist, 2016: How Does Availability of Meteorological Forcing Data Impact Physically Based Snowpack Simulations?. *J. Hydrometeorology*, **17**, 99–120, <https://doi.org/10.1175/JHM-D-14-0235.1>.

Ralph, F. M., C. Hecht, and B. Kawzenuk (2017, April 6). *How Many Atmospheric Rivers Have Hit the U.S. West Coast During the Remarkably Wet Water Year 2017?*. Retrieved from <http://cw3e.ucsd.edu/how-many-atmospheric-rivers-have-hit-the-u-s-west-coast-during-the-remarkably-wet-water-year-2017/>

Rice, R., R. C. Bales, T. H. Painter, and J. Dozier, 2011: Snow water equivalent along elevation gradients in the Merced and Tuolumne River basins of the Sierra Nevada. *Water Resour. Res.*, **47**, W08515, doi:10.1029/2010WR009278.

Rosenthal, W., and J. Dozier, 1996: Automated mapping of montane snow cover at subpixel resolution from the Landsat Thematic Mapper. *Water Resour. Res.*, **32**, 115–130, <https://doi.org/10.1029/95WR02718>.

Schirmer, M., V. Wirz, A. Clifton, and M. Lehning, 2011: Persistence in intra-annual snow depth distribution: 1. Measurements and topographic control. *Water Resour. Res.*, **47**, W09516. <https://doi.org/10.1029/2010WR009426>

Schöner, W., I. Auer, and R. Böhm, 2009: Long term trend of snow depth at Sonnblick (Austrian Alps) and its relation to climate change. *Hyrdol. Process*, **23**, 1052–1063.

Seager, R., M. Hoerling, S. Schubert, H. Wang, B. Lyon, A. Kumar, J. Nakamura, and N. Henderson, 2015: Causes of the 2011–14 California Drought. *J. Climate*, **28**, 6997–7024, <https://doi.org/10.1175/JCLI-D-14-00860.1>

Shi, X. and D. Durran, 2016: Sensitivities of Extreme Precipitation to Global Warming Are Lower over Mountains than over Oceans and Plains. *J. Climate*, **29**, 4779–4791,

<https://doi.org/10.1175/JCLI-D-15-0576.1>

Simpson, J. J., M. D. Dettinger, F. Gehrke, T. J. McIntire, and G. L. Hufford, 2004: Hydrologic scales, cloud variability, remote sensing, and models: Implications for forecasting snowmelt and streamflow. *Weather and forecasting*, **19**(2), 251-276.

Slack, J. R., and J. M. Landwehr, 1992: Hydro-climatic data network (HCDN): A U.S. Geological Survey streamflow data set of the United States for the study of climate variations, 1874–1988, *Open-File Rep. 92- 129*, U. S. Geological Survey.

Sproles, E. A., T. R. Roth, and A. W. Nolin, 2017: Future snow? A spatial-probabilistic assessment of the extraordinarily low snowpacks of 2014 and 2015 in the Oregon Cascades. *The Cryosphere*, **11**, 331-341. doi:10.5194/tc-11-331-2017.

Stewart, I. T., D. R. Cayan, and M. D. Dettinger, 2005: Changes towards earlier streamflow timing across western North America. *J. Climate*, **18**, 1136-1155.

Stoelinga, M. T., M. D. Albright, and C. F. Mass, 2009: A new look at snowpack trends in the Cascade Mountains. *J. Climate*, **23**(10), 2473–2491, doi:10.1175/JCLI3321.1.

Sumargo, E., and D. R. Cayan, 2017: Variability of cloudiness over mountain terrain in the Western United States. *J. Hydrometeorol.*, **18**, 1227–1245, <https://doi.org/10.1175/JHM-D-16-0194.1>.

Sumargo, E., and D. R. Cayan, 2018: The influence of cloudiness on hydrologic fluctuations in the mountains of the western United States. *Water Resour. Res.* (submitted).

Trujillo, E., J. A. Ramírez, and K. J. Elder, 2007: Topographic, meteorologic, and canopy controls on the scaling characteristics of the spatial distribution of snow depth fields. *Water Resour. Res.*, **43**, W07409. <https://doi.org/10.1029/2006WR005317>

U.S. Army Corps of Engineers, 1956: *Snow hydrology: Summary report of the snow investigations*. North Pacific Division, U.S. Army Corps of Engineers, 437 pp.

Verdy, A., M. R. Mazloff, B. D. Cornuelle, and S. Y. Kim, 2014: Wind-driven sea level variability on the California coast: an adjoint sensitivity analysis. *Journal of Physical Oceanography*, **44**(1), 297-318.

Viviroli, D., D. R. Archer, W. Buytaert, H. J. Fowler, G. B. Greenwood, A. F. Hamlet, Y. Huang, G. Koboltschnig, M. I. Litaor, J. I. López-Moreno, S. Lorentz, B. Schädler, H. Schreier, K. Schwaiger, M. Vuille, and R. Woods, 2011: Climate change and mountain water resources: overview and recommendations for research, management and policy. *Hydrol. Earth Syst. Sci.*, **15**, 471-504, <https://doi.org/10.5194/hess-15-471-2011>.

Williams, A. P., R. Seager, J. T. Abatzoglou, B. I. Cook, J. E. Smerdon, and E. R. Cook, 2015: Contribution of anthropogenic warming to California drought during 2012–2014. *Geophys. Res. Lett.*, **42**, 6819–6828, doi:10.1002/2015GL064924.

Woodhouse, C. A., G. T. Pederson, K. Morino, S. A. McAfee, and G. J. McCabe, 2016: Increasing influence of air temperature on upper Colorado River streamflow. *Geophys. Res.*

Lett., **43**, 2174–2181, doi:10.1002/2015GL067613.

Yin, J. H., 2005: A consistent poleward shift of the storm tracks in simulations of 21st century climate. *Geophys. Res. Lett.*, **32**, L18701, doi:10.1029/2005GL023684.

Zelinka, M. D., D. A. Randall, M. J. Webb, and S. A. Klein, 2017: Clearing clouds of uncertainty. *Nat. Climate Change*, **7**, 674-678. doi:10.1038/nclimate3402.

Chapter 5

Conclusions

This dissertation highlights the importance of mountain cloud variability as a driver of surface hydrologic variations in the mountains of the western U.S. The results from this study include the novel characterizations of spatial and temporal mountain cloud variability (Chapter 2), of snowmelt and streamflow responses to daily cloudiness variability (Chapter 3), and of watershed-scale snow-fed runoff response to upstream cloudiness variability (Chapter 4). Chapter 1 of this dissertation introduces the scientific problems and outlines the research questions specifically addressed in the three subsequent chapters. Correspondingly, this concluding chapter summarizes the main findings.

Chapter 2 first explores the means and variability of cloudiness, as measured by GOES cloud albedo (α_{cloud}) over mountain terrain across the western U.S. As expected, the results show greater cloudiness in the northwestern U.S. than in the southwestern U.S. across all seasons. On the other hand, the variability is roughly comparable in both northwestern and southwestern U.S., but emphasized during the springtime in the maritime mountains, such as the Sierra Nevada and the Cascades. When scaled by its mean, the (relative) variability is greatest during the spring-summer period, particularly in the west slope of the Sierra Nevada.

On a daily scale, the α_{cloud} variability often exceeds 50% of a given location's long-term average. In terms of incoming solar radiation (SWF), this amount is equivalent to 90-140 W m⁻². On a seasonal scale, the α_{cloud} variability often exceeds 10% of a given location's long-term average, equivalent to 10-20 W m⁻² of SWF. For reference, Mizukami et al. (2014) found from their study in upper Colorado River basin that an 85 W m⁻² SWF difference in

May results in ~20% difference in annual runoff and ~3-week difference in snowmelt/runoff timing.

A rotated empirical orthogonal function (REOF) analysis of daily α_{cloud} anomalies reveals that a few leading modes account for the predominant portion of the daily variability of clouds over the western United States, with the first five REOFs accounting for 67% of the variance. Importantly, the modes occupy relatively large regional scales. The first mode resides over the northern Sierra Nevada and the southern Cascades and the second mode resides over the northern Rockies in Idaho and western Montana. Monthly standard deviations of the associated temporal coefficients (principal components) indicate that both modes have greatest amplitude in winter and spring, when snow deposition and snowmelt are most active. Thus, these fluctuating patterns are pertinent to mountain snowmelt-runoff processes—a major source of water supply in the western U.S. Although the two leading modes are well-correlated with the upper level (geopotential) height, they are surprisingly only weakly associated with well-known teleconnection patterns, with only Arctic Oscillation exerting a significant influence during the snow seasons (winter-spring).

Chapter 3 investigates the snowmelt and streamflow responses to cloud cover variability [as measured by a cloud cover index (CC), which increases linearly with α_{cloud}]. A contingency analysis demonstrates that snowmelt usually coincides with lesser CC, and snow accumulation or no snow loss occurs with higher CC. This and other analyses demonstrate the importance of CC to snowpack dynamics. A lag-correlation analysis subsequently confirms this dominant inverse relationship in the sense that as CC decreases, short wave flux (SWF) increases, and snowmelt and snow-fed streamflow increases. Snowmelt and streamflow responses to CC variations typically peak 1-3 days after anomalously high or low

cloudiness. The inverse relationship lasts longer into the early summer, albeit weaker, in wetter years. Revisiting the REOF analysis performed in the previous chapter, correlations between the leading RPC modes and snowmelt/streamflow demonstrate statistically significant snowmelt and streamflow responses to regional cloudiness patterns.

Results from a linear regression analysis relating snowmelt and streamflow to CC variations from 5 days previous to zero days quantifies the multi-day cumulative effect of cloudiness. Over different locations and different months, this linear analysis indicates that CC accounts for 5%-56% of day-to-day snowmelt variability and 2%-47% of streamflow variability. The magnitude of the cloudiness effect typically peaks in May. The limited amount of variance captured is likely because the snowmelt and streamflow responses to CC variations may be, to some extent, non-linear.

The snowmelt and streamflow responses to CC tend to be stronger at lower elevations during the early and late snowmelt seasons, and at higher elevations during the peak snowmelt season. The relatively strong lower elevations' responses in the early snowmelt season reflect the fact that snowpack melts at lower elevations first, owing to the thinner snowpack, warmer air and snowpack temperatures, and lower snowpack cold content, which is the energy required to bring the snowpack temperature to melting point (Marks et al., 1999). With such conditions, lower elevations' snowpack is ready to melt with a relatively small increase in solar radiation input.

The relatively strong higher elevations' responses in the peak snowmelt season, on the one hand, reflect snowmelt initiations at higher elevations, as enough energy has finally been built up to melt this thicker and formerly colder snowpack. On the other hand, it may also indicate the complication from higher air temperature and downward longwave radiation

associated with the forest cover, which is typically denser at lower elevations. Overall, this analysis suggests the importance of accounting for non-linearity associated with cold content and external factors (e.g., longwave radiation from the atmosphere, forest cover, slope and aspect).

Chapter 4 applies the datasets and findings derived in the two preceding chapters to watershed modeling. In so doing, experiments are conducted using optimized versions of the California Department of Water Resources' PRMS hydrologic model. For comparative purposes, we include separate models of two close-by watersheds, i.e., the upper Tuolumne River and the Merced River, which drain the west slope of the central Sierra Nevada mountain range. The CC datasets are used to derive SWF, which is subsequently used as an input to the PRMS model. As discussed in Section 4.2.1 and Appendix 4C, this new SWF parameterization provides significant improvements on SWF estimates. When used as a forcing in the PRMS model, with calibrations, this method offers significant improvements on basin runoff simulations.

This method also provides a means of conducting a set of experiments, where the response of snow-fed runoff to the observed cloudiness is compared to that from altered cloudiness and SWF. Of particular interest are the effects of daily CC variability, the relative importance of high, mid and low elevation cloudiness variations, and the effects of cloudiness variation that have stronger intensity than historically observed.

In both upper Tuolumne and upper Merced watersheds, we find cloudiness variability affects the snow-fed runoff by distributing it throughout the snowmelt season. This effect acts to increase runoff in the early season and decrease runoff in the later snowmelt season, resulting in runoff from the natural system that has (1-3 days) earlier spring onset than it

would have had cloudiness been smoothed out so it only had a climatological average seasonal cycle. This characteristic is mostly evident in wet years, but not in dry years when the snowmelt and runoff occurs earlier in a more concentrated pulse.

When cloudiness variations at different elevation bands are accounted for, cloudiness at higher elevation bands of both upper Tuolumne and upper Merced watersheds have greater effects on the basin runoff. This result is presumably related to the fact that other external factors (e.g., cooler air temperature and less forest cover) are typically not as dominant and that snowpack that feeds the stream flows is typically thicker at higher elevations. On the other hand, cloudiness at lower elevation bands has greater effects on the basin evapotranspiration owing to the warmer temperatures at lower elevations. Furthermore, cloudiness delays the spring onset by 2-15 days, regardless of the elevation bands.

The results from amplifying clear/cloudy interludes show overall greater snow-fed streamflow sensitivity to “relatively cloudy periods get cloudier” experiments, which delay the spring onsets by 3-5 days in most HRUs. In contrast, the “relatively clear periods gets clearer” experiments barely affect the streamflow. In comparison, widespread warming in the western North America during the second half of the 20th century resulted in 1-4 weeks earlier spring onsets (Stewart et al., 2005), underlining the pertinence of cloudiness in moderating the effect of climate change-induced springtime warming. This result may also provide an outlook on the effects of future changes in cloudiness pattern under the intensification of dry/wet hydrologic extremes associated with climate change (Swain et al., 2018).

In summary, this dissertation as introduced in Chapter 1 addresses the following goals:

1. To characterize spatial and temporal cloudiness variabilities over the mountain terrain of the western U.S., from which new questions arise:
 - a. How do these variabilities relate to intra-seasonal modes of weather variability, like the Madden-Julian Oscillation?
 - b. How do they evolve with climate change?
 - c. How do they compare to those in other mountain regions, such as the Rockies, Alps and Himalayas?
2. To evaluate how this variability influences daily-seasonal snowmelt and runoff processes, from which new questions arise:
 - a. How would the results change if non-linearity is accounted for, such as that associated with snowpack cold content, longwave and turbulent fluxes?
 - b. How do they evolve with climate change?
3. To examine the applicability of satellite-derived SWF estimate in hydrologic modeling, which will allow spatially and temporally comprehensive investigation of the effects of cloudiness variability and the associated SWF variations on snowmelt-runoff processes at watershed scales. At present, more analyses need to be done to better constrain the effects of:
 - a. Intensification of cloud cover fluctuations, which we have shown to be sensitive to threshold between clear sky and cloudy sky, and
 - b. Complications from the advective temperature component, as opposed to the radiative temperature component associated with cloudiness.

References

Mizukami, N., M. P. Clark, A. G. Slater, L. D. Brekke, M. M. Elsner, J. R. Arnold, and S.

Gangopadhyay, 2014: Hydrologic Implications of Different Large-Scale Meteorological Model Forcing Datasets in Mountainous Regions. *J. Hydrometeorol.*, **15**(1), 474–488. doi:10.1175/JHM-D-13-036.1.

Marks, D., J. Domingo, D. Susong, D., T. Link, and D. Garen, 1999: A spatially distributed energy balance snowmelt model for application in mountain basins. *Hydrol. Process.*, **13**, 1935-1959. doi:10.1002/(SICI)1099-1085(199909)13:12/13<1935::AID-HYP868>3.0.CO;2-C

Stewart, I. T., D. R. Cayan, and M. D. Dettinger, 2005: Changes towards earlier streamflow timing across western North America. *J. Climate*, **18**, 1136-1155.

Swain, D. L., B. Langenbrunner, J. D. Neelin, and A. Hall, 2018: Increasing precipitation volatility in twenty-first-century California. *Nature Climate Change*, **1**.